SERI/STR-211-3231
DE88001108

October 1987

Research on High-Efficiency, Stacked, Multijunction, Amorphous Silicon Alloy Thin-Film Solar Cells

Final Subcontract Report 11 October 1983– 30 October 1986

J. Bragagnolo
Spire Corporation
Bedford, Massachusetts

Prepared under Subcontract No. ZB-4-03055-1

SERI

Solar Energy Research Institute
A Division of Midwest Research Institute

1617 Cole Boulevard
Golden, Colorado 80401-3393

Operated for the
U.S. Department of Energy
under Contract No. DE-AC02-83CH10093

SERI/STR-211-3231
UC Category: 63
DE88001108

SERI/STR--211-3231

DE88 001108

Research on High-Efficiency, Stacked, Multijunction, Amorphous Silicon Alloy Thin-Film Solar Cells

Final Subcontract Report
11 October 1983–30 October 1986

J. Bragagnolo
Spire Corporation
Bedford, Massachusetts

October 1987

SERI Technical Monitor: W. Luft

Prepared under Subcontract No. ZB-4-03055-1

Solar Energy Research Institute
A Division of Midwest Research Institute

1617 Cole Boulevard
Golden, Colorado 80401-3393

Prepared for the
U.S. Department of Energy
Contract No. DE-AC02-83CH10093

NOTICE

Printed in the United States of America
Available from:
National Technical Information Service
U.S. Department of Commerce
5285 Port Royal Road
Springfield, VA 22161

Price: Microfiche A01
Printed Copy A06

Codes are used for pricing all publications. The code is determined by the number of pages in the publication. Information pertaining to the pricing codes can be found in the current issue of the following publications, which are generally available in most libraries: *Energy Research Abstracts, (ERA); Government Reports Announcements* and Index (*GRA* and I); *Scientific and Technical Abstract Reports (STAR);* and publication, NTIS-PR-360 available from NTIS at the above address.

ACKNOWLEDGEMENTS

The following personnel participated in the research reported in this report:

Spire Corporation:	Julio Bragagnolo,	Principal Investigator and Program Manager
	J. Booker	
	V. Dalal	
	A. Greenwald	
	M. Leonard	
	P. Littlefield	
	A. Mastrovito	
	L. Mitzman	
	S. Tobin	
	G. Storti	
Polaroid:	F. Berry	
	J. Cary	
	C. Fuleihan	
	M. Green	
	D. Slobodin	
University of Delaware:	Bill Baron	
	Stephen Hegedus	
Drexel University:	Allen Rothwarf (Consultant)	

U.S. Department of Energy, SERI Contract #AB-4-03055-1
Polaroid Corporation
Southern California Edison

TABLE OF CONTENTS

TABLE OF CONTENTS (Concluded)

LIST OF ILLUSTRATIONS

LIST OF ILLUSTRATIONS (Continued)

LIST OF ILLUSTRATIONS (Concluded)

LIST OF TABLES

LIST OF TABLES (Continued)

LIST OF TABLES (Concluded)

PREFACE

This report covers the third year of a three year project to develop high efficiency, stable multi-junction amorphous silicon alloy solar cells. In the report for the first year (SERI/STR-211-2730), we described: (1) the design and construction of a radio frequency (RF) plasma enhanced chemical vapor deposition (CVD) systems used to obtain the amorphous silicon alloys, (2) the deposition and characterization of the initial a-Si:H and a-(Si,Ge):H layers using dark and photoconductivity measurements and, (3) the fabrication and characterization of a 7.8% efficient a-Si:H p-i-n cell and of a tunnel-junction a-Si:H/a-Si:H tandem cell. A Semiannual Report (SERI/STR-211-2636) was also published during the first phase of this program.

In the report for the second year, (SERI/STR-211-2946), we described: (1) the properties of a-Si:H and a-(Si,Ge):H layers grown in our multi-sector reactor, with a high light-to-dark photoconductivity ratio ($>10^6$) observed for a-Si:H films and decreasing with increasing Ge content, (2) the improvement in the Urbach edge energy caused by H_2 dilution and the decrease in SiH_2 bonding resulting from increasing negative substrate bias during a-(Si,Ge):H growth in a triode geometry, (3) the design and construction of a CVD reactor for deposition of highly transparent, textured SnO_2 layers, (4) the development of 8.6% efficient a-Si:H cells, 6.8% efficient a-(Si,Ge):H cells, 7.5% efficient a-Si/a-Si tandem cells and 6.7% a-Si/a-(Si,Ge) tandem cells, all with an area of 0.1 cm^2 and (5) a new tandem cell analysis technique based on quantum efficiency measurements. A Semiannual Report (SERI/STR-211-2845) was also published covering the first half of the second phase of this program.

In this third year, we report an extensive effort to solve the key outstanding problems impeding the fabrication of high efficiency tandem cells. The emphasis is on the last six months of this effort, since in addition to the reports previously reviewed, the last Semiannual Report (SERI/STR-211-3104) covers the first half of the last phase of this program in detail. However, the main achievements of the preceding periods are reviewed as appropriate.

This report is organized into six sections including a Summary, a section devoted to equipment description and four sections devoted to each of the program tasks: Semiconductor Materials Studies, Non-Semiconductor Materials Studies, Single-Junction Cell Research, and Multi-Junction Cell Research. It includes three appendices dealing with safety issues, calibration procedures, and tandem cell analysis.

We describe (1) new deposition techniques to obtain pinhole-free a-Si:H alloy films by avoiding dust formation in the plasma (2) the deposition of low absorptance, textured SnO_2 layers by thermal CVD of $Sn(CH_3)_4$, (3) a more stable, high reflectance Ti/Ag back contact, (4) the application of the new deposition techniques to the achievement of 10.5%, 0.1 cm^2, 10.1%, 0.5 cm^2 and 9.4%, 1 cm^2 a-Si:H p-i-n devices, (5) the development of a-(Si,Ge):H cells with efficiency ranging from 5.4% for a-(Si,Ge):H cells with a bandgap of 1.45 eV to 7.5% for graded bandgap cells with an average bandgap of 1.67 eV and (6) the development of a-Si/a-(Si,Ge) tandem cells with 6.5% and 7.2% efficiency using a 1.45 eV and a graded bottom cell i-layer with 1.67 eV average bandgap, respectively.

This work was a collaborative effort between Spire and Polaroid Corporations. In addition to SERI, Polaroid and Southern California Edison supported this effort. V. Dalal was Principal Investigator and Program manager during the first two years of this contact. J. Bragagnolo was Program Manager during the last year and Principal Investigator during the last half year.

SECTION 1

SUMMARY

The emphasis in this report is on activities that have been taking place during the last half-year of this program. A program summary, including key earlier achievements, is presented in what follows.

1.1 OBJECTIVE

The objectives of this program were: i) to research a-Si alloy materials, ii) to use those materials in the preparation of thin-film stacked multi-junction solar cells, iii) to utilize a multi-chamber deposition system for the fabrication of such devices and iv) to demonstrate in FY 1986 a stable 13% (AM1) solar conversion efficiency for a 1 cm^2 multi-junction cell.

1.2 APPROACH

The multi-junction solar cell chosen for the demonstration of high efficiency was a monolithic, two-terminal tandem device. Achievement of high efficiencies requires optimum performance of the single-junction cells composing the tandem, particularly a high efficiency a-Si:H top cell and a-(Si,Ge):H bottom cell with a bandgap (E_g) of < 1.5 eV. The program was divided into four tasks addressing the major elements of high efficiency tandem solar cells. In what follows, we describe the key results obtained in each of the four tasks.

1.3 SEMICONDUCTOR MATERIALS STUDIES

A single chamber and a six-sector deposition system for the growth of a-Si alloy layers and single-junction and multi-junction devices were designed, built, and made operational during the first year.[1] A schematic view of the six-sector a-Si:H alloy deposition chamber is shown in Figure 1-1. Each sector is provided with radio frequency (rf) driven plasma electrodes in a triode configuration, gas inlets and vacuum outlets. The plasma discharge is confined within each sector, so that no deposition occurs on the walls of other sectors, but no vacuum isolation exists between them. High-quality a-Si:H films with E_g = 1.75 - 1.80 eV, dark conductivity $\sigma_D < 10^{-11}$ $(\Omega\text{-cm})^{-1}$, light-to-dark conductivity ratio $\geq 5.7 \times 10^6$ and electron and hole $(\mu\tau) \approx 2\text{-}4 \times 10^{-7}$ and $6\text{-}7 \times 10^{-8}$ cm^2/V, respectively, have been grown in this chamber.[1]

Photo and dark conductivities and hole diffusion length of a-(Si,Ge):H alloy films were found to degrade with increasing (Ge)/(Si) ratio, particularly for alloy bandgaps below 1.5 eV,[1,2] in agreement with other workers.

During the last year of the program, new deposition techniques to obtain defect-free films by avoiding dust formation in the plasma were successfully developed. High-quality a-Si:H alloys were obtained by deposition at a relatively low plasma pressure.

1.4 NON-SEMICONDUCTOR MATERIAL STUDIES

A deposition chamber for the chemical vapor deposition of low (5-10%) absorbance, low (5-15 $\Omega/\square$) resistivity, textured and specular SnO_2:F front contact layers from a gas mixture containing $Sn(CH_3)_4$, N_2, O_2 and CF_3Br was designed, built, and put into

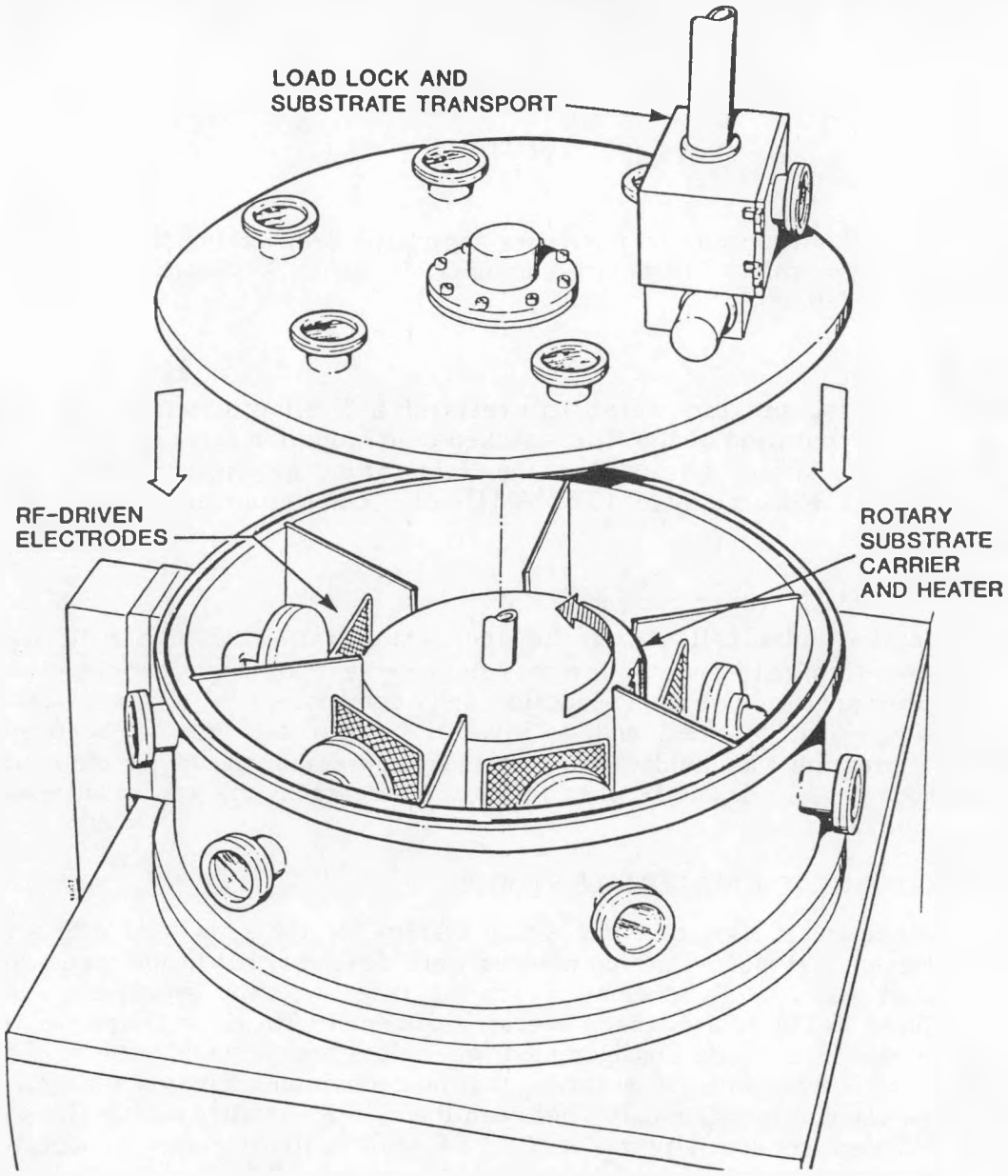

FIGURE 1-1. REACTOR VESSEL AND SUBSTRATE TRANSPORT OF PLASMA ISOLATED MULTI-SECTOR REACTOR.

operation during the final year of this program. Also, high reflectivity titanium-silver bilayer back contacts were developed for use in high efficiency devices.[3] Both developments were essential in the minimization of photon losses and opened the way for the achievement of high efficiency a-Si:H solar cells.

1.5 SINGLE-JUNCTION CELL RESEARCH

Single-junction a-Si:H cells of over 10% efficiency under AM1.5 global illumination have been made in the six-sector deposition chamber on high quality, textured SnO_2:F grown in our laboratory.[4] A summary of the highest efficiencies measured in a-Si:H cells of three area sizes can be seen in Table 1-1. The I-V characteristics of cell 20585-C9, measured by SERI and having an efficiency of 10.5% are shown in Figure 1-2.

TABLE 1-1. I-V CHARACTERISTICS OF HIGH EFFICIENCY a-Si:H CELLS AS TESTED AT SERI AND SPIRE.

Cell	Area (cm^2)	V_{oc} (mV)	J_{sc} mA/cm^2	FF (%)	Eff (%)	
20585-C9	0.0993	878	16.63	72.2	10.5	SERI
		888	17.54	70.8	11.0	Spire
20585-C1	0.503	898	16.54	68.2	10.1	SERI
		861	16.62	73.5	10.5	Spire
30582-E1	1.011	865	15.15	71.8	9.4	SERI
		848	15.73	72.1	9.6	Spire

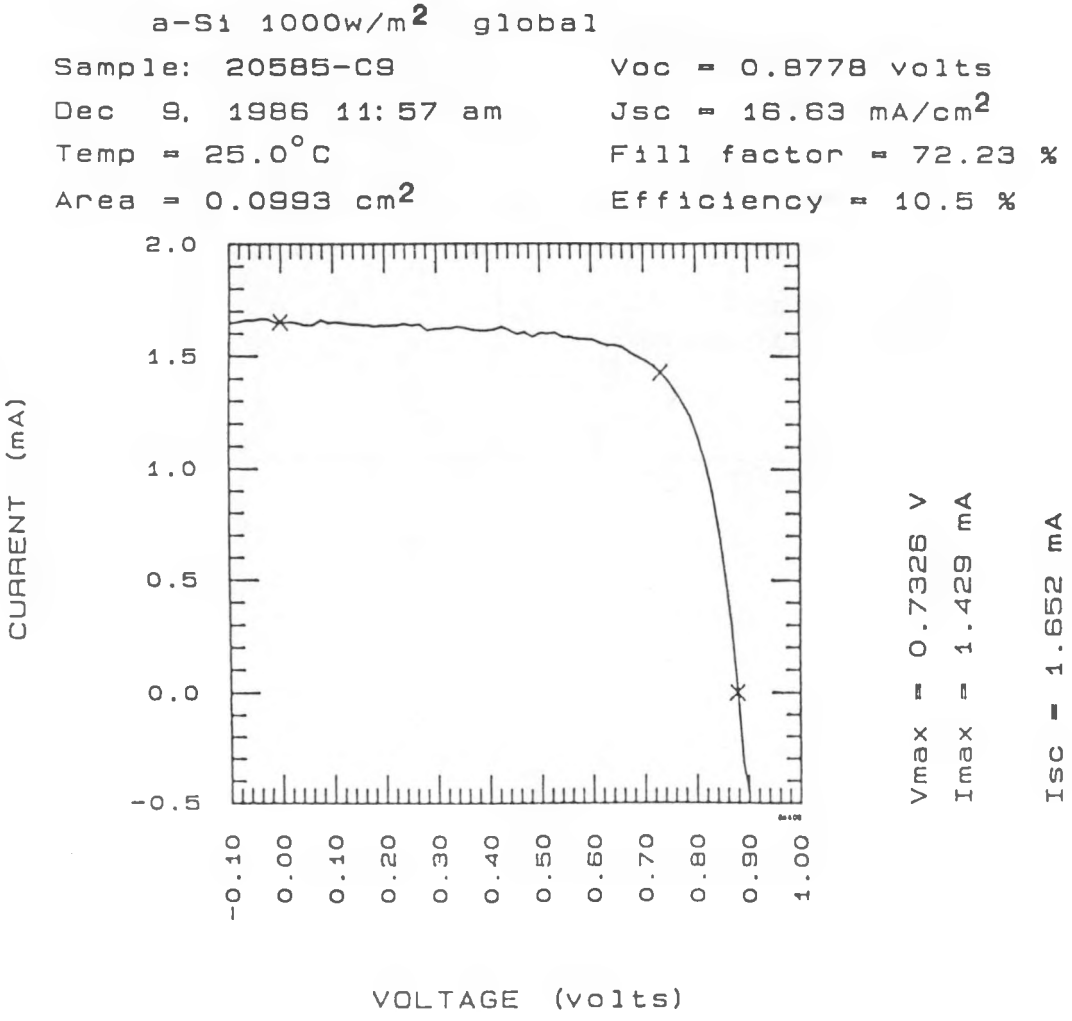

FIGURE 1-2. I-V CHARACTERISTICS OF 10.5% EFFICIENT a-Si:H CELL AS MEASURED BY SERI.

Single-junction, graded-bandgap a-(Si,Ge):H cells of 7.5% efficiency and 0.1 cm^2 area were fabricated on textured SnO_2 during the third program year[3] (Figure 1-3). Ungraded a-(Si,Ge):H cells grown on specular SnO_2 with a 1.45 eV band gap alloy i-layer developed during the last phase of this program exhibited higher light-generated currents than graded-band gap cells, namely, over 19 mA/cm^2.

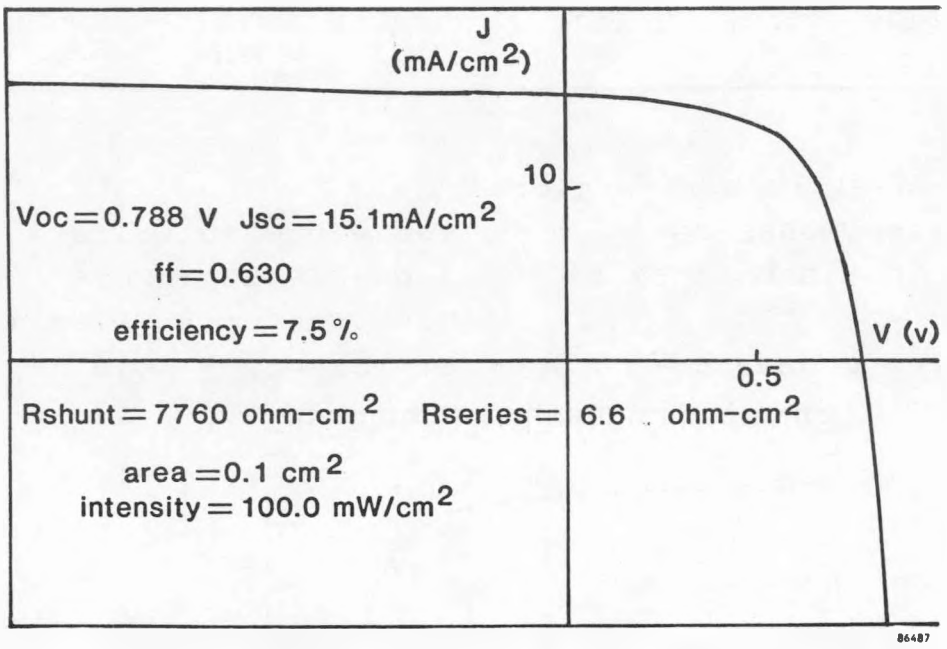

FIGURE 1-3. I-V CHARACTERISTICS OF a-(Si,Ge):H CELL.

1.6 MULTI-JUNCTION CELL RESEARCH

Multi-junction, monolithic a-Si:H/a-(Si,Ge):H cells with efficiencies of 7.2% for 0.1 cm^2 area have been fabricated.[4] A model for the prediction of the tandem efficiency achievable with given a-Si:H and a-(Si,Ge):H cells and the light-generated current to be expected from specific alloy optical properties has been perfected.[4] Also, a technique to obtain the quantum efficiency of individual cells in a tandem device has been developed.[5,6] The high quantum efficiency of a tandem cell containing the 1.45 eV alloy is compared to that of the 7.2% efficient tandem using this technique (Figure 1-4). Based on the above model, further optimization of the 1.45 eV band gap alloy could lead to tandem cells with short-circuit currents over 11 mA/cm^2 and efficiencies in excess of 11%.[4]

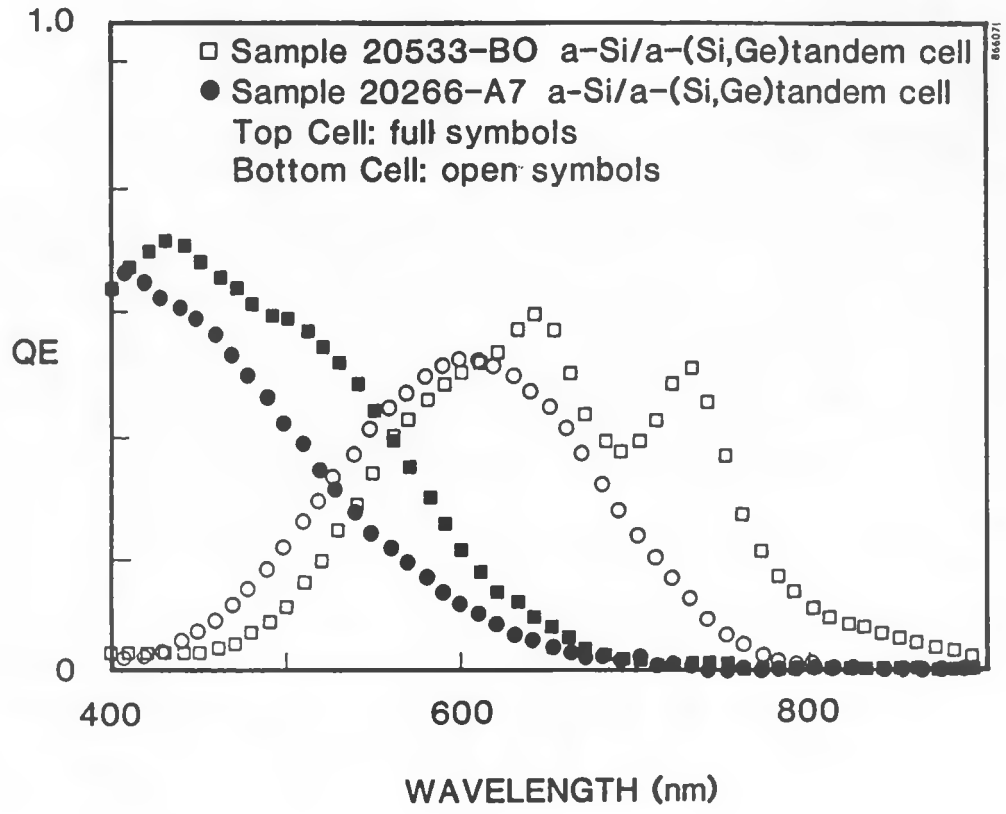

FIGURE 1-4. QUANTUM EFFICIENCY OF TANDEM CELLS

1.7 CONCLUSIONS

Deposition and analytical capabilities for the development of state-of-the-art a-Si:H alloy devices have been assembled. Single-junction a-Si:H cells of efficiency over 10% have been demonstrated, showing the quality of the a-Si:H alloy and SnO_2 deposition technology developed. A solid base for the achievement of high efficiency multi-junction cells has been laid out.

SECTION 2

DESCRIPTION OF THE DEPOSITION EQUIPMENT

Three major deposition systems were designed and built for this effort. A single chamber triode RF plasma enhanced CVD reactor was built in the first two months of the program with the goal of rapidly initiating amorphous silicon alloy material and device deposition while a more complex multi-sector reactor was being constructed. The multi-sector reactor was finished during the first program year and used to obtain the highest quality amorphous silicon alloys and devices made during this effort. In particular, data obtained during the last half year of effort, on which this report is based, refers to materials and devices fabricated in the multi-sector reactor. The single-chamber reactor continued to be used during the program for preliminary development of deposition techniques. Finally, a chamber for the deposition of SnO_2 by thermal CVD was successfully built to supply this program with highly transparent, textured SnO_2 substrates.

The major design features of the three reactors will be discussed in this section, while key materials and device results will be reviewed in Sections 3 to 6.

2.1 SINGLE-CHAMBER REACTOR

We have designed and constructed a single-chamber plasma-deposition reactor for depositing a-Si alloy films. The reactor is a bell jar type, with the substrate being held horizontally, facing downward on a heater block. The schematic diagram of the reactor is shown in Figure 2-1. The reactor can deposit films on a 4-inch x 4-inch (100 cm^2) substrate. Total internal volume is 47 liters. (Electrode size: RF: 180 cm^2, ground: 430 cm^2, rf = 13.6 MHz.) The following features are worth noting:

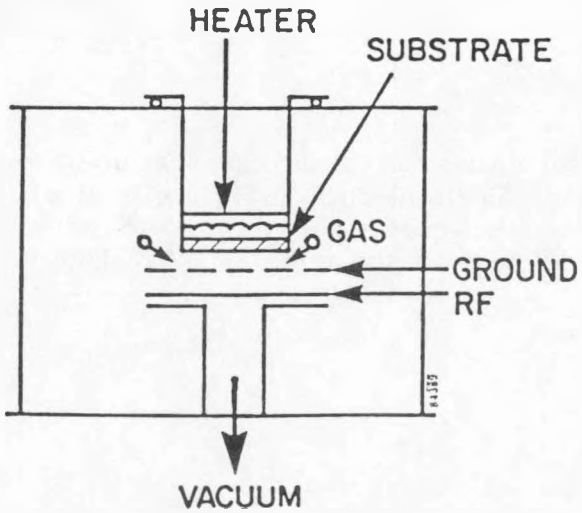

FIGURE 2-1. SCHEMATIC DIAGRAM OF SINGLE CHAMBER REACTOR.

- Oil migration into the deposition chamber is minimized by the use of a turbomolecular vacuum pump, backed by a trapped roughing pump and the use of a ballast gas (argon) to maintain foreline pressures over 100 mtorr. The turbo pump is even used during deposition with constant pressure maintained by the use of an MKS butterfly valve, pressure controller, and pressure transducer. Silicon dust is trapped before the control valve using quartz wool and stainless steel mesh filters.

- A completely separate roughing pump with foreline traps and ballast gas is used to partially evacuate the chamber from the atmosphere before the gate valve to the turbo pump is opened. The separate roughing pump also allows redundancy of pumping, an important safety consideration.

- Separate gas manifolds for doped and i-layer deposition are provided so as to minimize cross-contamination between doped and i-layers.

- Gases are controlled using Unit Instruments mass flow controllers.

- All gas lines are welded or use O-ring (Parker Ultraseal and Cajon VCR) fittings.

- Pressure-sensor activated solenoid valves are used to cut-off gas supply in the event of either power or vacuum failure.

- The reactor can be run either with a two or a three-electrode plasma geometry. A screen mesh between the live electrode and the substrate can be used to isolate the substrate from the plasma if needed. The substrate can be biased independently with positive or negative bias. Typical electrode spacing is 1 to 5 cm (variable).

This reactor was constructed during the first two months of the program.

2.2 MULTI-SECTOR REACTOR

2.2.1 Basic Design

In order to prevent cross-contamination between p, i, and n layers, and between cells of different alloys, we have designed and built a 6-sector multi-chamber reactor. The basic design of the reactor is shown in Figure 2-2. It consists of 6-sectors and a load lock.

The reactor is a rotary type with cylindrical geometry. There are two cylinders, inner and outer. The space between the outer and inner cylinders (105 liters) is evacuated and forms the plasma sectors. This space is divided into six sectors by using vertical sector dividers, which serve to confine the plasma within each sector. Each sector has its own gas inlet, and its own pumping port. There is also a central pumping port, located in the middle of the bottom base plate, which serves to pump down the entire system rapidly and is used for pumping during deposition at pressures below 100 mtorr. Each sector also has its own plasma electrodes.

The sample is introduced through a load lock which is sitting vertically above sector 1. A gate valve and a bellows-sealed push-pull feedthrough are provided. The sample is

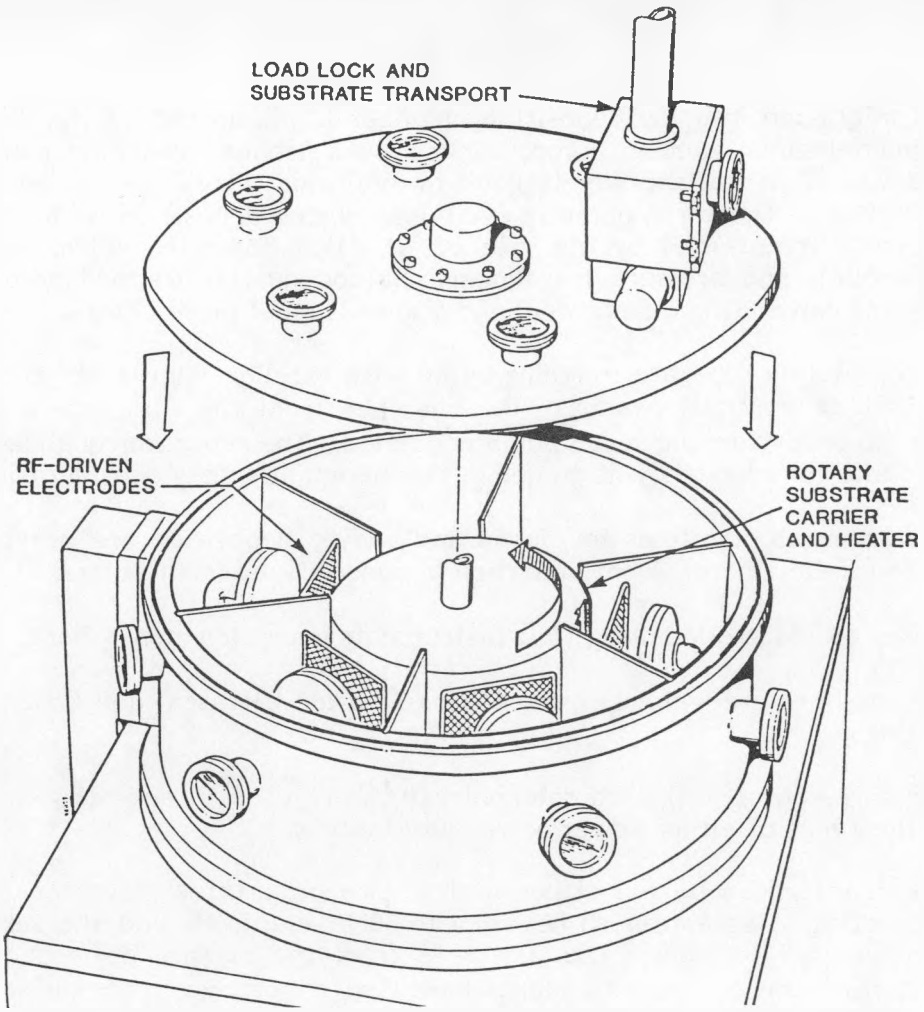

FIGUR E 2-2. REACTOR VESSEL AND SUBSTRATE TRANSPORT

transferred down into sector 1 by opening the gate valve and using the push rod. There is a spring mechanisms for locking it in position in a machined slot so that good thermal contact can be maintained with the heater block. The heaters are outside the vacuum, on the air side (inside) of the inner cylinder.

The sample is moved from sector-to-sector by rotating the inner cylinder. To withdraw the sample after the deposition is completed, the sample is brought back to sector 1, the gate valve is opened, and the push-pull rod is used to move the sample up.

It will be noticed that the sectors are plasma-isolated but not vacuum or gas isolated. This particular design is based on the experiments reported in the first Semi-annual report[7] which conclusively show that gas isolation is not necessary but plasma isolation is. Also, we have provided a cleaning electrode to strike a SiH_4 plasma in each sector before the substrate is introduced into that sector, so that any residual impurities can be gettered or buried.[7] A-Si:H is by far the best getter for O_2 etc., and by depositing ~100 nm of a-Si layer on the walls, all impurities can be buried.

Figure 2-3 shows a photograph of the front of the reactor, Figure 2-4 of the back (showing a hydraulic hoist), and Figure 2-5, of the bottom, showing the vacuum plumbing. We have provided the reactor with a number of viewports and blanked-off ports, so that instrumentation and diagnostics can be added when needed.

We shall next discuss each of the major subsystems of the reactor.

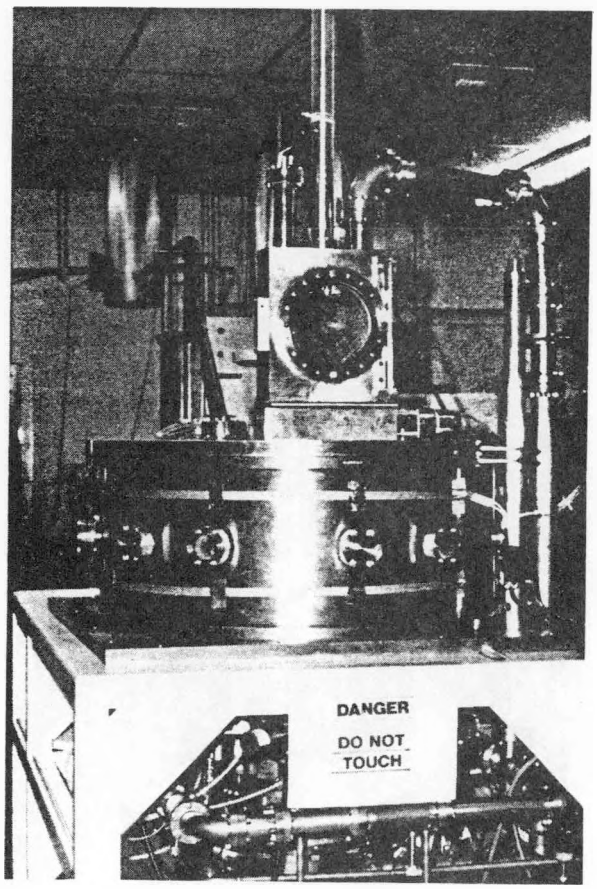

FIGURE 2-3. PHOTOGRAPH OF FRONT OF REACTOR

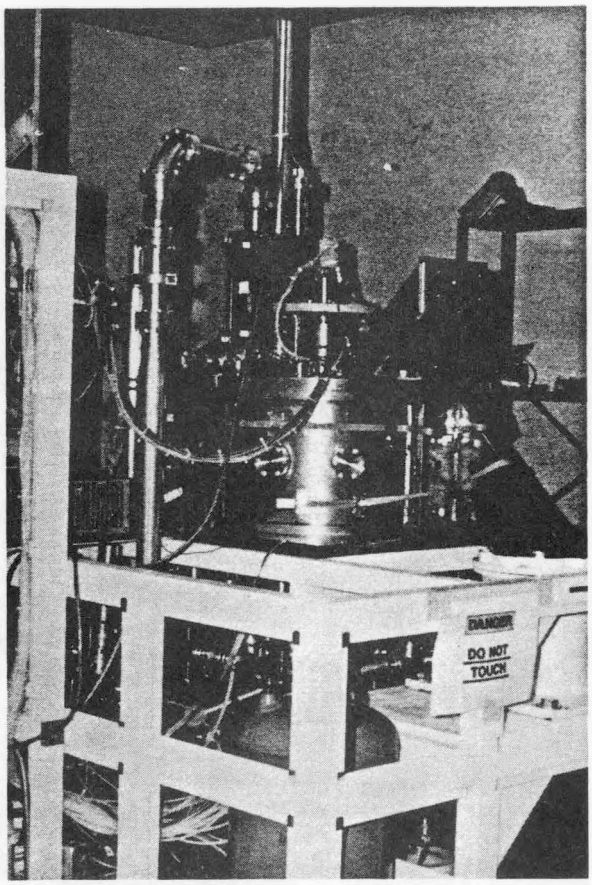

FIGURE 2-4. PHOTOGRAPH OF BACK OF REACTOR

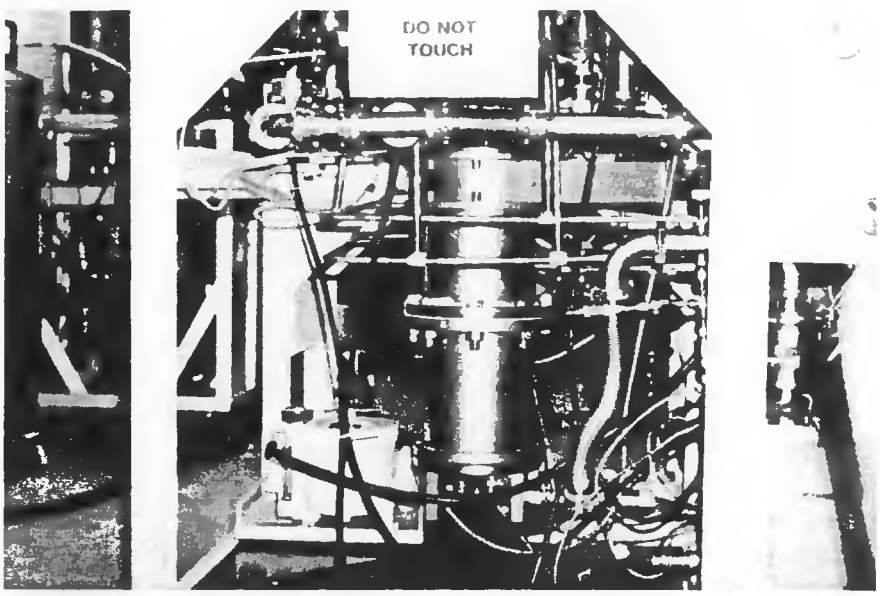

FIGURE 2-5. PHOTOGRAPH OF VACUUM SYSTEM

2.2.2 Vacuum System

To assure high purity, we have used a Leybold TMP 450 vertical turbomolecular pump, backed with a Leybold DK30 mechanical pump. There is another mechanical pump, Leybold DK30, for roughing down the system, so that the turbo-pump never sees atmospheric pressure. Argon ballast gas is bled into the foreline upstream of a trap and the DK30 pumps to prevent oil backstreaming. There is a solenoid operated gate valve (Cooke Vacuum) which allows the system to be opened to the turbo-pump.

Figure 2-6 shows a schematic diagram of the vacuum system. The diagram is self explanatory. A pressure control valve (MKS) controls the pressure during operation. The load lock can also be pumped down to low pressures using the turbo-pump.

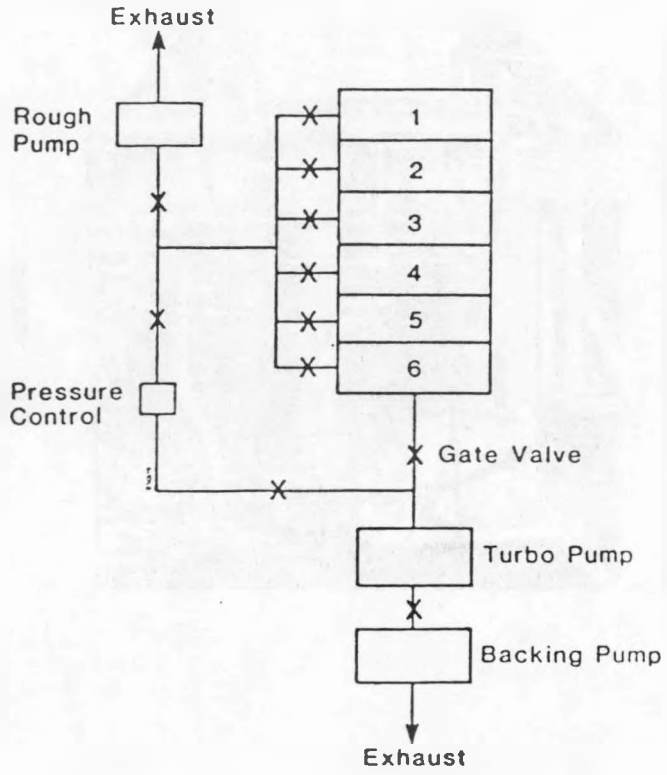

FIGURE 2-6. SCHEMATIC DIAGRAM OF VACUUM SYSTEM

All vacuum valves are pneumatically operated, normally closed valves. The air pressure is applied using electrical solenoid valves.

2.2.3 Gas System

The inlet gas system is divided into two basic manifolds, the I (intrinsic) and D (dopant) manifolds. A schematic diagram of the gas inlet system is shown in Figure 2-7. Note that each sector, except for sector 4, only gets one manifold (D or I). In simplest operation one would sequentially do p-i-n-p-i-n in that order in sectors 1 to 6. But by providing an additional manifold to sector 4, we can do 3 p-i-n junctions by rotating substrate back and forth in the sector sequence 1-2-1-3-4-3-6-5-6.

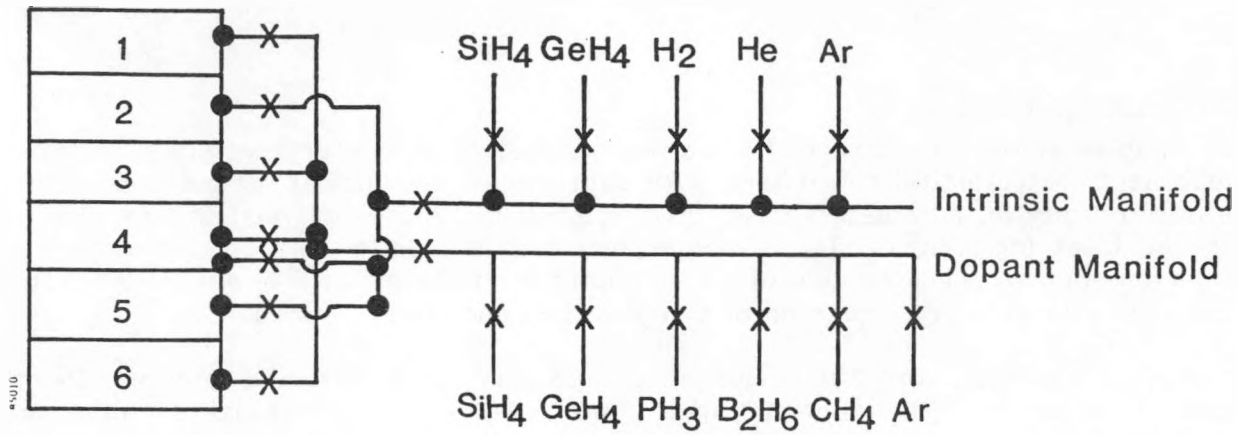

FIGURE 2-7. SCHEMATIC DIAGRAM OF GAS SYSTEM

Gas flow is measured by Unit Instruments mass flow controllers, and shut off by pneumatic valves. All gas fittings are welded Cajon VCR or Parker Ultra-seal. Appropriate filters, regulators, purge assemblies and OSHA approved cabinets are provided.

2.2.4 Power System

The plasma can be either DC or RF. A 3-electrode geometry (see Figure 2-8) is used, so that the plasma is struck between the live electrode and the grounded screen-mesh electrode. The substrate is outside the plasma, and can be independently biased with respect to ground. Electrode-screen and substrate-screen distances are adjustable from 1 to 5 cm.

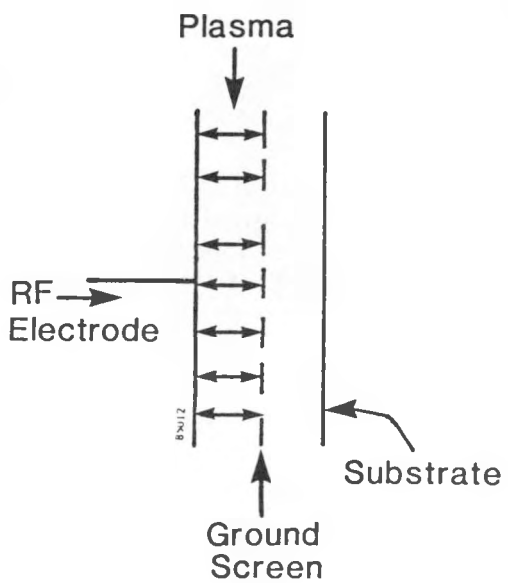

FIGURE 2-8. SCHEMATIC DIAGRAM OF 3-ELECTRODE GEOMETRY

2.2.5 Control System

This complex system was designed for either manual or computer controlled operation. Independent analog/digital controllers, with both manual and digital set point capability, are used to vary all parameters (temperature, pressure, gas flow) requiring sensors and feedback loops for control. The computer serves as a monitor and process sequencer. Hard wired interlocks independent of the computer are installed to shut down the reaction if errors in data entry, the program, or a malfunction endangers personnel.

All process variables, and the status of all gas and vacuum valves, are prominently displayed on or near the control panel (Figure 2-9). During manual or automated operation the gas flow pattern is clearly shown by colored lights, minimizing the possibility of error. The operator can override computer control from this panel, without having to use a keyboard for data entry, providing faster response to emergencies.

Computer controlled operation was not implemented during the 3-year program.

2.2.6 Special Features

The following special features have been provided in this reactor.

- 6 sectors and a load lock.
- Turbomolecular pump.
- Redundant pumping systems.
- 3-electrode geometry.
- Solenoid valves, gas flow control and pressure control.
- Independent manifold for each sector.
- Isolation between dopants and intrinsic gases.
- A well-laid out control panel which visually helps the operator.
- Dual mode control (manual or computer).
- OSHA approved safety cabinets.

2.2.7 Safety

The construction and operation of an a-Si reactor in a safe manner is a matter of crucial importance. Safety has to be built-in, designed-in and not added-on. This issue is so important that we have included a separate appendix (Appendix A) on "Safety Issues in a-Si Deposition". We have implemented most of the suggestions included in Appendix A in our multi-sector reactor.

2.3 TIN OXIDE DEPOSITION CHAMBER

The objective of this effort is to deposit a high transparency, high conductivity, textured tin oxide film on a glass substrate. We have chosen to use the technique pioneered by R. Gordon of Harvard University,[8] namely chemical vapor deposition from tetramethyl-tin. The system described below, fabricated by the end of the second program year, was designed to deposit films on two 100 cm^2 substrates and insure containment of this chemical.

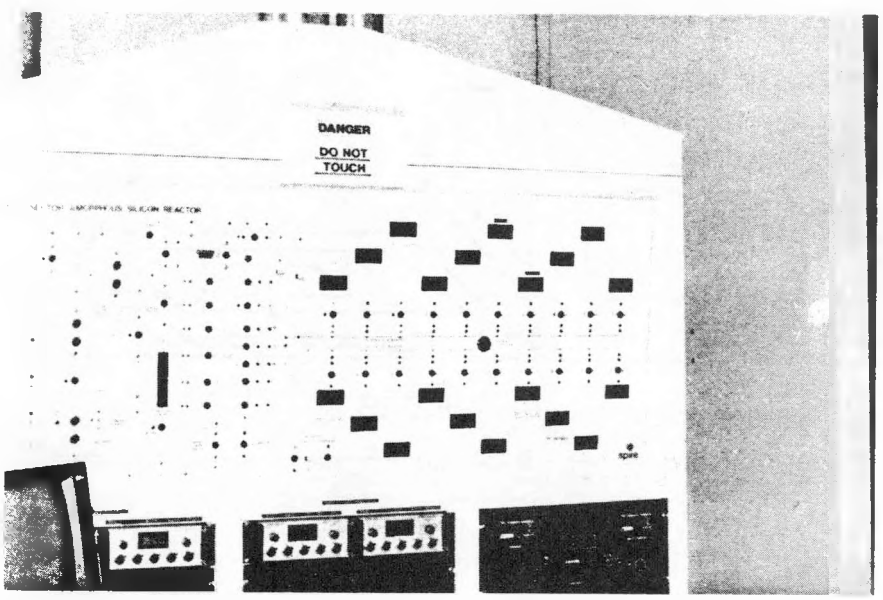

FIGURE 2-9. PHOTOGRAPH OF CONTROL PANEL

2.3.1 Description of the Chamber

A schematic of the deposition chamber constructed by Spire Corporation is shown in Figure 2-10. An outer stainless steel chamber, which can support vacuum inside, is in the shape of an inverted tee. The sample rests on a heater block which can move horizontally at a controlled speed up to 1 cm/sec. The heater temperature is variable. The sample is inserted through a vacuum flange at the right and is heated in place to the desired temperature, then moved to the left under the gas nozzle. Gas enters the chamber through a variable slit in the central nozzle and is pumped out from both ends of the chamber. This arrangement allows us to simulate the deposition process as it would occur in a belt furnace, but in a much smaller space. Additional films, before or after the deposition of tin oxide could be deposited in the same reactor.

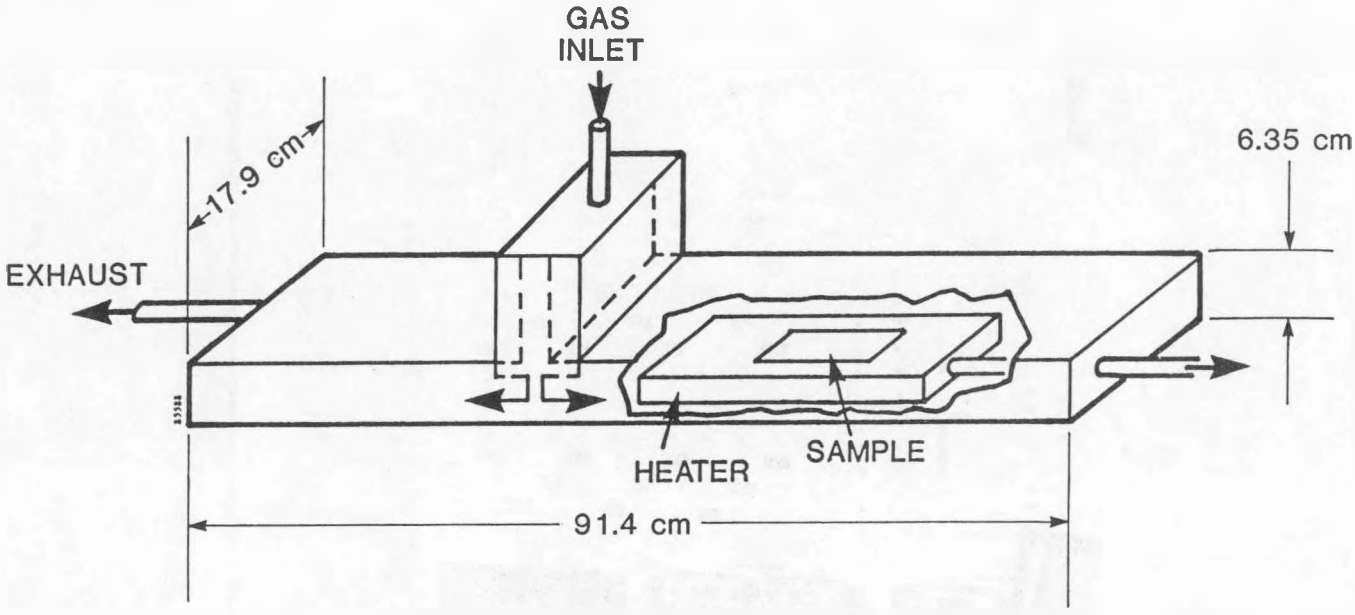

FIGURE 2-10. SCHEMATIC DIAGRAM OF TIN OXIDE DEPOSITION SYSTEM (with interior dimensions).

The gas flow diagram for this reactor is shown in Figure 2-11. Nitrogen, oxygen, and the dopant freon are fed in measured amounts directly to the reactor. The nitrogen flow is broken into two additional, but smaller flow streams which are nominally set to equal levels. One of these smaller flow streams goes to the tetramethyl-tin (TMT) bubbler which is maintained at a constant temperature of 10°C (to prevent TMT vapor condensation in reactor plumbing). The stream of gas exiting the bubbler, and the second small nitrogen flow stream can be interchanged. Either one can flow into a bypass line around the reactor, or into the reactor. Thus, a uniform gas flow pattern at a stabilized pressure can be established in the reactor with a "dummy" nitrogen flow, and a steady stable flow of TMT from the bubble can be established using the bypass without deposition. The "dummy" nitrogen flow and the TMT bubbler output can then be switched rapidly to allow stable deposition without changing the flow pattern established in the chamber. Similarly the TMT flow can be switched very quickly.

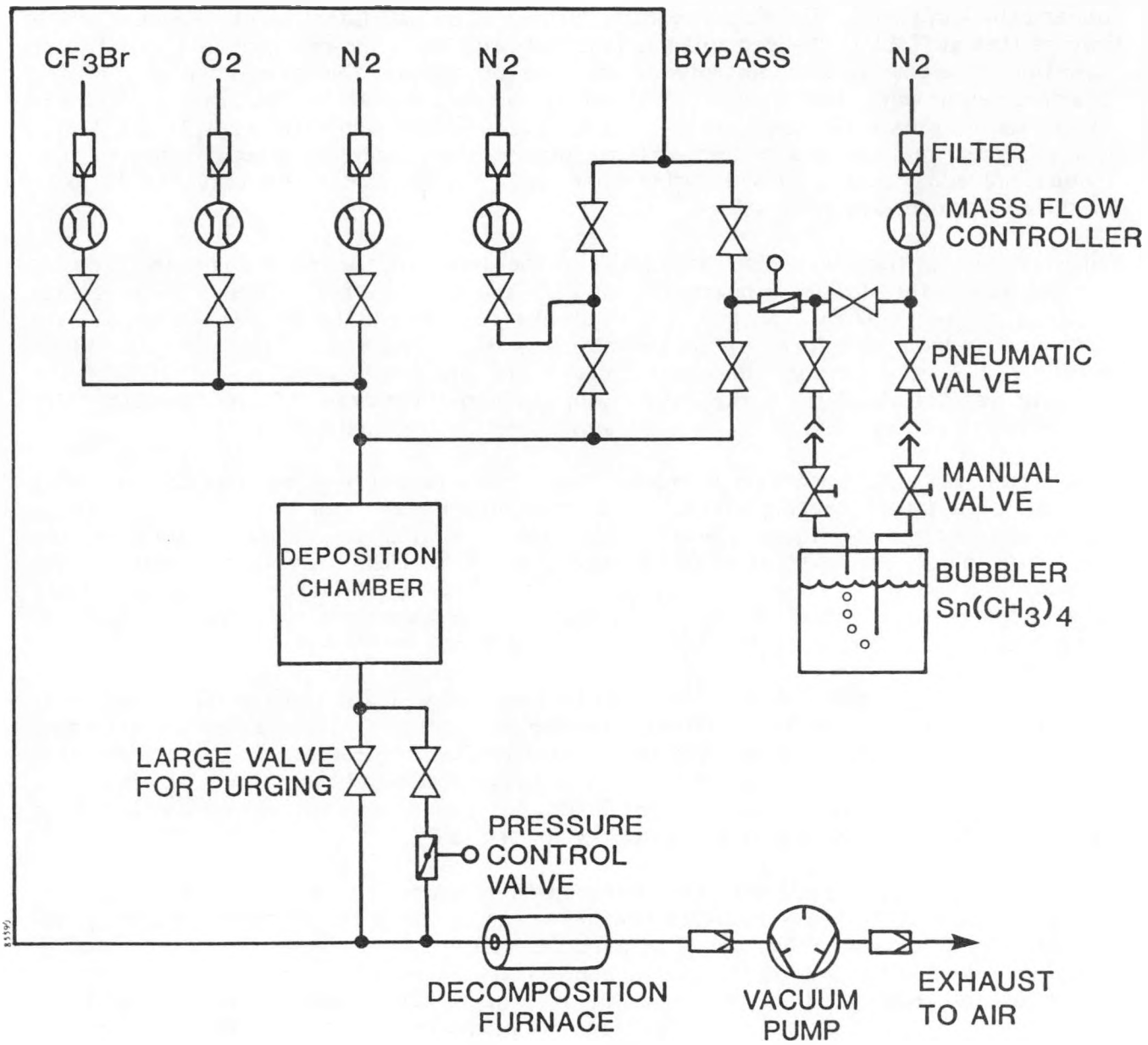

FIGURE 2-11. FLOW DIAGRAM FOR TIN OXIDE DEPOSITION SYSTEM.

The vacuum pump was included as a safety measure. By running the process slightly below atmospheric pressure (600 torr), leaks in the process lines or chamber would be internal and this reduces the possibility of exposing personnel to the highly toxic tetramethyl-tin (TMT). The decomposition furnace is an additional safety measure which insures that all TMT is changed to SnO_2 (and CO_2 and H_2O) and reduces the possibility of harmful emissions to the atmosphere. In case of power failure, residual gas in the chamber can be purged by nitrogen flow and will be decomposed by the furnace which has a high thermal mass and cools slowly. As an added safety precaution the TMT bubbler, gas controls, reactor and decomposition furnace are inside a vented cabinet. The loading/unloading port is closed during operation. Full secondary containment of toxic material is provided by this cabinet.

The initial deposition run showed two flaws in the design of the moving heater. First, it did not reach the design temperature (600°C) and took over two hours to reach its maximum point of 475°C. Second, the insulating feet on this heater were scraped into dust moving back and forth inside the stainless steel chamber. This dust was found downstream in the vacuum lines and clogged the pressure control valve so that the pressure was not stabilized during deposition, but varied between 300 and 800 torr. This is believed to be the cause of the non-uniformity seen in the final film.

The heater was redesigned with a welded, rather than bolted-box, construction, allowing the use of a larger heating element. A transformer was used to boost the voltage available to power the internal heater. The thermal uniformity of the heater was also measured, in open air, using an infrared imaging camera. The temperature variation on a glass sample was $\pm$ 2°C from edge to edge, and better than $\pm$1°C over 90% of the sample at an average temperature of 160°C. At higher temperatures in the enclosed chamber, the percent variation in sample temperature should be reduced.

Additional heaters were added to the external chamber walls of the tin-oxide reactor in Figure 2-10, to increase the maximum sample temperature. The upper limit is now sufficient to warp the glass superstrate (over 700°C). A total of 1200 watts of strip heaters were placed on the upper and lower chamber walls and surrounded by insulation. Maximum wall temperature can exceed 200°C. A linear thermal gradient exists near either end of the reactor due to water cooling for the seals.

The internal walls of the chamber were coated with silica to reduce rust formation. After processing many samples, a rust-like coating began to form on all stainless-steel parts exposed to the hot gases. Non-adhering particles of this coating were also found on some samples. Examination of dust samples showed traces of bromine, implying that the decomposition products of the freon used in the process (CF_3Br) were combining with the oxygen present to attack the stainless steel. A paintable coating was found (ZYP Inc., Tennessee) which was fired and effectively reduced rust formation. Dust formation was also reduced by replacing the insulating legs on the internal heater with stainless steel wheels.

Streaks in the film were eliminated by modifying the nozzle. A cross sectional view is shown in Figure 2-12. The spacing and diameter of holes in the upper plate serve to keep the pressure fairly constant in the plenum. A baffle breaks up gas jets from the fine holes. The final slit is 0.5 mm wide. After deposition, a white powder deposit is found on the outside (i.e., bottom) of the slit plate. This deposit is cleaned off every ten runs. No deposits have been found inside the nozzle.

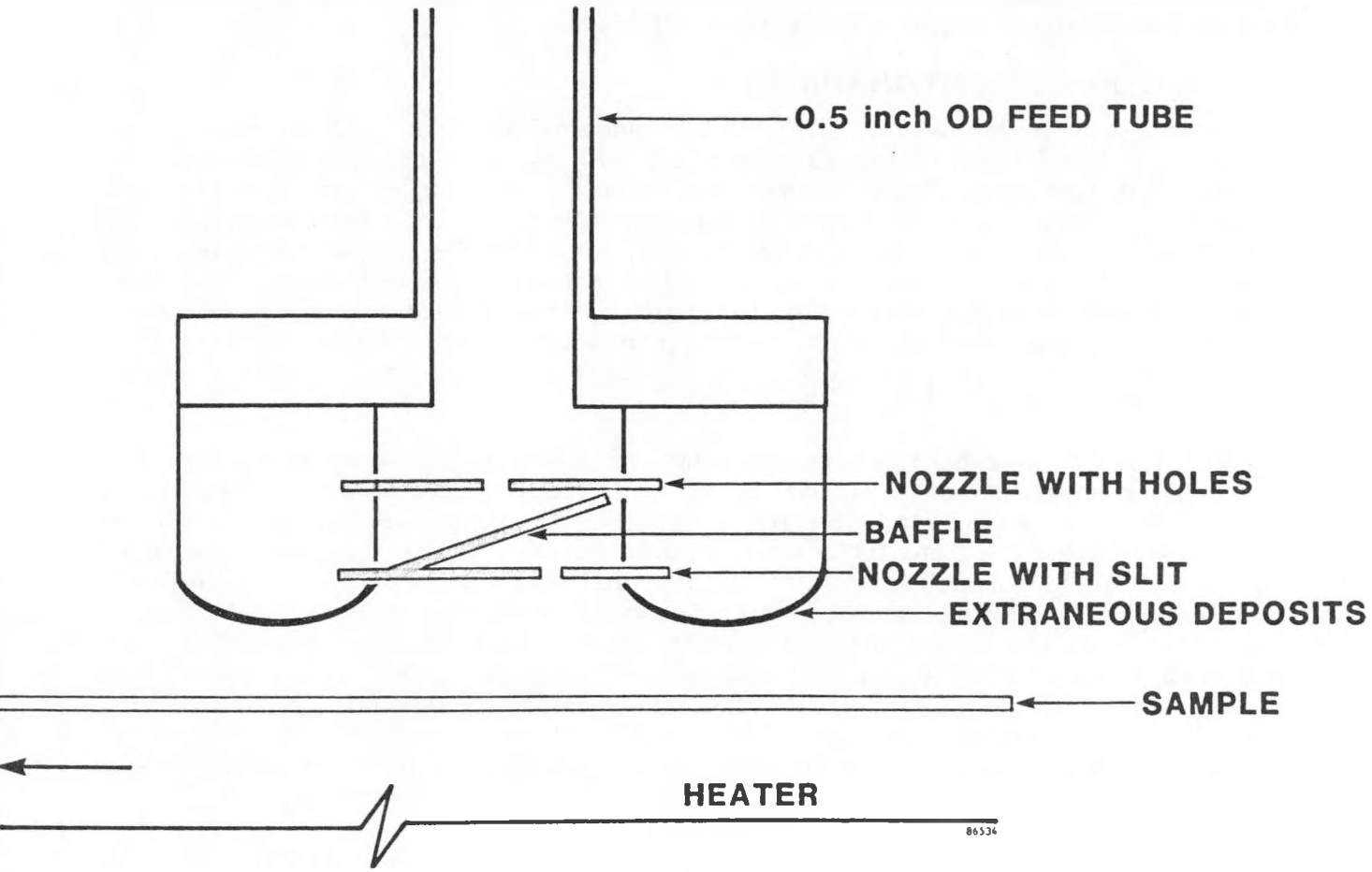

FIGURE 2-12. CROSS SECTION VIEW OF NOZZLE FOR CHEMICAL VAPOR DEPOSITION OF TIN OXIDE.

SECTION 3

SEMICONDUCTOR MATERIALS RESEARCH

Amorphous silicon films were deposited and characterized during this program to help guide the device development effort. Dark and photoconductivities, infrared transmission, Auger analysis, optical transmission and a variety of device measurements were used to evaluate the quality of the films obtained.

3.1 MATERIAL DEPOSITION STUDIES

a-Si:H films of both high bandgap (1.85 eV) and moderate bandgap (1.75 eV) were grown from SiH_4.[5] It was found that H_2 dilution of the SiH_4 gas leads to higher bandgaps. The films had very high photo-to-dark conductivity ratios ($>10^6$), coupled with very low dark conductivities ($<10^{-11}$ S-cm^{-1}). The intensity dependence of the photoconductivity of these films followed a relationship of the form $\sigma_{pc} \sim I^{0.9}$. The high σ factor (slope of log σ vs. log I curve) (0.9) indicates a low defect density on the conduction band side. These films also had sharp valence band tails, with an Urbach edge energy $E_o \sim 43$ meV. The Urbach edge sharpened up, with E_o reducing to ~ 39 meV upon dilution with H_2. The a-Si:H films had electron ($\mu\tau$) products in the range of 4×10^{-7} cm^2/V, and hole ($\mu\tau$) products in the range of 4×10^{-8} cm^2/V.

a-(Si,Ge):H films, with bandgaps in the range of 1.42-1.70 eV were grown by glow discharge decomposition of SiH_4 and GeH_4.[1] A study of H-bonding of these films revealed that films which were subjected to negative bias during growth tended to have few SiH_2 bonds, but the films subjected to positive voltage bias during growth tended to have significant SiH_2 bonding. A study of dark and photoconductivities of a-(Si,Ge):H films, deposited at 300°C, revealed that dark conductivity increased with decreasing bandgap, and that photoconductivity decreased with decreasing bandgap (Figure 3-1). The dark conductivity of films grown at 250°C however, remained constant as a function of bandgap (Figure 3-2). Electron ($\mu\tau$) products showed a systematic decrease with increasing Ge content (reduced bandgap). The Urbach edge energy E_o, a measure of disorder, increased with increasing Ge content. The inclusion of H_2 in the discharge gas mixture decreased E_o by about 3 meV. Increasing temperature increased E_o.

A plasma-gettering process was developed for gettering impurities such as H_2O and B_2H_6 from the walls of the reactor. This process relies on depositing a-Si:H films on the electrodes and walls to getter impurities. The process has allowed us to deposit high quality materials (a-Si:H and a-(Si,Ge):H) and devices (a-Si:H, a-(Si,Ge):H, and tandem cells).

3.1.1 Deposition of Pinhole-Free a-Si:H Alloy Films

A key problem encountered in attempting to fabricate high quality a-Si:H alloy devices is dust formation in the plasma. This is caused by the nucleation of the various SiH_n-type radicals at the relatively high pressures employed, typically well above 100 mtorr.

Excessive dust has two negative consequences: first, dust particles are incorporated into the layers, leading to device shunting. This prevented us from obtaining high-efficiency devices of over 0.1 cm^2 area. Second, the need to open the vacuum chamber of our multi-chamber deposition system after every run, to remove the accumulated dust, rendered the load-lock chamber useless in preventing atmospheric contamination of the vacuum environment.

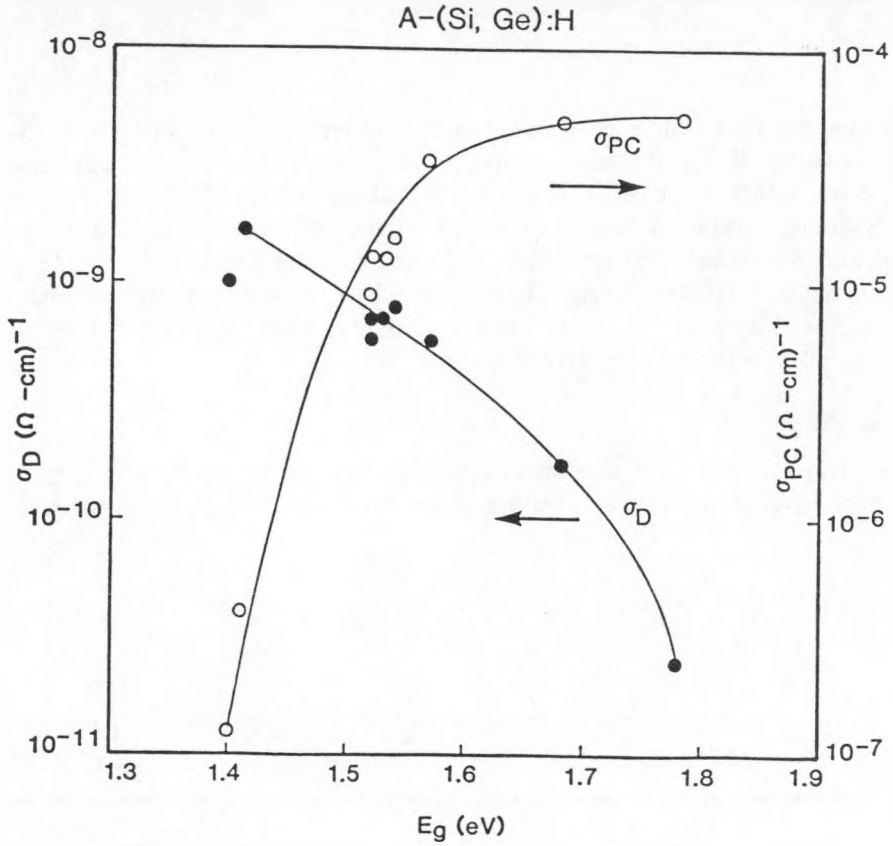

FIGURE 3-1. DARK AND PHOTOCONDUCTIVITY OF a-(Si,Ge) FILMS DEPOSITED AT 300°C.

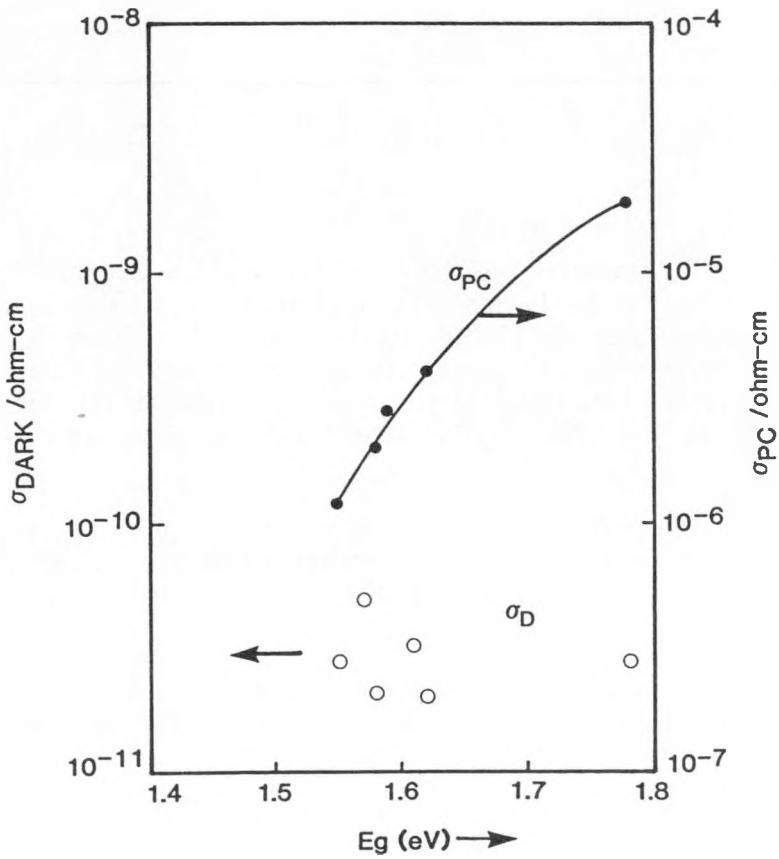

FIGURE 3-2. DARK AND PHOTOCONDUCTIVITY FOR a-(Si,Ge):H FILMS DEPOSITED AT 250°C.

An attempt was made to reduce the shunt area density by growing all the a-Si:H alloy layers at low pressure (LP), namely below 100 mTorr. In this approach, the plasma parameters were adjusted to obtain high quality alloys with relatively low defect density. Feedback on materials quality was obtained from device data. In what follows, we present process and materials information on the various a-Si:H alloy layers obtained in the course of device optimization. The materials described were deposited in the multi-sector reactor (Section 2), with which the highest quality films were obtained. Device data will be presented in Sections 5.2 and 5.3.

3.1.2 a-Si:H i-Layers

Typical values of the RF power W_{rf}, substrate bias V_b, pressure P, temperature T, and gas flow rates leading to high and low pinhole densities in a-Si:H i-layers are compared in Table 3-1.

TABLE 3-1. PROCESS PARAMETERS OF TYPICAL a-Si:H i-LAYERS WITH HIGH (HPD) AND LOW (LPD) PINHOLE DENSITIES.

Sample	P (mTorr)	T (°C)	W_{rf} (W/cm^2)	V_b (V)	(SiH_4) Flow Rate (sccm)	Growth Rate (Å/s)	Comments
20414	100	275	0.18	-10	15	0.9	HDD
20589	30	275	0.18	-10	20	0.9	LDD

High pinhole density (HPD) material typically exhibited areas with over one pinhole per cm^2, while low pinhole density (LPD) material was virtually pinhole free. No extensive effort was made to further quantify pinhole density, except to observe that 0.5 and 1.0 cm^2 area devices with shunt resistances over 500 ohm cm^2 could be easily fabricated only in the pinhole-free material. This facilitated the achievement of efficiencies in excess of 10 and 9% respectively for 0.5 and 1.0 cm^2 a-Si:H p-i-n devices, as reported in Section 5.2.9.

No reliable conductivity data are available for films grown during the last six months of this effort. From the high device efficiencies obtained (Section 5.2.9), we presume that photo-to-dark conductivity ratios are at least comparable to the previously obtained values exceeding 10^6.

Finally, optically determined band gap values for this material were in the range 1.75 to 1.80 eV (Figure 3-3). This makes it an appropriate material for the top cell in a tandem structure.

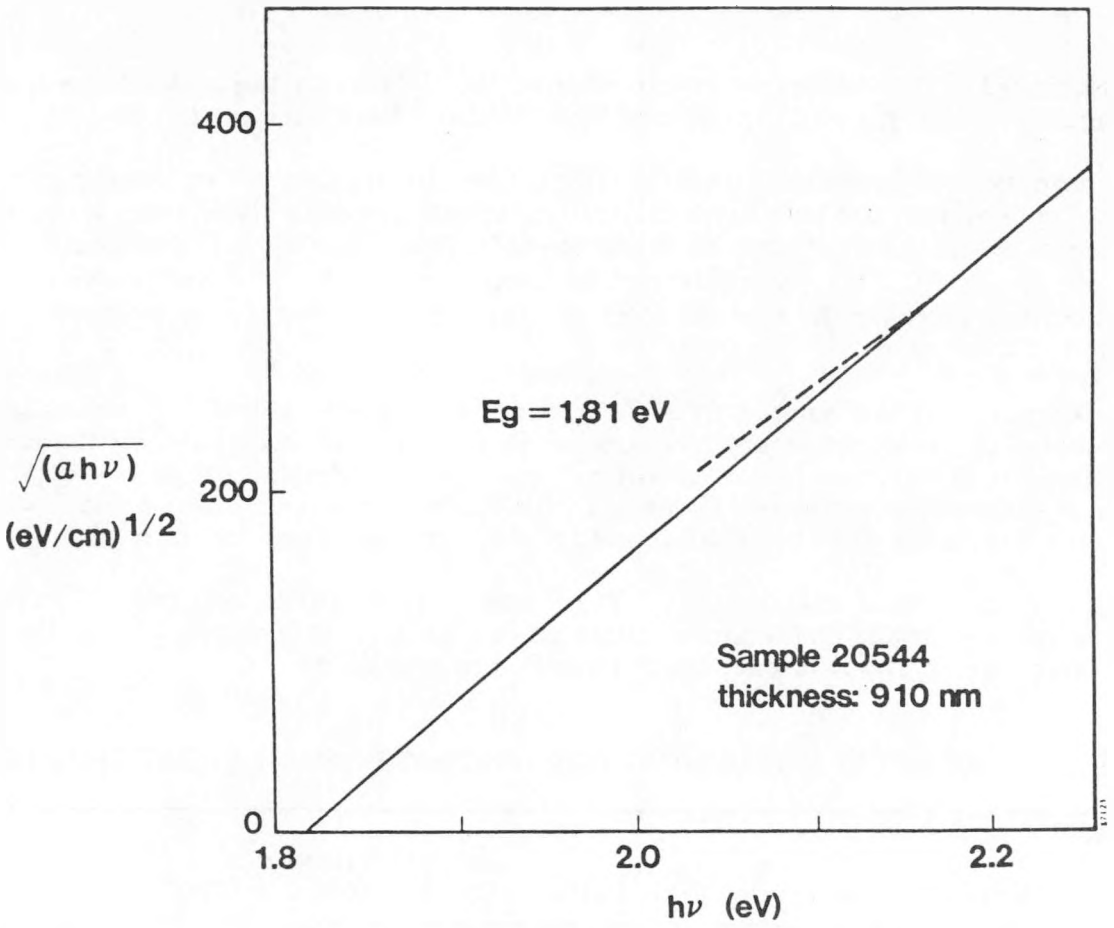

FIGURE 3-3. TAUC PLOT FOR TYPICAL i-LAYER.

3.1.3 P- and N-Layer Optimization for a-Si:H

The desired characteristics of p^+- and n^+-layers are high conductivity and optical transmission. Deposition at lower pressures can change both optical and electrical properties of such layers. In what follows, we describe the process optimization of both layer types to obtain high device open-circuit voltage and short-circuit current under low dust deposition conditions.

When p^+-layers were initially grown under low pressure conditions (<100 mTorr), p-i-n a-Si:H devices with low V_{OC} were obtained (see Section 5.2.2). This was attributed to low p^+-layer conductivity. Several depositions of single p^+-layers at low pressure were carried out in an attempt to obtain higher conductivity. The CH_4, H_2 and B_2H_6 fractions in the input gas flow were varied, as well as the RF power W_{rf}. Thicknesses were measured ellipsometrically and refractive indices were also obtained.

When conductivity was measured, the values obtained were very low $\leq 10^{-5}$ S cm^{-1}, independent of the process conditions. This was expected of low-pressure p^+-layers, but was also observed for the standard high-pressure (> 100 mTorr) process. Analysis of this problem shows that an adsorbed surface charge layer of density Σ_s(cm^{-2}) could induce a majority carrier depletion region in the a-Si:H p^+-layer of width ∂ given by:

$$\partial = \Sigma_s / N_b \approx 1 \ \mu m$$

where $N_b(cm^{-3})$ is the density of electrically active defects in the bulk of the p^+-layer and typical values of $\Sigma_s = 10^{15}\ cm^{-2}$ and $N_b \approx 10^{19} cm^{-3}$ have been used.

Under these typical conditions surface effects due to physisorbed or chemisorbed gas layers could dominate the bulk conductivity unless samples with thicknesses in excess of 1 μm were used. All our samples were made thinner (<200 nm) and could not be accurately measured. This was confirmed by measurement of a p^+-layer in vacuum, i.e., the conductivity increased by over an order of magnitude as compared with measurements conducted in ambient air.

Consideration of our low sample throughput and the problem in applying data from 1μm thick samples to the development of optimum 10 nm thick p^+-layers led to the decision not to fabricate the thicker samples. Instead, use of device data to optimize the p^+-layer deposition process resulted in a-Si:H devices with V_{oc}'s in excess of 900 mV and J_{sc}'s over 17 mA/cm^2, indicating good conductivity and p^+-layer transparency (Section 5).

In Table 3-2 the typical values of W_{rf}, V_b, P and T of high (HP) and low (LP) pressure p^+-layers prepared under identical conditions as in high V_{oc} devices are given. Thickness t, refractive index n at 633 nm,and optical gap E_g are also given.

TABLE 3-2. PROCESS AND OPTICAL PARAMETERS FOR p^+-LAYER DEPOSITION.

Sample	P (mTorr)	T (°C)	W_{rf} (W/cm^2)	V_b (V)	Flow Rates (sccm) (SiH_4)	(H_2)	(CH_4)	(PH_3)	t (nm)	n (-)	E_g (eV)
20440	200	210	0.13	-10	20	30	15	10	126	2.75	-
20461	84	210	0.15	-10	20	30	15	10	175	2.81	2.34
20445	85	210	0.18	-10	20	30	15	10	169	2.93	2.47

Use of values of W_{rf} lower than those in Table 3-2 resulted in devices with lower V_{oc}.

Optical band gap measurements of p^+-layers yielded values in the range 2.2-2.5 eV, depending on preparation conditions. Data for sample 20461 can be seen in Figure 3-4. While this value of E_g is still somewhat low and values approaching 3.0 eV would be preferable, thin p^+-layers around 15 nm can be successfully utilized in p-i-n devices.

The same considerations apply to conductivity measurements of n^+-layers. The corresponding data for a low pressure n^+-layer are summarized in Table 3-3.

TABLE 3-3. PROCESS AND ELLIPSOMETRIC PARAMETERS FOR n^+-LAYER DEPOSITION.

Sample	P (mTorr)	T (°C)	W_{rf} (W/cm^2)	V_b (V)	Flow Rates (sccm) (SiH_4)	(H_2)	(PH_3)	t (nm)	n (-)
20454	75	325	0.21	0	20	20	20	146	3.64

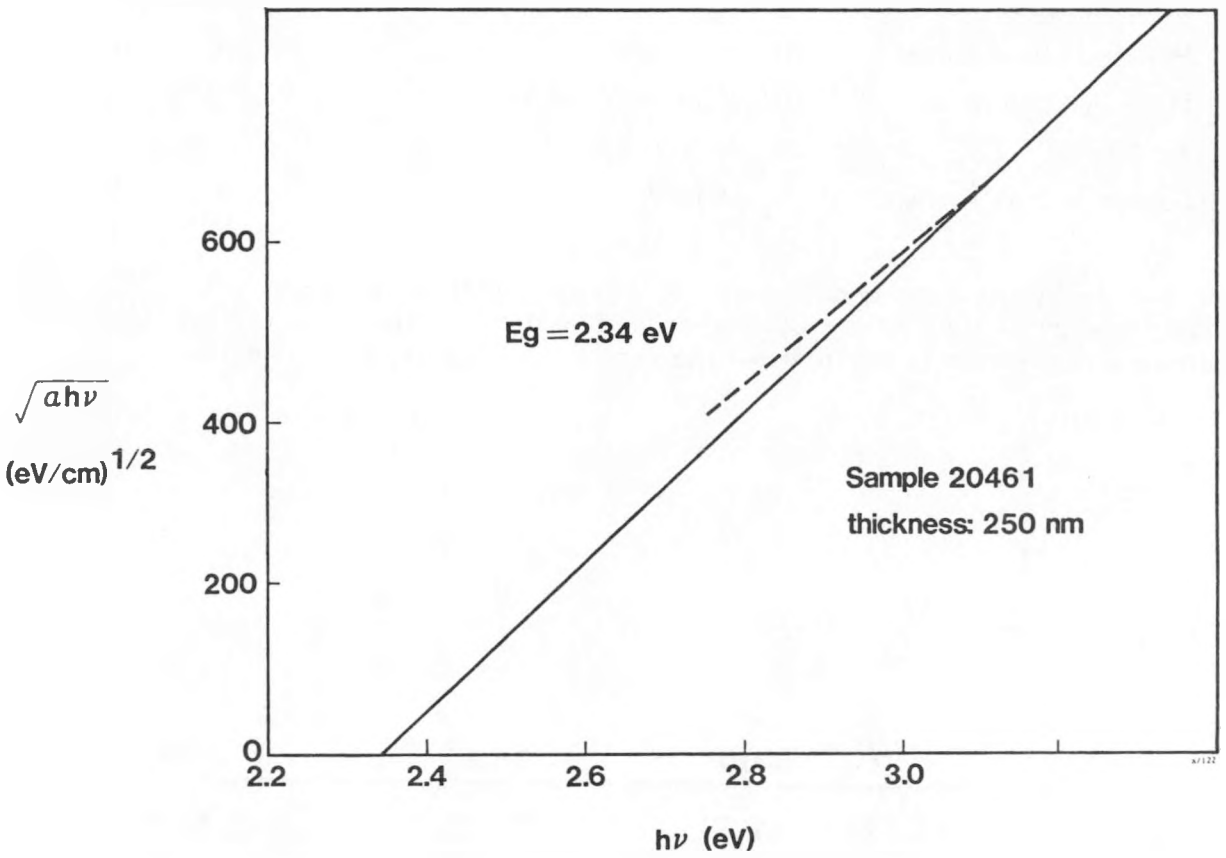

FIGURE 3-4. TAUC PLOT FOR p^+-LAYER

3.1.4 a-(Si,Ge):H Alloys

The p^+-, i-, and n^+-layer processes described in 3.1.1 and 3.1.2 were taken as baseline processes in the ensuing development of single-junction and multi-junction devices during the last half of Phase III. The strong device basis of the analysis guiding this development suggests that this material can be best reported under Section 5. However, optical and conductivity data for an a-(Si,Ge):H sample prepared under the optimum conditions discussed in Section 5 will be reported here.

The sample was grown by plasma decomposition of SiH_4 and undiluted GeH_4. The growth parameters for this sample are as follows (see Section 5.3.1):

Total System Pressure:	P = 65 mTorr
Substrate Temperature:	T = 350°C
Total Flow Rate:	Q_t = 72 sccm
Silane flow Rate:	(SiH_4)= 40 sccm

Germane Flow Rate:	(GeH_4) = 12 sccm
Hydrogen Flow Rate:	(H_2) = 20 scm
Hydrogen Dilution:	$(H_2)/(SiH_4 + GeH_4)$ = 0.4
RF Power:	W_{rf} = 0.10 W/cm^2
Substrate Bias Voltage:	V_b = -10 V

Figure 3-5 shows the dark conductivity of sample 20530 as a function of $10^3/T$. An activation energy of 0.62 eV is obtained from the slope of this plot. Optical band gap measurements are shown in Figure 3-6. The data are summarized in Table 3-4.

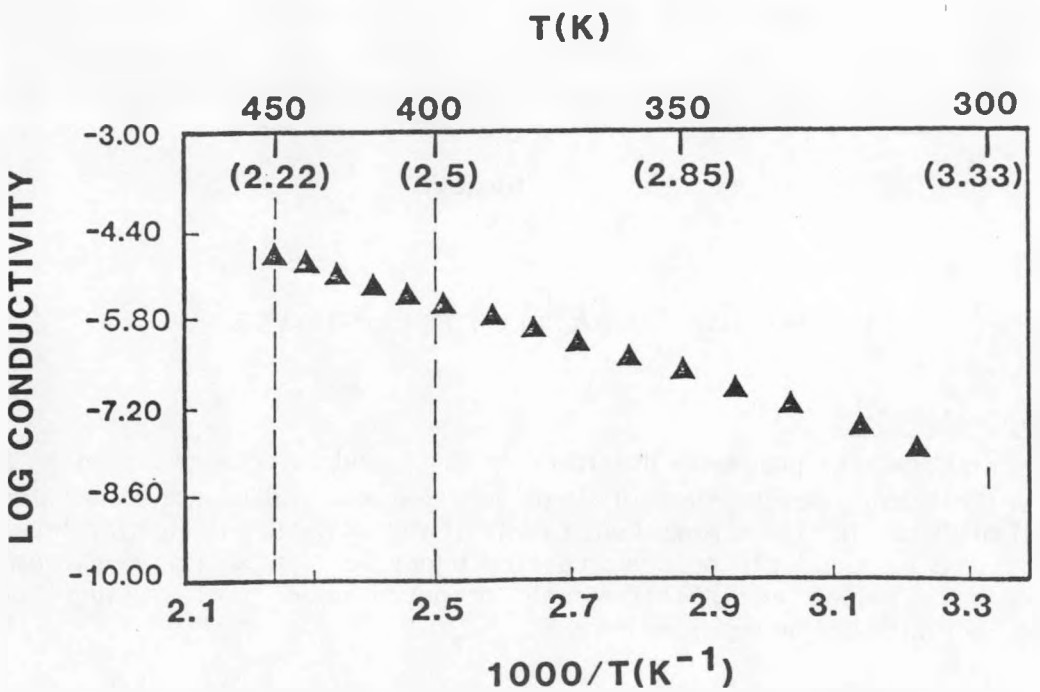

FIGURE 3-5. DARK CONDUCTIVITY σ vs. 1000/T FOR a-(Si,Ge):H i-LAYER OF E_g = 1.45 eV.

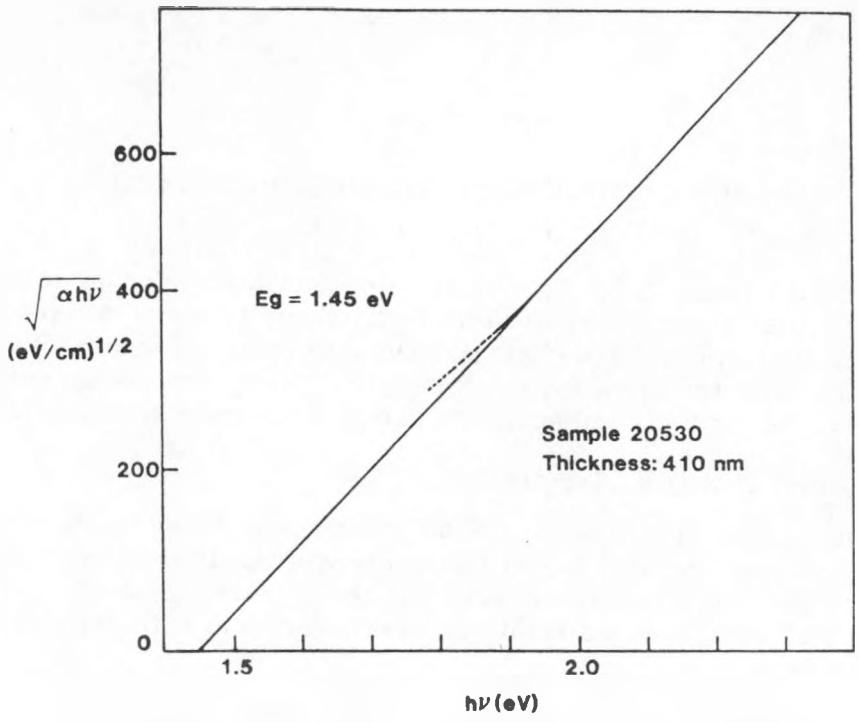

FIGURE 3-6. TAUC PLOT FOR a-(Si,Ge):H i-layer.

TABLE 3-4. ELECTRICAL AND OPTICAL PROPERTIES OF LOW BAND GAP a-(Si,Ge):H ALLOY. Sample thickness is 400 nm

Sample	Dark Conductivity S cm^{-1}	Photo Conductivity S cm^{-1}	Ratio (-)	Activation Energy (eV)	Optical Gap E_g (eV)
20530	1.05×10^{-8}	2.16×10^{-6}	2.06×10^{2}	0.62	1.45

A comparison with Figures 3-1 and 3-2 shows that the dark conductivity of sample 20530, grown at a substrate temperature of 350°C, exceeds the values obtained in samples of comparable bandgap deposited at 250 and 300°C. Photoconductivity values, on the other hand, are comparable to those of the 300°C samples and higher than those of the 250°C samples.

This is consistent with the data in Figures 3-1 and 3-2, which suggests that as substrate temperature increases, the structural disorder introduced by Ge tends to decrease, while rapid H_2 evolution beginning at ca. 325°C introduces additional bonding defects to yield an optimum deposition temperature above 300°C.[9]

We also note that, besides substrate temperature, the optimum deposition conditions developed in the last half year of this program to yield minimum dust formation are different to those used in the deposition of the samples in Figures 3-1 and 3-2, which involved pressures in the range of 200-300 mTorr, a much higher H_2 dilution $(H_2)/(SiH_4) + (GeH_4) = 6\text{-}7$ and the use of GeH_4 diluted to 10% in H_2.[9] Further discussion of the effect of H_2 dilution will be presented in Sections 5.3.1 and 5.3.2.

SECTION 4

NON-SEMICONDUCTOR MATERIALS RESEARCH

As discussed in greater detail in Section 5.2.4, an optical model for an amorphous silicon solar cells suggests that major losses in overall efficiency result from optical absorption in the SnO_2 front and aluminum back contacts and from total reflection. The objective of this task was to develop textured, highly transparent SnO_2 and highly reflecting Ti/Ag bi-layer contacts as the most fruitful approach to high efficiency a-Si:H cells.

4.1 TRANSPARENT CONDUCTIVE OXIDE

The front contact to an amorphous silicon solar cell must be highly conductive, transparent, and non-reactive with a-Si:H during deposition. It should not act as a source of diffusing impurities. Indium tin oxide (ITO) has the greatest value of conductivity for a given transparency of any known material. However, it reacts with a-Si:H at the required deposition temperature.

Searching the literature we determined that the next best candidate material is SnO_2, which can be doped with flourine or chlorine and deposited with appropriate texture. Initial sample lots of glass coated with SnO_2 deposited by pyrolysis of a water solution of tin chloride on a production line were not uniform nor reproducible. Therefore we chose to make our own coatings of SnO_2 using the technique pioneered by R. Gordon of Harvard University,[8] chemical vapor deposition from tetramethyl-tin. This organio-metallic compound poses a severe safety hazard,[10] and the deposition system described in Section 2 was designed to insure containment of this chemical.

During the last six months of this program significant progress was made in reproducibly depositing textured tin oxide films on Corning 7059 low sodium glass superstrates. The typical film is characterized by:

- 4 x 4 inch area
- 10 ohms/square sheet resistance
- Optical absorption under 5% between 500 nm and 700 nm
- Surface texture, or feature size, approximately 500 nm
- Film thickness approximately 2 micrometers
- Thickness and resistivity uniformity better than 10%
- Uniformity of texture and diffuse transmission, better than 10%
- Surface imperfections less than $30/cm^2$
- Increase in cell J_{sc} (relative to planar SnO_2) of over 20% (Section 4.2.8).

Previous experiments had demonstrated films with the correct texture, resistivity, and optical transparency in limited areas. The reproducible fabrication of uniform films increased cell efficiency during this time period.

4.1.1 Deposition Process for SnO_2 on Glass

The gases used in this process are nitrogen, oxygen, freon 13B1 (CF_3Br) and tetramethyltin (TMT or $Sn(CH_3)_4$). The adjustable flow range for these gases in our equipment is given in Table 4-1. Parameters used to deposit specular and textured films are given in Table 4-2. The temperature of the glass substrate during deposition exceeded 621°C as determined by melting point standards placed on the substrate. Thermocouple readings of the heater block gave varying results depending upon position and were not accurate measurements of sample temperature; however, one thermocouple was used to control repeatability of the process.

4.1.2 Two Layer Coatings

At the start of May 1986, reproducible coatings of textured tin oxide were deposited on Corning 7059 substrates using high oxygen content gas streams. These coatings were always non-uniform with the greatest texture at the back of the substrate (back and front are relative to direction of motion under nozzle). The effect was believed to be caused by non-uniform nucleation of SnO_2 on silica. Specifically, gas flowing over the back of the substrate before reaching the nozzle contained a very low concentration of tin which led to a small concentration of stable nucleii on the substrate. These nucleii would grow and prevent further nucleation of grains, eventually leading to a large-grain, rough film. The front part of the glass, in a gas stream with a high concentration of tin, would have a high nucleus density initially and develop a finer grain-size, smoother film.

TABLE 4-1. RANGE OF EXPERIMENTAL PARAMETERS

Oxygen Flow	250 to 5000 sccm
Nitrogen Flow	250 to 5000 sccm
Nitrogen Flow in Bubbler	25 to 500 sccm
Freon (CF_3Br) Flow	10 to 200 sccm
Sample Temperature	20 to 750°C
Wall Temperature	20 to 200°C
Chamber Pressure	20 to 750 torr
(600 torr in all cases but specific low pressure tests)	
Bubbler TMT Pressure	700 torr always
Bubbler Temperature	10°C always
Partial Pressure TMT at 10°C	56 torr
TMT in Gas from Bubbler	8%

TABLE 4-2. COATING PARAMETERS

Sample # Description	SN0045 specular	SN0047 "heavy" texture	SN0054 "light" texture
Sheet Resistance (Ω/□)	23	14 to 18	10 to 13
Optical absorption (%) at 600 nm	2	14	5
Film Thickness (μm)	0.1	3.0	1.5 to 2
Oxygen flow (sccm)	800	3200	3200
Nitrogen flow (sccm)	3000	660	640
CF_3Br flow (sccm)	80	64	64
TMT flow (sccm)	8	5	5
Sample speed (cm/min) past nozzle	19.1	1.6	2.4

Uniformly textured film was achieved by depositing the tin oxide in two passes. The first layer was a specular film approximately 100 nm thick, highly doped (20 ohms/square) and deposited quickly. Moving the substrate at high speed through the nozzle prevented early grain growth from dominating final film parameters. Subsequent growth on a tin oxide coated substrate showed uniform grain size even though the substrate was moved slowly to deposit a thick film. In Table 4-2 the textured films were deposited on top of the specular film indicated.

Towards the end of the program, a concerted effort was made to achieve high efficiency a-Si:H cells. To this end, a series of runs were made in which the SnO_2 texture was varied by controlling the thickness of the top layer. Due to time constraints, it was not possible to quantify layer texture, and only visual evaluation was used to direct experimentation. However, it was generally found that texture increased with the SnO_2 layer thickness. The preferred texture, as revealed by scanning electron microscopy, will be discussed in 4.1.5.

4.1.3 Measurement of Optical Properties

The total optical transmission of textured films was measured as a function of wavelength using an index-matching fluid, hydrogenated terephynol diodomethane, placed between the tin oxide and a covering microscope slide. The reduction of haze when looking through the textured tin oxide, compared to the surface when covered with this special fluid, was visually striking (Figure 4-1). The percent of diffuse optical transmission through this combination was measured with a haze meter and found to be negligible. Comparing the total transmission to that of just the glass substrate, plus liquid and slide, enables accurate computation of the absorptivity of the tin oxide, (Figure 4-2), as shown in Table 4-2.

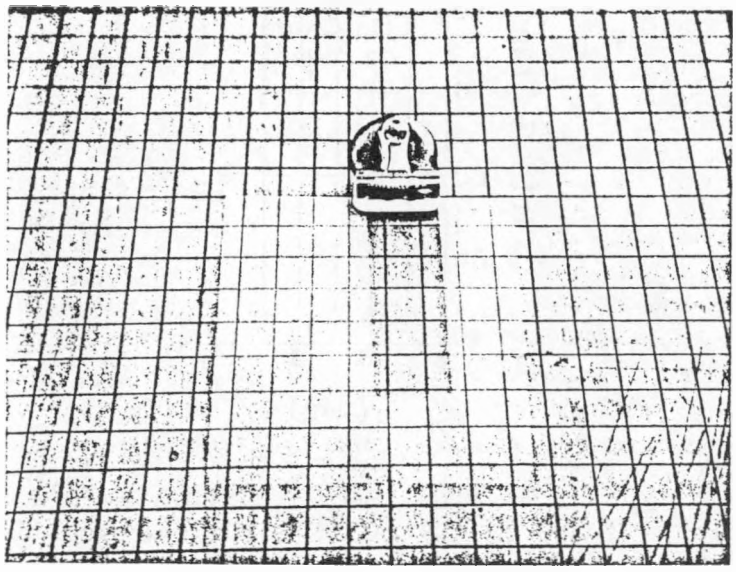

FIGURE 4-1(a). EFFECT OF INDEX-MATCHING FLUID. (Note clarity looking through slide, 0.5 inch squares.)

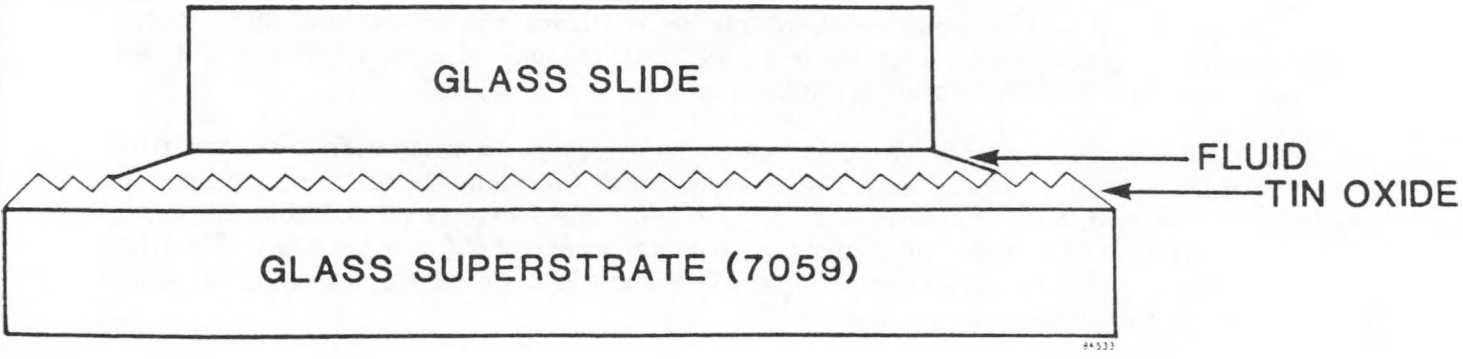

FIGURE 4-1(b). GEOMETRY USED IN FIGURE 4-1(a).

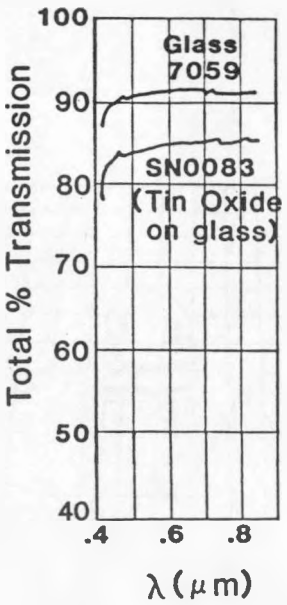

FIGURE 4-2. TRANSMISSION THROUGH SnO_2 ON GLASS (Sample SN0083) AND THROUGH (7059) GLASS ALONE WITH INDEX-MATCHING FLUID (FIGURE 4-1).

Typical total transmission and reflection measurements of a highly textured film made with an integrating sphere but not using the index-matching fluid are shown in Figure 4-3. The estimated absorptivity of the film determined from Figure 4-3, A = 1-R-T, is much greater than the value of A determined by the use of the index matching fluid, Figure 4-2. Light trapping in the film is believed to lower the measured transmission even when the sample was closely coupled to the integrating sphere. The data in Figure 4-3 were taken with a two-inch diameter integrating sphere mounted on a spectrophotometer. Another measurement using broad band interference filters and an eight-inch diameter integrating sphere gave similar results, implying that the use of a small sphere did not cause the inaccuracy in transmission measurements.

The uniformity of film thickness was determined by mapping the reflection from the film over the 4 inch x 4 inch surface at a single wavelength (677 nm, HeNe laser). A typical map of a good sample, SN0083, is shown in Figure 4-4. One fringe is identifiable, implying a thickness variation of 185 nm for an average film thickness of 2.0 micrometer. The film non-uniformity is $\pm$ 5% for this case and the difference in average thickness is less than the microscopic roughness seen in Figure 4-5.

4.1.4 Physical Measurements

An analysis of the film listed in Table 4-2 was made by scanning electron microscope (SEM) to determine grain size and chemical composition. Figure 4-5 (a,b,c) shows the specular, medium textured, and rough textured films respectively. The nominal grain size increases from 100 nm to 500 nm to over one μm. The roughest film resulted in all-shorted cells. The highest cell efficiency, over 11%, was achieved by deposition on a film that could be described as having medium texture.

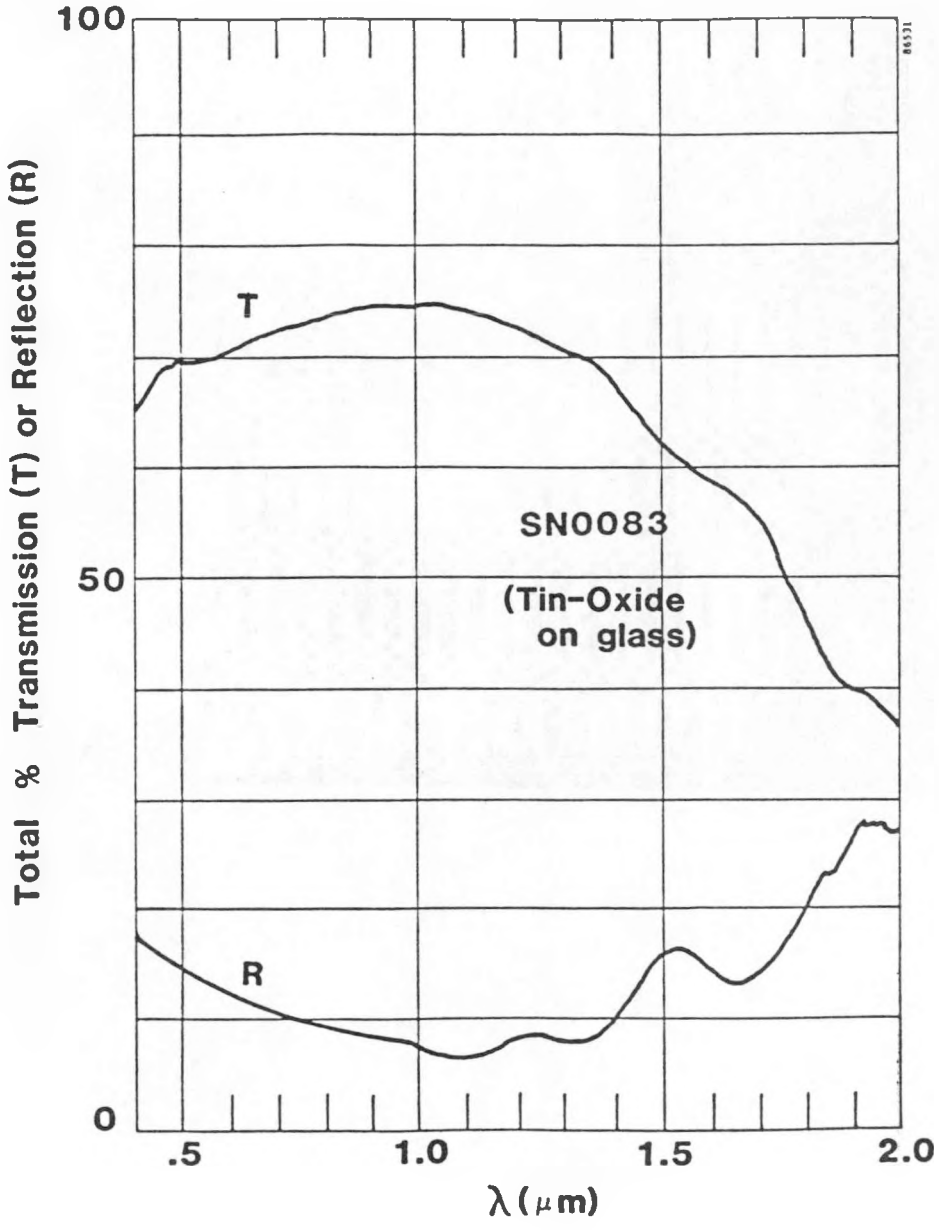

FIGURE 4-3. DIRECT TRANSMISSION (T) AND REFLECTION (R) FROM DIFFUSE TIN OXIDE SAMPLE (SEE FIGURE 4-3) WITHOUT INDEX-MATCHING FLUID.

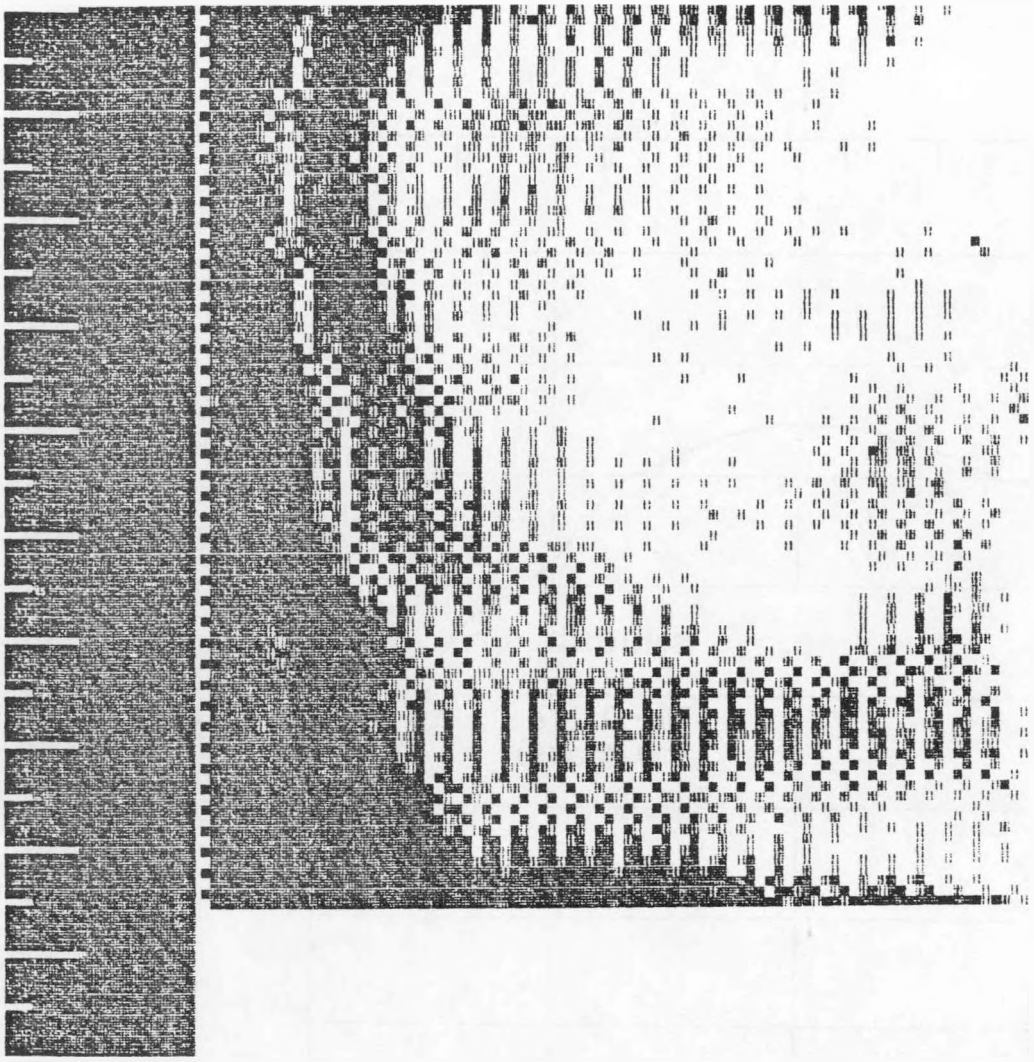

OF X POINTS = 88.5

OF Y POINTS = 87.5 NEW VALUES OLD VALUE

LASER OUTPUT VALUE IS 4095 INPUT LOWEST % VALUE? .2

TOTAL POINTS ARE 7744 .4

cell number and position is SNOO83R .6

FIGURE 4-4. REFLECTOMETER SCAN OF SNOO83 (Textured tin oxide on glass.)

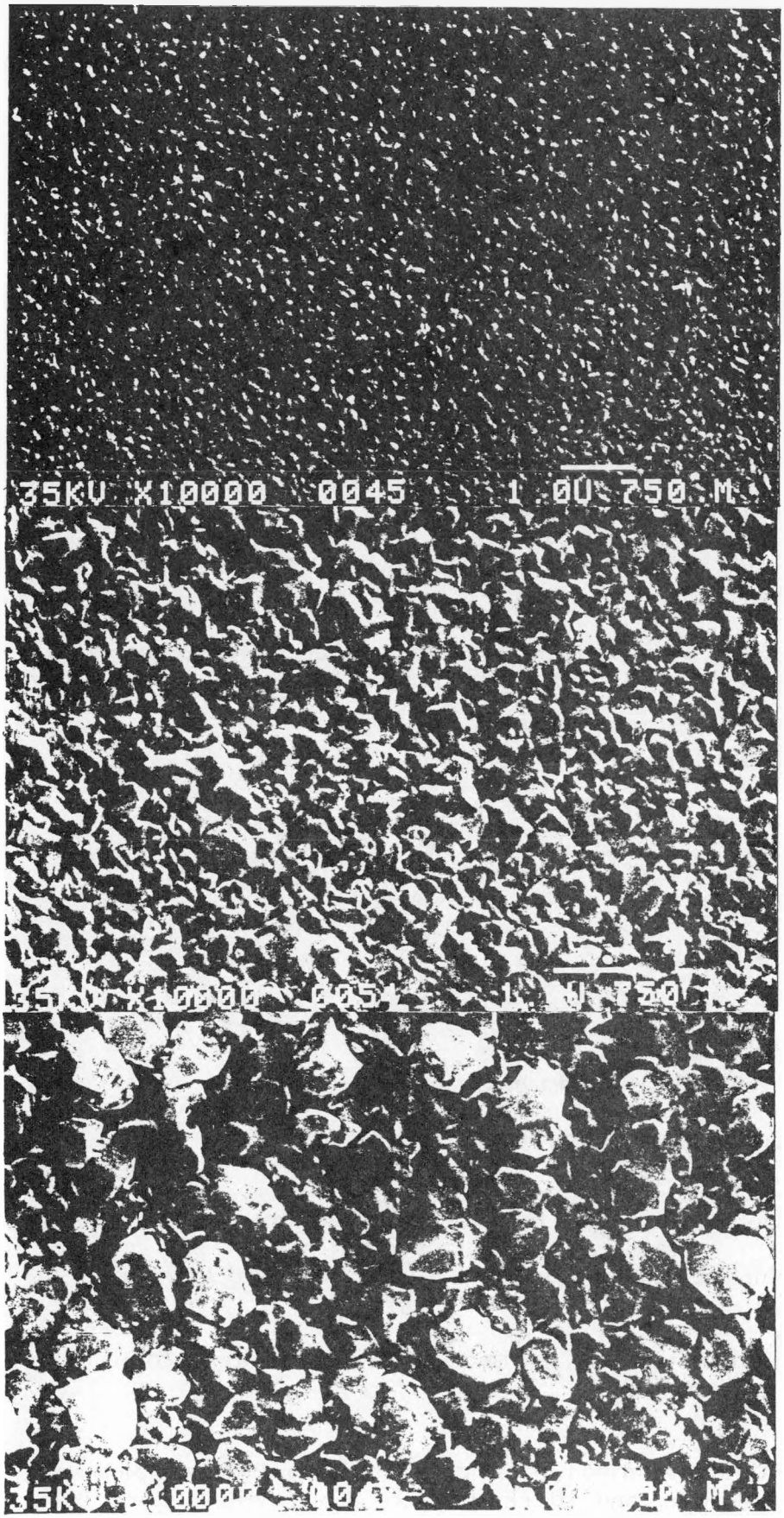

a) Specular SN0045

b) Medium Textures N0054

c) Heavy Texture SN0047

FIGURE 4-5. SCANNING ELECTRON MICROGRAPHS OF TIN OXIDE AT 10,000X.

The chemical composition of particles found on some films was examined by energy dispersive spectroscopy EDS in an SEM (Figure 4-6.) The particle is tin, plus oxygen not detectable by EDS. Apparently the process coated a "foreign" particle on the substrate, creating a high point, which could short out a cell, surrounded by a region of thinner tin oxide. These denuded regions have been observed to be as large as 5 mm in diameter. These defects were eliminated by better cleaning procedures for the substrate and by coating the deposition chamber with a silica-rich compound.

Another type of mechanical defect found in tin oxide films is shown in Figure 4-7 by optical photomicrographs at a magnification of 50X. The black specks are gouges or craters in the glass surface, more obvious at high magnification. Figure 4-7(a) is typical of films produced at Spire. The sample had to be moved around to find any defects, which have an average density much less than $50/cm^2$. Figure 4-7(b) is a similar image of an NSG (Nippon Sheet Glass) sample which could not be used as the defect density approaches $10{,}000/cm^2$. All cells on such a substrate were shorted out. Quality control inspection under an optical microscope at 50X was found to be necessary for all samples. Not all NSG samples were bad.

4.2 DIFFUSON OF IMPURITIES ACROSS THE TIN OXIDE/a-Si:H AND a-Si:H/METAL BACK CONTACT INTERFACES

Tin oxide films deposited at Spire were analyzed by Scanning Auger Microprobe (SAM), Secondary Ion Mass Spectroscopy (SIMS), and Rutherford Backscattering Spectroscopy (RBS). Preliminary results show:

- Tin oxide films are stoichiometric
- Fluorine content probably less than 0.1% (atomic)
- The tin oxide film is reduced to metallic tin at the interface with the p-layer
- Tin does not diffuse into the amorphous silicon.

4.2.1 Scanning Auger Microprobe Analysis

Samples were prepared for Auger analysis to answer the following questions:

- What is the distribution of tin at the interface between tin oxide and the p-layer?
- What amount of fluorine will diffuse from the tin oxide into the p-layer?
- What amount of fluorine will be found in a p-layer deposited from BF_3 plus silane?
- What is the chemical composition, particularly fluorine content, of tin oxide films deposited at Spire?

Four samples analyzed in detail are described in Table 4-3. Briefly, these samples were textured and non-textured tin oxide, and 10 nm p-layers doped with BF_3 or B_2H_6 deposited on undoped or doped SnO_2, respectively.

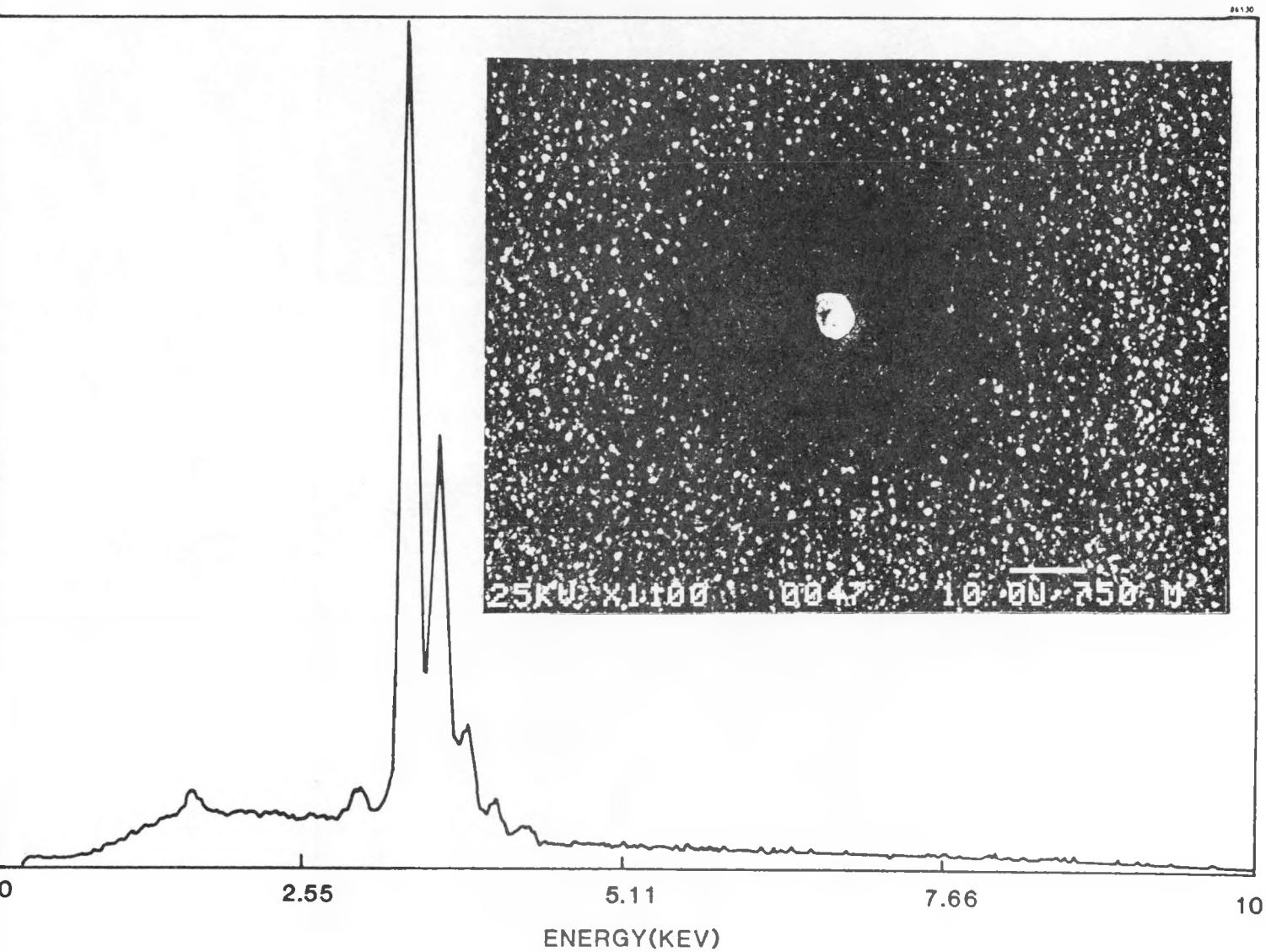

FIGURE 4-6. ANALYSIS OF DEFECT PARTICLE SHOWS TIN OXIDE COATING.

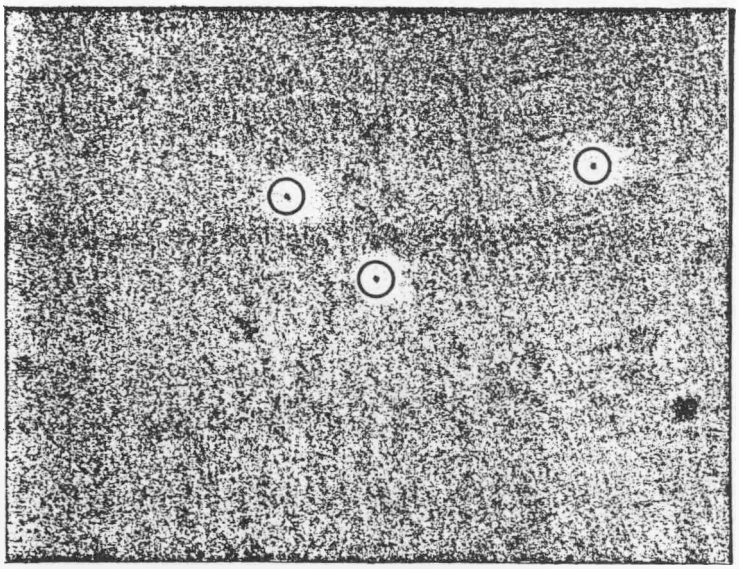

a) Spire Textured Tin Oxide.

b) Nippon Sheet Glass Specular Tin Oxide.

FIGURE 4-7. CRATER DEFECTS IN TIN OXIDE FILMS, OPTICAL PHOTOMICROGRAPHS AT 50X.

TABLE 4-3. PROCESS PARAMETERS FOR SAMPLES PREPARED FOR AUGER ANALYSIS

1. Textured tin oxide on 7059 glass, SN0072

   - First layer 800 sccm O_2, 2800 sccm N_2, 200 sccm CF_3Br, 8 sccm TMT, 16.2 cm/min speed
   - Second layer 3200 sccm O_2, 700 sccm N_2, 64 sccm CF_3Br, 8sccm TMT, 5.3 cm/min speed
   - Parameters similar to sample SN0054 in Table 4-2.

2. Specular tin oxide on silicon wafer, SN0074

   - 800 sccm O_2, 2800 sccm N_2, 200 sccm CF_3Br, 8sccm TMT, 15.6 cm/min speed
   - Parameters similar to sample SN0045 in Table 4-2
   - This was substrate used to prepare films for SIMS and RBS analyses

3. P-Layer (BF_3) on undoped tin oxide

   - Run 12201 on SN0110
   - P-Layer, 220°C, 6 minutes, 22.5 sccm SiH_4, 2.5 sccm BF_3, 0.1 watt/cm^2, 0.024 torr, about 10 nm deposited
   - Tin oxide: 900 sccm O_2, 3100 sccm N_2, 8 sccm TMT, 15 cm/min, 2 passes

4. P-Layer (B_2H_6) on fluorine-doped tin oxide

   - Run 12202 on SN0109
   - P-Layer, 220°C, 6 minutes, 20 sccm SiH_4, 5 sccm H_2 with 2% B_2H_6, 0.1 watt/cm^2, 0.022 torr, about 10 nm deposited
   - Tin oxide: Two passes under nozzle at 200 sccm O_2, 650 sccm N_2, 200 sccm CF_3Br and 8 sccm TMT at 15 cm/min. Two additional passes under nozzle at 800 sccm O_2, 2800 sccm N_2, 200 sccm CF_3Br and 8 sccm TMT at 15 cm/min.

Figures 4-8 through 4-11 show the results of Scanning Auger Microprobe Analysis. Figure 4-8 shows a scan of the surface, and a scan after sputtering with argon for 30 seconds (approximately 10 nm deep) for sample 1 in Table 4-3. Carbon contamination visible on the surface is completely absent after sputter-cleaning. There is no clear fluorine signal, implying a concentration less than 0.1 atomic percent. The nominal sensitivities to oxygen and tin were given as 0.4 and 0.9 respectively. Measuring peak-to-peak heights for tin and oxygen, with the given sensitivities, implies stoichiometric SnO_2 at the sample surface (plus contaminants) and an oxygen/tin ratio of only 1.4 after sputtering. The non-stoichiometry is caused by preferential sputtering of oxygen and is not characteristic of the film.

Figure 4-9 shows the Scanning Auger Microprobe results for a specular tin oxide film. The carbon contamination found on the surface is removed by sputtering for a short time. A fluorine peak is not identifiable in the noise; estimated maximum concentration of F is 0.1 atomic percent. Also, the ratio of oxygen to tin at the surface, 2:1, is lower after sputtering.

Figure 4-10 shows a depth profile through the 10 nm p-layer doped with BF_3 into an undoped tin oxide film. The signals do not represent accurate atomic concentration (A.C.), although the data were scaled for this, due to preferential sputtering. The tin signal has a small peak at 9 minutes, the approximate location of the start of the silicon-tin oxide interface. The oxygen signal has no corresponding peak, clearly going to zero at the interface. This is taken to be evidence of metallic tin at the interface. Because the sputtering process broadens the interface, there is no evidence for diffusion of tin away from the interface in these data. As the depth of the p-layer is approximately 20 nm, the layer of metallic tin may be just one or two monolayers. The carbon signal for this sample after sputtering through the thin surface layer is greater than that seen in Figures 4-8(b) or 4-9(b) but may still represent a background noise level, as the analyzing vacuum chamber was opened and pumped down to change samples. The fluorine signal is assumed to be zero (noise level). Boron was not detected in the film, implying a maximum concentration of 0.1 atomic percent.

Figure 4-11 shows a depth profile through a 10 nm p-layer doped with diborane (B_2H_6) deposited on top of a tin oxide film as highly doped with fluorine as possible. These data are essentially identical to those in Figure 4-10. A peak in the tin signal after sputtering 10 minutes is still visible, though smaller than in Figure 4-10. The presence and quantity of metallic tin is similar. The change in the ratio of oxygen to silicon signals is not considered significant, for the surface of this film was more textured than the previous sample, and this could affect relative sputtering rates and signals. Again, a small carbon signal was detected which could be background contamination. The fluorine signal in these data did increase above the zero background level to about 0.2 atomic percent sputtering through the silicon-tin oxide interface. Boron was not detected in the p-layer.

This Auger analysis showed glow discharge of a p-layer of amorphous silicon reduced SnO_2 to produce, approximately, one mono-layer of tin at the interface. This occurred at a sample temperature of only 220°C and low RF power (0.1 watt/cm^2) with the substrate isolated from the plasma by a grounded screen. The reduction of tin oxide occurred in a pure silane plasma with no hydrogen added and with BF_3 used as a dopant, or with B_2H_6 used as a dopant with minimum hydrogen added. The concentrations of boron and fluorine in the films were below the detection limits for Auger analysis.

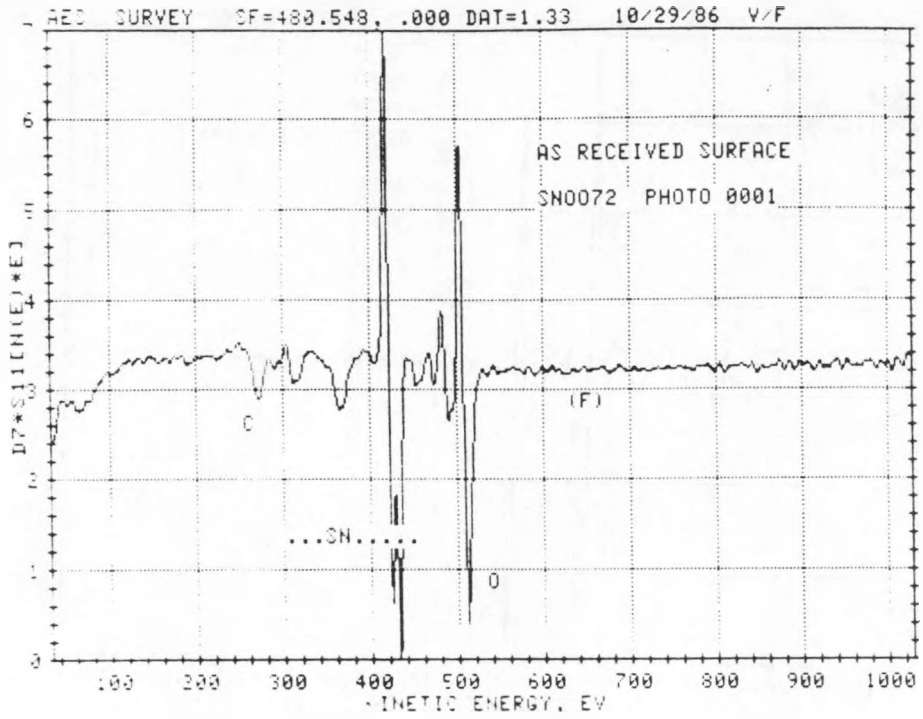

a) Surface scan position of fluorine peak, if present, indicated by (F).

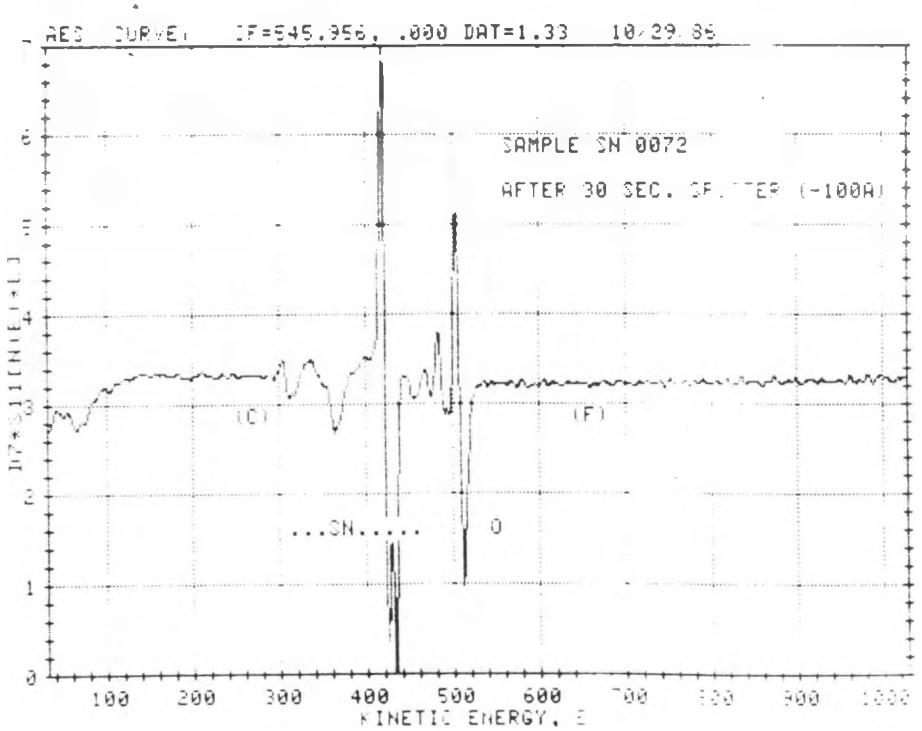

b) After sputter-cleaning surface (removing 10 nm) carbon peak (C) gone.

FIGURE 4-8. SCANNING AUGER MICROPROBE ANALYSIS OF TEXTURED TIN OXIDE.

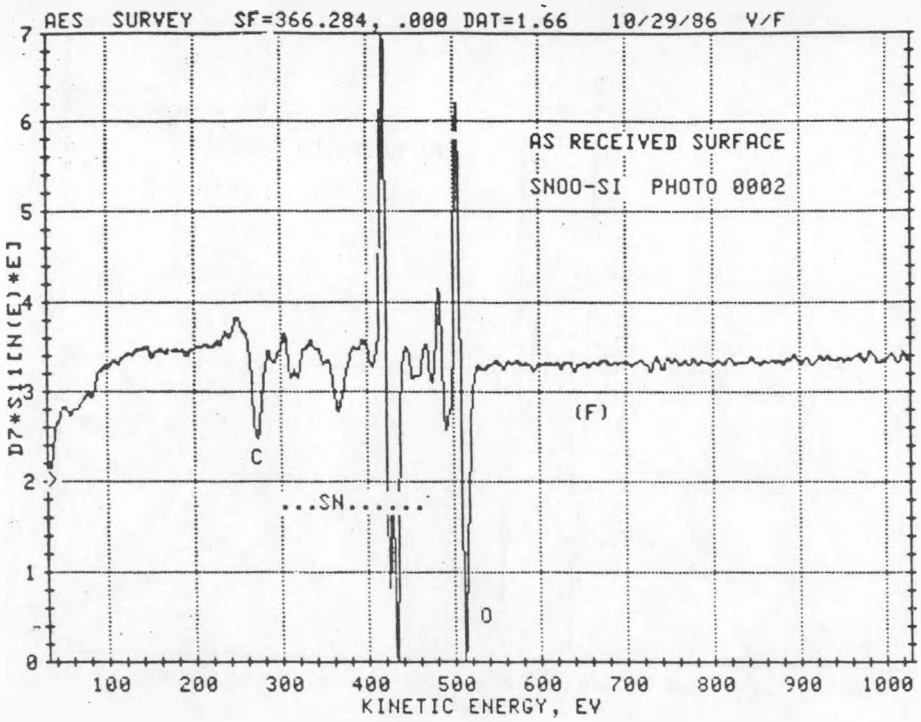

a) Surface (F) indicates position of (absent) fluorine peak.

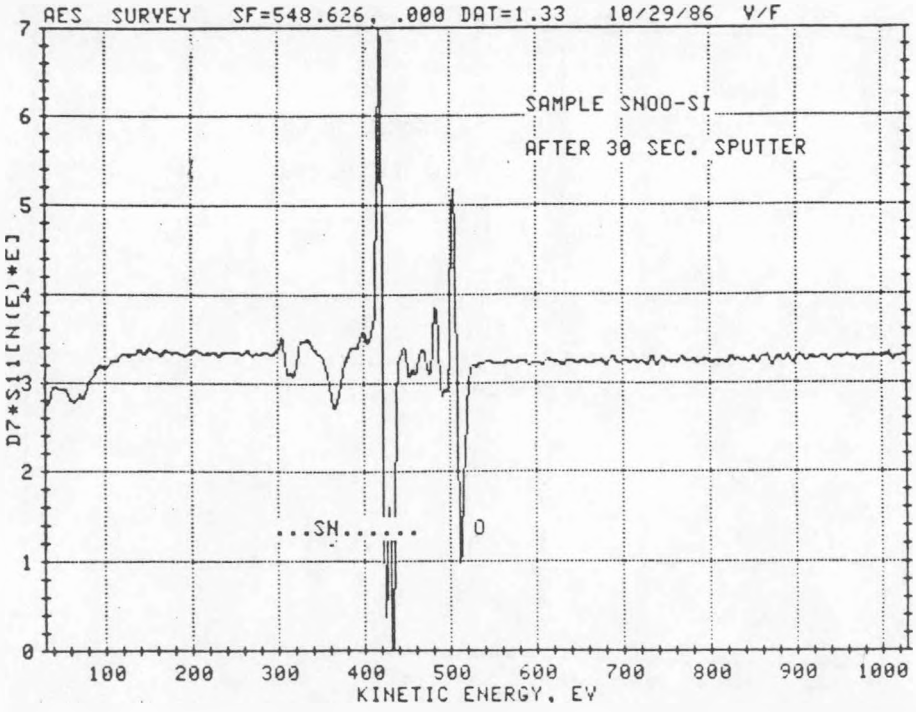

b) After sputtering approximately 10 nm.

FIGURE 4-9. SCANNING AUGER MICROPROBE ANALYSIS OF SPECULAR TIN OXIDE.

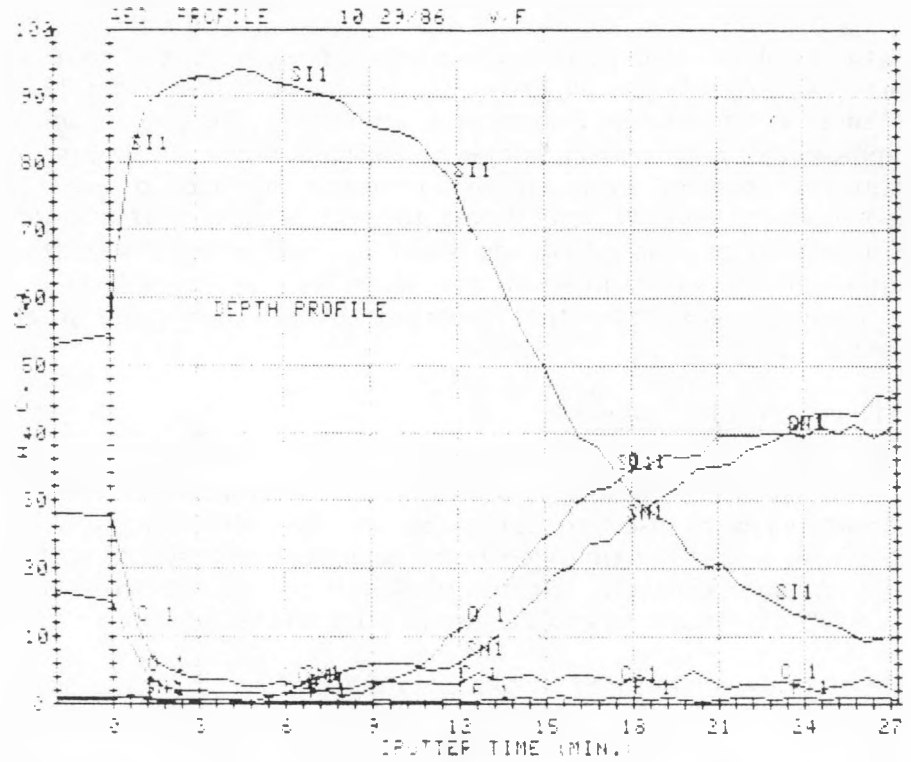

FIGURE 4-10. SAM DEPTH PROFILE OF BF_3 P-LAYER ON UNDOPED SnO_2.

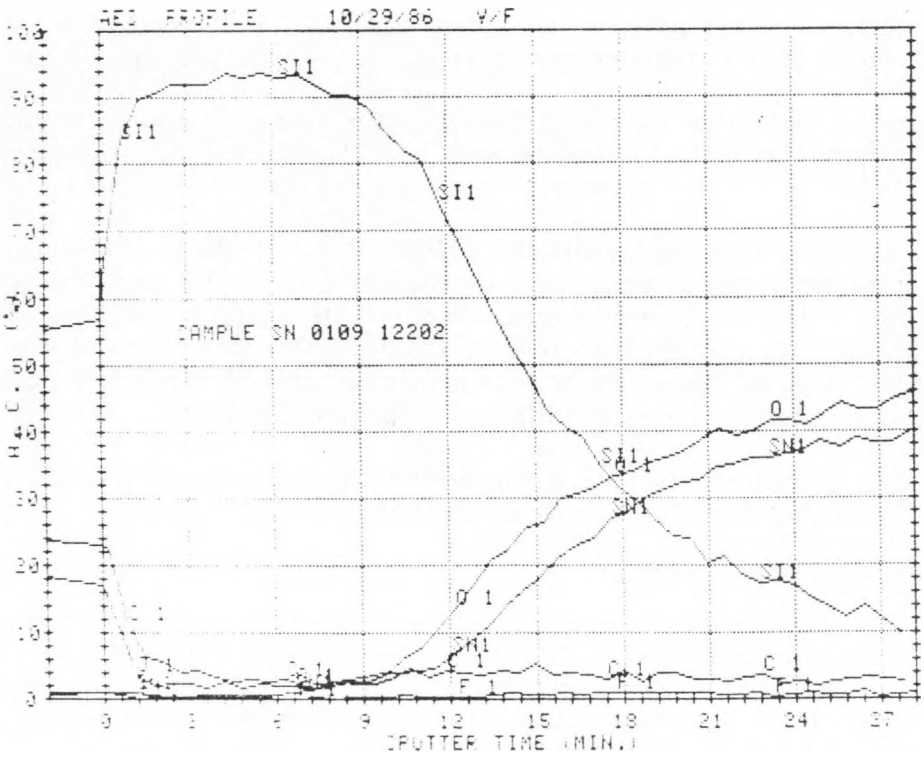

FIGURE 4-11. SAM DEPTH PROFILE OF B_2H_6 P-LAYER ON SnO_2:F.

The SAM was also used to take photomicrographs of each of the four samples. The surface of samples 3 and 4, p-layers on tin oxide, are shown in Figures 4-12 (a) and (b). A discontinuity in surface composition, such as a pinhole in the amorphous silicon layer, would be very apparent in a secondary image of emitted Auger electrons. Both pictures indicate a continuous coating, even on the textured surface, despite an estimated thickness of the p-layer of only 20 nm. It was thought that very thin amorphous silicon layers might be deposited as isolated islands which are not joined together until the film reaches some minimum thickness, in much the same way as polysilicon is deposited on SiO_2 by CVD. These images show that glow discharge amorphous silicon films are continuous.

4.2.2 SIMS Analysis of Tin Diffusion

Secondary ion mass spectroscopy (SIMS) was used as a diagnostic technique to determine if tin from the SnO_2/p-interface would diffuse into the amorphous silicon layer. High deposition temperatures were used to maximize possible diffusion. The substrate was SN0074 (see Table 4-3), a specular tin oxide layer deposited on a silicon wafer. Run 12170 deposited an i-layer, approximately 320 nm thick, on top of the tin oxide. Deposition temperature was 450°C, pressure was 0.022 torr of pure silane, run time was one hour.

The depth profile of tin was measured at two points 5 mm apart on the surface; both are shown in Figure 4-13. The tin signal of secondary ion mass spectroscopy (SIMS) was recorded as a function of time while the surface was sputtered by a high power oxygen beam. Sputtering was stopped when the tin signal dropped suddenly, implying the substrate silicon wafer was reached. The crater depth was measured and a depth scale placed on Figure 4-13 assuming a linear sputtering rate. The depth scale was not corrected for different sputtering rates of a-Si:H and SnO_2, but the end point is accurate. The maximum signal was assumed to correspond to the concentration of tin in stoichiometric tin oxide to determine the scale of the ordinate in Figure 4-13.

The results show no indication for the diffusion of tin. An increase in the tin signal near the a-Si:H/SnO_2 interfae, or bump, can be seen at 10^{17} to 10^{19} tin atoms/cc. This bump is caused by small irregularities in the surface (Figure 4-5a).

The tin signal at the sample surface is the effect of a pinhole in the amorphous silicon layer. This signal degrades to zero, i.e., the beam sputters through the underlying tin oxide in the pinhole, before the amorphous silicon-tin interface is reached. The tin signal at maximum depth drops from 90% to 10% in about 30 nm; this is the best resolution for this technique with this sample at an infinitely sharp interface because the original silicon wafer was highly polished and the crystalline silicon-tin oxide interface is very abrupt.

In optimizing this experiment to detect tin, detection of oxygen or flourine in either the amorphous silicon or tin oxide layers was precluded.

4.2.3 RBS Analysis of Tin Diffusion

Rutherford Backscattering Spectroscopy (RBS) was used as a complementary analytical technique to SIMS. Although this technique is less sensitive to small concentrations of contaminants, it does not distort depth profiles by sputtering and it does not need a "standard" for determining atomic concentrations. The technique measures the energy of alpha particles reflected from the sample, and the original datum is count rate at a given

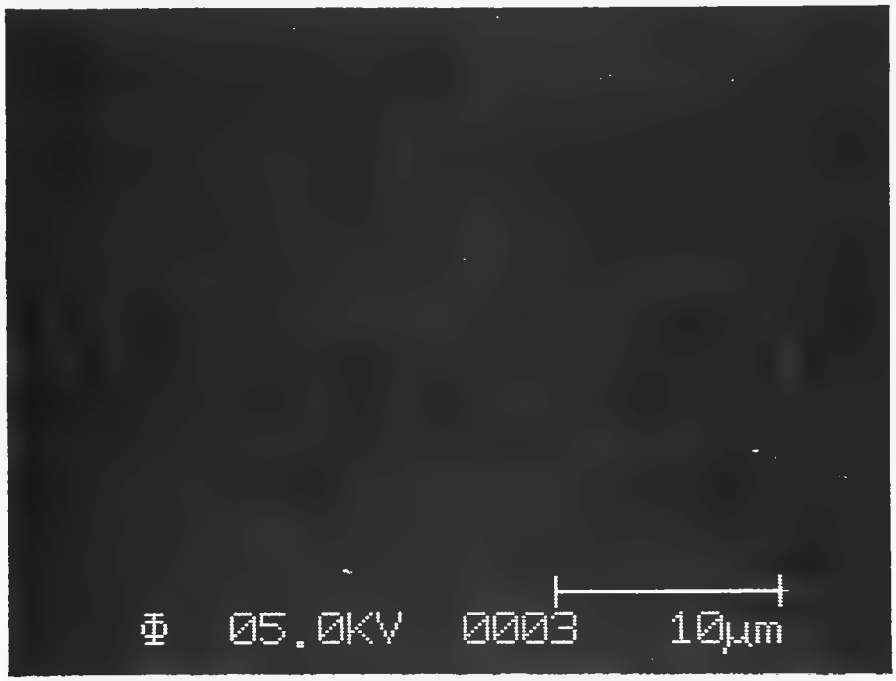

(a) BF_3 P-Layer on Undoped SnO_2.

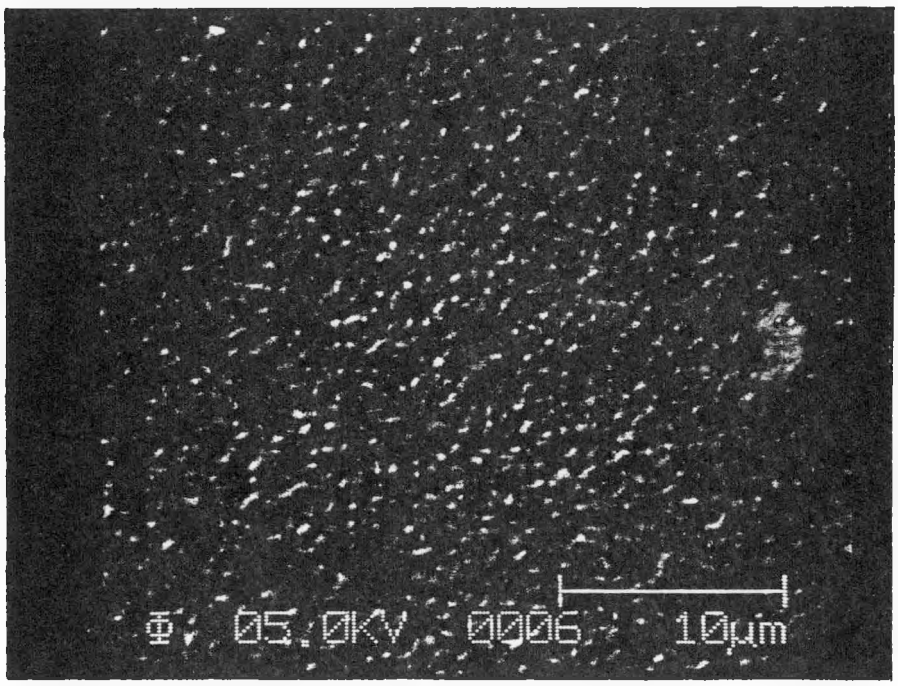

(b) B_2H_6 P-Layer on Doped SnO_2 (textured).

FIGURE 4-12. SAM IMAGE OF SURFACE OF P-LAYERS SHOWING CONTINUITY OF 200 nm FILMS (3000X).

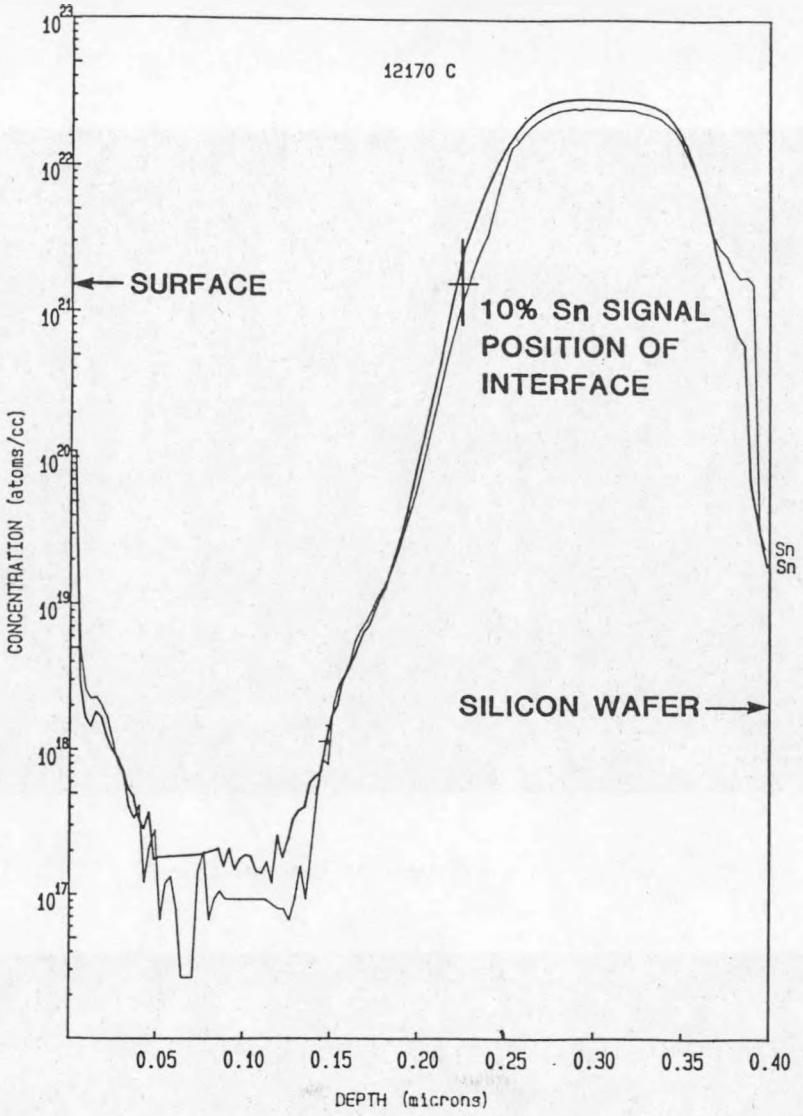

FIGURE 4-13. SIMS ANALYSIS OF I-LAYER ON SnO_2 AT 450°C.

energy, Figure 4-14. The energy of the reflected alpha particle is greater for collisions with atomic nucleii of high mass and is reduced proportional to depth for reflection from buried atoms.

The sample used in this analysis is identical to that used for SIMS, an amorphous silicon film deposited on top of a tin oxide film on a silicon wafer. Tin oxide films on glass could not be used because high mass components in the glass (barium) would add substantial noise to the analysis. The only high mass atom in the sample is tin, so the signal is at much higher energy than the surface of the amorphous silicon layer, and this significantly improves resolution to determine if any tin has diffused forward.

Figure 4-14 shows the raw data from RBS analysis with a theoretical curve fit added. The silicon signal on the left shows the surface layer (channel 300) followed by a dip representing the location of the tin oxide layer followed by the signal from the substrate, with increasing depth represented by lower energy or channel number. The tin signal is the large peak on the right, and the oxygen signal is the "bump" on the silicon curve at about channel 150.

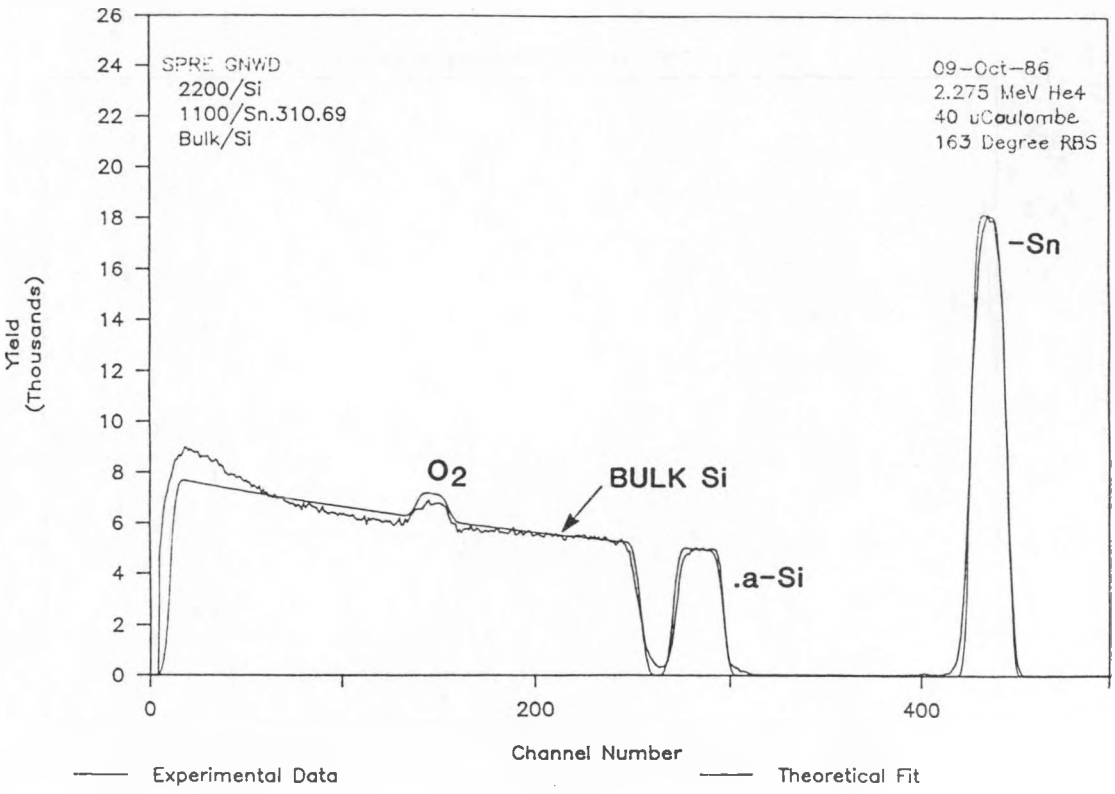

FIGURE 4-14. RBS ANALYSIS OF A-Si:H ON SnO_2 ON SILICON WAFER.

Figure 4-15 is the analyzed RBS composition versus depth profile. We believe that the density of crystalline silicon instead of amorphous hydrogenated silicon was used in computing the depth of the first layer, which should be thicker than shown. The thickness of the tin oxide layer is correct. Hydrogen is not seen in this analysis. The ratio of oxygen to tin (69% to 31%) is within experimental accuracy of stoichiometric composition. The Auger-determined ratios of oxygen to tin is wrong. No diffusion of tin could be detected from this data.

4.2.4 STABLE a-Si:H-METAL BACK CONTACT INTERFACES

Direct evaporation of silver onto phosphorus doped amorphous silicon alloy films as a back contact produced an excessive number of shorted cells in experiments at Spire. Functional cells suffered rapid degradation. Therefore, an optically transparent conductive interlayer which would serve as a diffusion barrier to Ag was developed.

For high efficiency cells, a layer of titanium 2.5 nm thick is evaporated through a mask at room temperature. The film is exposed to air when the evaporation boat is changed, and then 500 nm of silver is evaporated through the same mask.

Figure 4-16 shows the optical transmission through the titanium film compared to the transmission through the glass substrate alone. The film absorbs less than 2% of all light with wavelengths longer than 500 nm. The film is believed to be non-stoichiometric titanium dioxide. Its impact on optical and electrical device properties is discussed in 5.2.7.

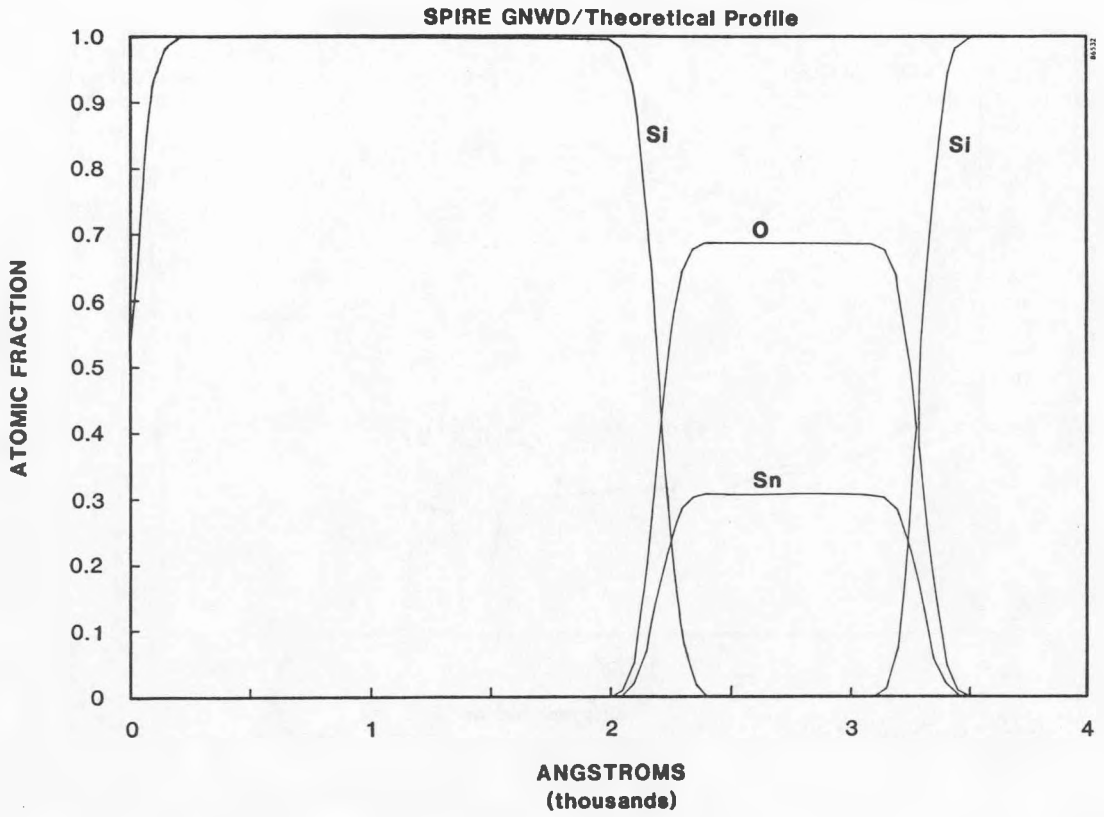

FIGURE 4-15. DEPTH PROFILE OF a-Si:H/SnO_2/Si SAMPLE BY RBS ANALYSIS.

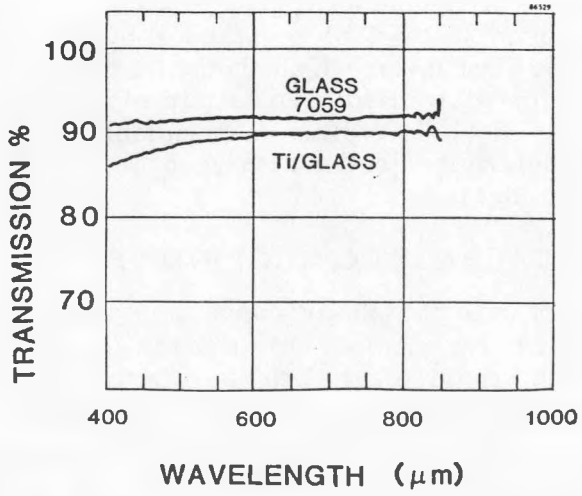

FIGURE 4-16. OPTICAL TRANSMISSION OF THIN TITANIUM OXIDE (Ti_xO_y)FILMS.

SECTION 5

SINGLE-JUNCTION CELL RESEARCH

5.1 SINGLE-JUNCTION CELL DEVELOPMENT

Earlier in this program, efficiencies of 9.1% over 0.1 cm^2 area have been achieved by this laboratory for single-junction a-Si:H cells, with typical J_{sc} in the 14-15 mA/cm^2 range.[3] Also, a(Si,Ge):H cells with a graded bandgap i-layer having over 7% efficiency were fabricated by changing the (Ge)/(Si) ratio during growth, with a maximum ratio of about 40% near the n^+-layer, suggesting a minimum bandgap of 1.5 eV.[5]

The two major problems to be solved in the quest for single-junction devices adequate for the development of high efficiency tandem cells are described below:

First, a substantial decrease in efficiency with increasing device area has previously limited the highest efficiencies reported by this laboratory to 0.1 cm^2 area devices. Many factors, such as SnO_2 morphology, substrate cleaning procedures, available clean-room technology and dust formation in the plasma determine the surface concentration of defects in an a-Si:H sample. Analysis of our specific problem, however, pointed to the last-mentioned as the dominant factor in the creation of shunting defects limiting both the efficiency and yield of our samples.

Second, the J_{sc} of the graded bandgap a-(Si,Ge):H cell has been limited to 15-16 mA/cm^2, possibly as a result of the decrease in carrier generation due to the higher bandgap existing throughout most of the i-layer, as compared to the ungraded case. Modeling of tandem I-V characteristics using an estimate of tandem J_{sc} from measured single-junction cell quantum efficiency data shows that when a-Si:H devices of about 9% efficiency are joined to a-(Si,Ge):H cells of this type, tandem efficiencies are limited by the J_{sc} of the low bandgap cell to about 9% (Appendix C).

The key aspects of the development effort during this last phase center on the solution to the above problems. First, low pressure (below 100 mTorr) deposition of all a-Si:H alloys has been used to avoid dust formation, reducing film pinhole density. Second, all alloy deposition processes have been adapted to low-pressure deposition, with specific emphasis on a-(Si,Ge):H of bandgap $E_g < 1.5$ eV.

In summary, the key activities during this period of six months were directed to:

1. The reproducible achievement of high efficiencies in single- and multi-junction devices of 1 cm^2 area.

2. The development of high quality a-(Si,Ge):H alloy i-layers with bandgap $E_g < 1.5$ eV.

This effort will be described in what follows.

5.2 a-Si:H SINGLE-JUNCTION CELLS

As the last phase of our program was approached, it was considered essential that the ability to obtain a-Si:H devices of high quality be demonstrated. This is because p^+ and n^+ layer technology as well as contact technology utilizing SnO_2 as the front contact and Al or Ti/Ag as a back contact developed during this program for a-Si:H could be used in p-i-n devices as an approach to a-(Si,Ge):H and tandem cell optimization.

As will be seen in what follows, a-Si:H devices with efficiencies over 10% were obtained through this effort. This suggests that the quality of our device fabrication techniques is excellent. While the specific improvements introduced in this period will be analyzed separately, an update and summary of the fabrication techniques utilized is appropriate at this point.

5.2.1 Summary of a-Si:H Device Fabrication in Multi-Sector Reactor

Standard single- and multi-junction cells were fabricated for this program on a 10 cm x 10 cm glass substrate, which is covered by a 1,500 to 2,500 nm thick SnO_2 layer acting as the front contact. For high efficiency cell fabrication, textured SnO_2:F with 5 to 10% absorptance and 5 to 15 $\Omega/\square$ sheet resistance grown by chemical vapor deposition in our laboratory (see Section 4) was used. For experiments where high efficiency was not essential, commercially obtained specular SnO_2 was used. This material has typically high absorptance (>15%) and sheet resistance of less than 20 $\Omega/\square$. A SnO_2 of quality comparable to that grown in our laboratory was not commercially available.

The standard p-i-n structure utilized for single-junction devices consists of:

1. A 10-15 nm thick, highly conductive and transparent a-(Si,C):H:B p^+-layer.

2. A thin (ca. 10 nm), sharply graded a-(Si,C):H transition layer in which the C concentration decreases to zero from that in the p^+-layer.

3. An a-Si:H i-layer with thickness in the range 150-700 nm.

4. A high conductivity a-Si:H n^+-layer.

The substrate is mounted on the central rotating drum in our multi-sector reactor and moved from one sector to another. Cross-contamination is avoided by growing a thin (ca. 50 nm) intrinsic a-Si:H layer (plasma cleaning) in the appropriate sectors following p^+, n^+ and transition layer deposition.

The basic sequence of operations in the preparation of an a-Si:H cell is shown in Table 5-1. This sequence was established during the last quarter of program activity and some of the details of this development will be discussed in the following paragraphs.

As a back contact, aluminum single layers or a bi-layer composed of a thin (<5 nm) layer of titanium followed by a highly reflecting layer of silver are deposited through a contact mask. Two mask patterns were used, one defining device areas of 0.1 and 0.5 cm^2 and the other containing additional devices with 1.0 cm^2 area, as shown in Figure 5-1.

TABLE 5-1. SEQUENCE OF DEPOSITION FOR A P-I-N a-Si:H CELL

	Operation	Sector
1.	Plasma Cleaning	p^+
2.	p^+-Layer	p^+
3.	Plasma Cleaning	p^+
4.	Plasma Cleaning	n^+
5.	Plasma Cleaning	i
6.	Transition Layer	i
7.	i-layer	i
8.	n^+-layer	n^+
9.	Cool in SiH_4 flow	n^+

To provide a coplanar contact to the front electrode, the a-Si:H layer is removed by mechanical scribing along lines approximately 100 μm wide, about 1 mm away from the contact edge. Bus collectors are evaporated through the same mask, contacting the a-Si:H through the exposed scribe line and having edges about 1 mm away from the back contact, as shown in Figure 5-2. Aluminum contacts are occasionally applied to the SnO_2 before a-Si:H deposition, to increase redundancy.

5.2.2 Interface Studies for Single-Junction p-i-n Cells

The desired properties for a p^+-layer are high conductivity and transparency. Data on device V_{oc} and J_{sc} can be used as a measure of p^+-layer quality. However, V_{oc} and fill factor can also be affected by the transition layer between the p^+ and i-layers.[11] Thus, p^+ and transition layer optimization cannot be easily separated.

It is clear from qualitative considerations that an optimum thickness exists for the transition layer. A thin i^+-layer would not prevent electrons from backstreaming to the p^+/i- interface while a thick layer may introduce excessive series resistance losses or decrease the high electric field near the interface, thus decreasing FF.

We have developed a deposition process for the p^+ and transition layers that leads to the formation of an optimum p^+/i-interface and therefore to simultaneously high V_{oc} and FF. Deposition parameters yielding devices with high V_{oc} and FF under low pressure plasma conditions were obtained by varying the input RF power W_{rf} and the deposition time t for the p^+-layer and transition layer i_t. Data for devices prepared under various sets of conditions are shown in Table 5-2. Samples were prepared using specular, commercially obtained SnO_2, aluminum back contacts and a plasma cleaning sequence more extensive than the one shown in Table 5-1 (see 5.2.3).

The average values for the V_{oc}, J_{sc}, FF and efficiency of all 0.1 cm^2 cells in each substrate with $R_{sh} \geq 500$ cm^2 are given. Typical variations over the substrate were: $\Delta V_{oc}/V_{oc} \leq 2\%$, $\Delta J_{sc}/J_{sc} \leq 1\%$ and $\Delta FF/FF \leq 10\%$. The quantum efficiency ratio R = QE (-1V)/QE(0V) for the highest efficiency cell in each sample is also shown.

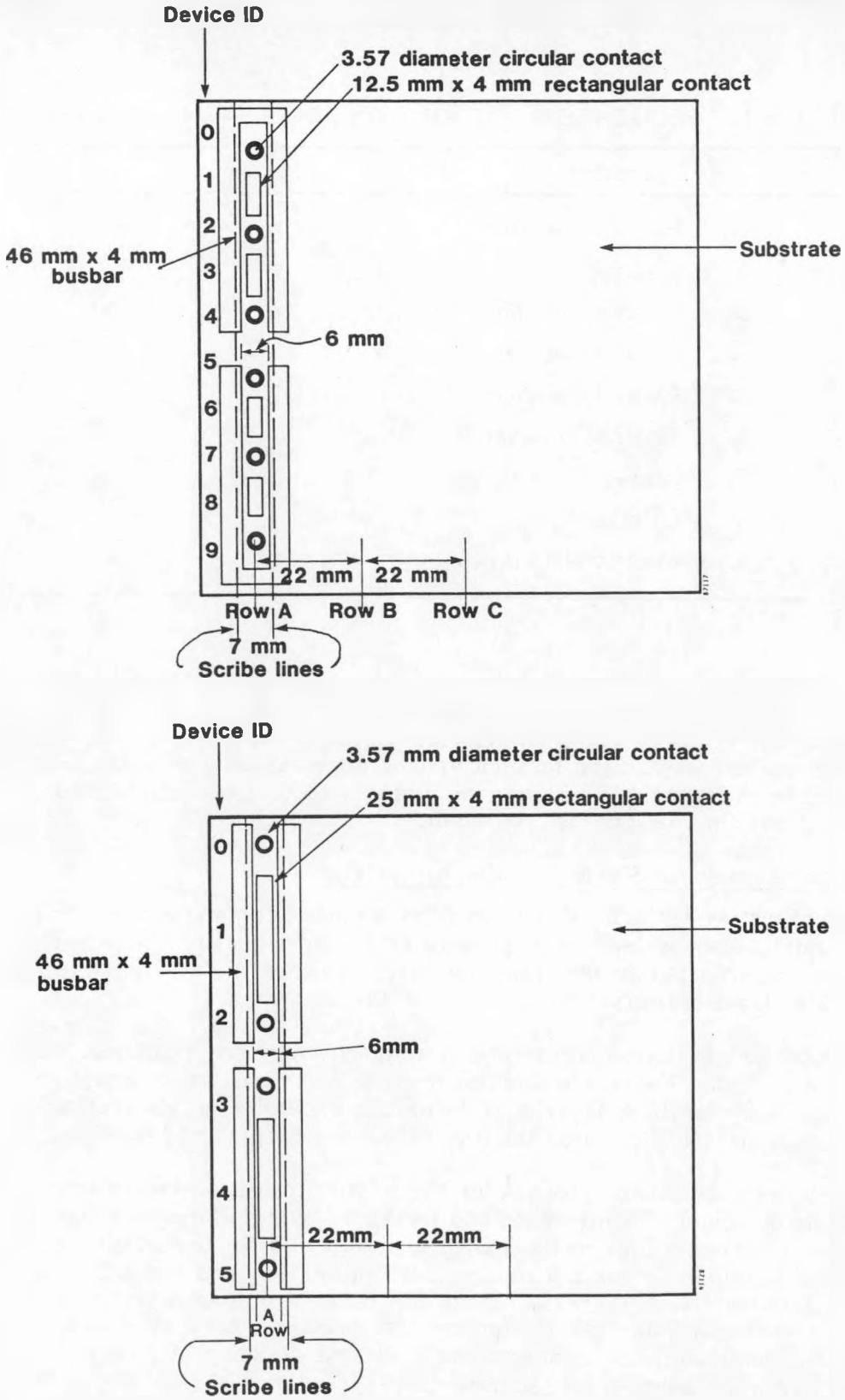

FIGURE 5-1. MASK PATTERNS FOR METAL CONTACT DEPOSITION INCLUDING (a) 0.1 cm^2 AND 0.5 cm^2 and (b) 0.1 cm^2 and 1.0 cm^2 devices. Rows W and X are added between A, B and C when more devices are desired. When masks in (a) and (b) are used simultaneously on the same substrate, other letters are used for row identification.

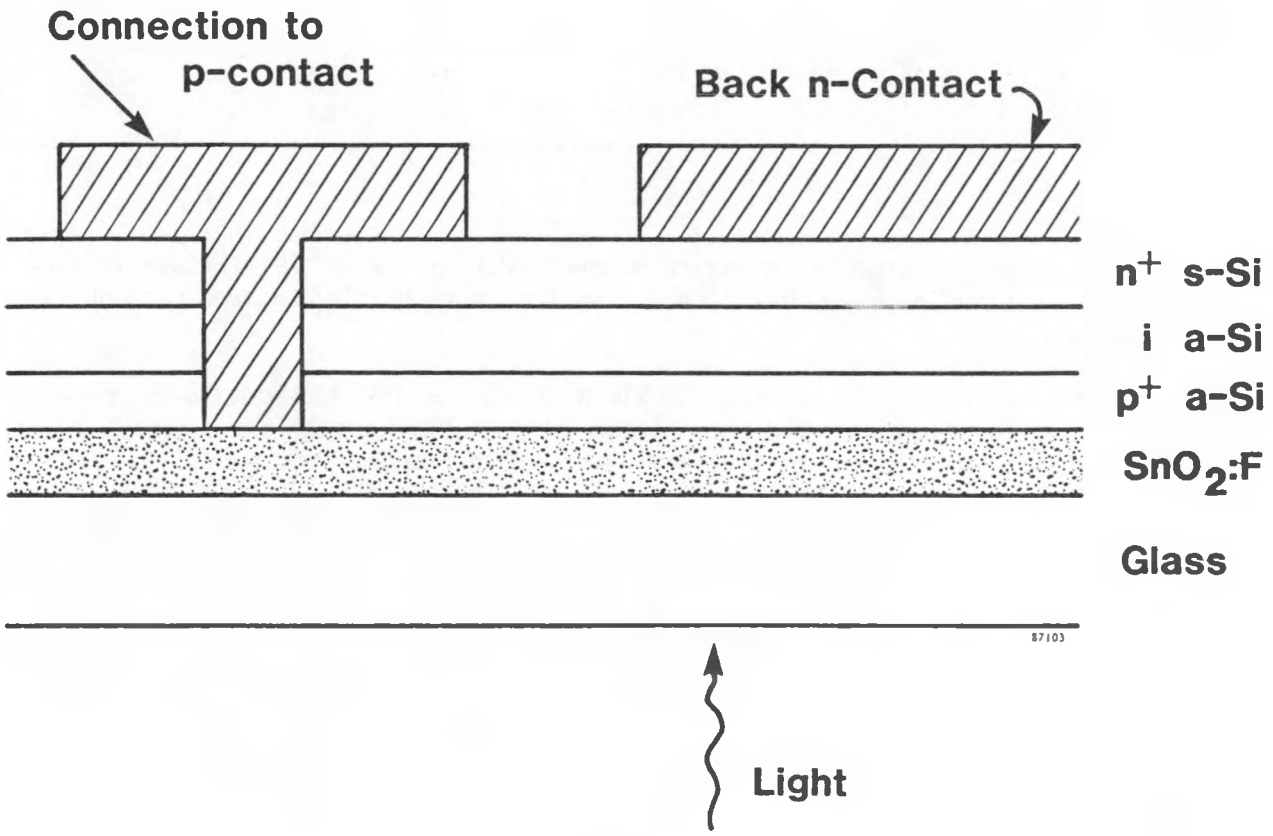

FIGURE 5-2. CROSS SECTION OF p-i-n a-Si:H ALLOY DEVICE SHOWING CONTACT GEOMETRY.

TABLE 5-2. AVERAGE i-V CHARACTERISTICS OF 0.1 cm^2 DEVICES FOR VARIOUS DEPOSITION CONDITIONS. $T(p^+)$ = 210°C, $T(i_t)$ = 300°C, T(i) = 275°C, $T(n^+)$ = 325 °C, $t(n^+)$ = 20 min.

Sample	$W_{rf}(p^+)$ (mW/cm^2)	$t(p^+)$ (s)	$W_{rf}(i_t)$ (mW/cm^2)	$t(i_t)$ (s)	th(i) (nm)	V_{oc} (mV)	J_{sc} mA/cm^2	FF (%)	EFF (%)	R (-)
20442(HP)	0.13	190	0	0	620	816	12.9	60.0	6.3	1.18
20448(LP)	0.08	300	0.07	360	610	763	12.5	72.0	6.9	1.03
20458(LP)	0.12	240	0.12	300	610	818	12.2	70.3	7.0	1.07
20457(L)	0.18	200	0.18	240	610	843	11.9	67.8	6.8	1.10
20463(L)	0.18	150	0.18	180	610	843	12.6	66.2	7.1	1.01
20467(LP)	0.18	150	0.18	180	600	844	12.8	69.3	7.5	1.04

The quantum efficiency ratio is a measure of the quality of the p^+/i-interface region. A ratio greater than one in the region < 550 nm indicates negligible electron recombination in this region.

The deposition conditions for sample 20463, with $t(i_t)$ = 180 s, seem to be optimum. Figure 5-3 shows the quantum efficiency of cell 20463-B9 under both short-circuit and I-V reverse bias conditions, confirming the high quality of this device structure.

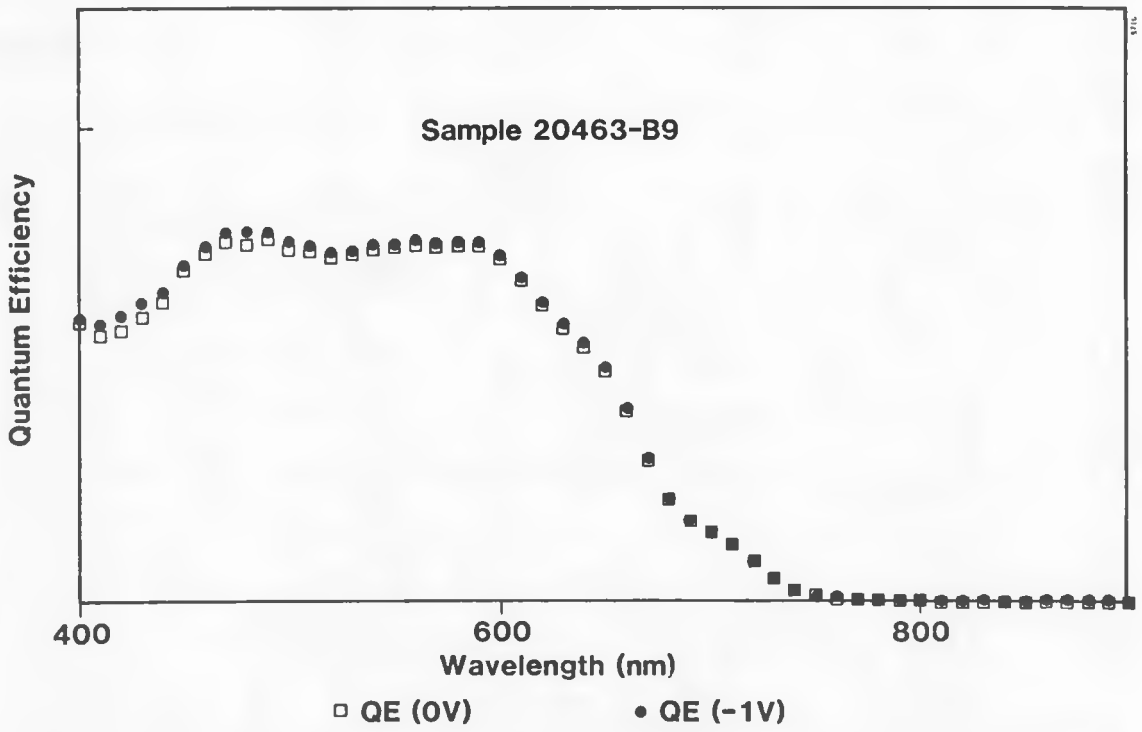

FIGURE 5-3. QUANTUM EFFICIENCY OF SAMPLE 20463-B9.

Finally, the reproducibility of the low-pressure process can be assessed by comparing the close I-V characteristics of samples 20463 and 20467, prepared under identical conditions. This result is typical of the control achieved. The standard process parameters developed from the effort described in 5.2.1 and this paragraph are as listed in Tables 3-1, 3-2 and 3-3.

5.2.3 Cross Contamination in Multi-Sector Reactor

During the initial phases of our program the plasma cleaning step was executed in all six sectors of the reactor both before and after p^+-layer deposition. This was true of all the samples in Table 5-2 and was a source of unnecessary delay in sample deposition, adding more than two hours to the total deposition time.

In order to assess the effect of the plasma cleaning routine, sample 20477 was grown using the same process described in Table 5-2, but with the routine shown in Table 5-1. The average of the I-V characteristics of all 0.1 cm^2 area devices is shown in Table 5-3 for samples 20463, typical of the process described in Table 5-2 and 20477. The ratios R = QE(-1V)/QE(0V) of the quantum efficiency (QE) in reverse bias to the QE at zero bias at 450 nm and 650 nm, respectively measuring the quality of the p^+i interface and the i-layer bulk, are also given in Table 5-3 for the best device in each sample.

TABLE 5-3. AVERAGE i-V CHARACTERISTICS OF a-Si:H SAMPLES GROWN WITH SHORT (SPC) AND LONG (LPC) PLASMA CLEANING ROUTINE.

Sample	Type	V_{OC} (mV)	J_{SC} (mA/cm^2)	FF (%)	EFF (%)	R(450 nm) (-)	R(650 nm) (-)
20463	SPC	844	12.6	66.2	7.1	1.01	1.02
20477	LPC	874	12.6	67.4	7.5	1.03	1.02

The variation observed between samples 20463 and 20477 is not considered to be significant. Based on the above data, the plasma cleaning routine in Table 5-1 was instituted. It is believed that the time necessary for plasma cleaning can be further reduced without affecting device quality.

As will be explained below, an extra plasma cleaning step after transition layer deposition was introduced in an effort to prevent carbon contamination and improve i-layer quality for the fabrication of high efficiency a-Si:H cells. This, however, affected the sequence in Table 5-1 only for the last ten a-Si:H samples fabricated for this program.

5.2.4 Photon Economy of a-Si:H Devices

Effect of i-layer Thickness

The photon economy of a-Si:H samples such as those fabricated during the optimization process described above can be easily understood with the help of an optical model of the device as a stack of homogeneous layers with plane, parallel boundaries. The optical constants and thicknesses of the layers are assumed to be known. If it is further assumed that no carrier recombination takes place in the cell i-layer, and that all carriers generated in the p^+ and n^+-layers recombine, then:

$$J_{sc}(NR) = e \int A_i(\lambda)\,\pi(\lambda)\,d\lambda$$

where $J_{sc}(NR)$ is the J_{sc} in the no-recombination limit, e the electron charge, λ the wavelength, A_i the absorbtance of the i-layer and $\pi(\lambda)$ the photon flux. Clearly, we can also state that:

$$L_K = e \int A_K(\lambda)\,\pi(\lambda)\,d\lambda$$

where A_k and L_k are the absorptance of layer k and the corresponding photon loss expressed as a light-generated current loss.

The no-recombination assumption is valid provided that the thickness of the i-layer does not exceed the field-enhanced diffusion length of the shortest-lived carrier, usually holes. This model is strictly applicable only to untextured devices.

From the extensive literature available[12,13] we have chosen values of the optical constants of a-Si:H, representing a material with a bandgap E_g 1.80 eV, as well as optical values for aluminum and silver. Values for the available SnO_2 layers have been calculated from measured optical spectra. Using these values, a computer calculation with the model yields the loss values in Table 5-4.

TABLE 5-4. CALCULATED PHOTON LOSSES FOR A P-I-N a-Si:H CELL

Layer	Thickness (nm)	L_K (mA/cm^2)	J(NR) mA/cm^2
Glass	-	0.20	
SnO_2	500	3.51	
p^+	150	0.87	
i	600	-	12.06
n^+	300	0.15	
Aluminum	500	2.22	
TOTAL INTERNAL LOSS:		6.95	

Since the total light-generated current available in the AM1.5 spectrum up to a wavelength of 800 nm is J_T = 26.98 mA/cm^2, we can complete the description of the photon economy of this typical device as follows:

TOTAL INTERNAL LOSS:	ΣL_K =	6.95 mA/cm^2
LIGHT-GENERATED CURRENT:	J(NR) =	12.06 mA/cm^2
TOTAL ABSORBED:	J_A =	19.01 mA/cm^2

REFLECTION LOSS = $J_T - J_A$ = (26.98 -19.01) mA/cm^2 = 7.97 mA/cm^2

The values calculated above are representative of a typical a-Si:H device as fabricated in the effort described in 5.2.2 and 5.2.3. The calculated values of J_{sc} are in agreement with those experimentally observed.

Even though the device efficiencies obtained did not approach 8%, the major problem, low J_{sc}, is easily understood based on this model. The results suggest that, in this type of device, the major losses are absorption in the SnO_2 and in the aluminum back contact and total reflection, and that the i-layer quality is adequate. This points to the use of textured, highly transparent SnO_2 and highly reflecting Ti/Ag bi-layer contacts as the most fruitful approach to high efficiency a-Si:H cells.

5.2.5 I-layer Thickness Effects in a-Si:H p-i-n Cells

If the model in 5.2.4 is used in the design of tandem structures (Section 6), the results suggest that the design thickness for the i-layer of the high bandgap a-Si:H cell in a two-terminal tandem should be less than the typical value of 600 nm used in the initial optimization of the low-pressure deposition process. In fact, thicknesses of less than 200 nm can yield a light-generated current of over 10 mA/cm^2, sufficient to exceed 10% tandem cell efficiency, (see Section 6). As the i-layer thickness t(i) decreases below 200 nm, the resulting decrease in bulk recombination in the i-layer should cause V_{oc} and FF to increase and approach the practical limits imposed by p^+, i_t and n^+-layer quality and contact technology. Thus, both FF and V_{oc} of an a-Si:H p-i-n device of a design appropriate for a tandem cell could well exceed the values obtained in thicker devices.

In order to determine what i-layer thickness would yield the design values of J_{sc} needed for application in a tandem and what values of FF and V_{oc} are achievable using the deposition techniques previously developed, we investigated the change in a-Si:H p-i-n cell performance with the thickness of the i-layer.

Table 5-5 shows the average values for the V_{oc}, J_{sc}, FF and efficiency of 0.1 cm^2 cells in each substrate with $R_{sh} \geq 500$ (Ω/cm^2) for a series of a-Si:H samples with i-layers of variable thickness th(i). Both p^+ and i_t layer deposition conditions are as in 5.1.2, the samples are listed in order of decreasing i-layer thickness and the n^+, p^+ and i-layer deposition times are indicated by $t(n^+)$, $t(p^+)$ and t(i) respectively.

TABLE 5-5. AVERAGE I-V CHARACTERISTICS OF a-Si:H CELLS WITH VARYING i-LAYER THICKNESS. Cell area is 0.1 cm^2, $R_{sh} \gtrsim 500$ cm^2, T (n^+) = 325°C.

Sample	$t(n^+)$ (min)	$t(p^+)$ (s)	t(i) (min)	th(i) (nm)	V_{oc} (mV)	J_{sc} (mA/cm^2)	FF (%)	Eff (%)
20467	20	150	150	600	844	12.8	69.3	7.5
20563	10	180	75	310	882	11.1	71.2	7.0
20543	10	180	75	290	834	11.2	70.5	6.6
20486	20	150	35	190	868	9.3	74.2	6.0
20553	10	180	35	190	883	9.7	72.1	6.2
20554	10	180	35	180	897	9.4	70.8	6.0
20560	10	180	35	180	875	9.4	74.2	6.1
20562	10	210	35	170	882	9.3	72.7	6.0

As expected, J_{SC} decreases as the i-layer becomes thinner, with the J_{SC} values obtained in good agreement with the values calculated from the optical model. Cells with 180 nm thick i-layers yield values near 10 mA/cm^2, suggesting that such values could be easily exceeded with the use of textured SnO_2.

The predicted increase in FF and V_{OC} is indeed observed when t(i) is changed from 600 to 310 nm, but there appears to be some variability in film quality from sample to sample, and both V_{OC} and FF reflect this. Finally, note that the average growth rate seems to decrease with sample thickness.

Clearly, variations in $t(p^+)$ from 150 to 210 s do not have a significant effect on V_{OC}. It is worth noting that values of V_{OC} as high as 926 mV and FF in excess of 75% have been obtained in cells with i-layers ca. 180 nm thick. Table 5-6 shows the I-V characteristics of selected devices exhibiting high V_{OC} and FF.

TABLE 5-6. I-V CHARACTERISTICS OF a-Si:H DEVICES WITH HIGH V_{OC} and FF, FABRICATED ON UNTEXTURED SnO_2 WITH ALUMINUM BACK CONTACTS. Device area is 0.1 cm^2.

Sample	$t(p^+)$ (s)	t(i) (min)	V_{OC} (mV)	J_{SC} mA/cm^2	FF (%)	EFF (%)	Comment
20511-C0	150	120	926	11.8	64.6	7.0	High V_{OC}
20516-C2	150	35	883	8.1	77.5	5.6	High FF
20554-B2	180	35	910	9.5	70.5	6.1	High V_{OC}
20555-B0	160	35	901	9.7	74.7	6.5	High V_{OC}, FF

We conclude from these data that very high values of V_{OC} and FF are attainable in a-Si:H p-i-n devices appropriate for use as the top cell in a two-terminal tandem structure. We also conclude that the deposition technology developed during this initial effort is adequate for the fabrication of high efficiency a-Si:H p-i-n devices. Indeed, as reported below, efficiencies in excess of 10% have been achieved based on essentially this technology with the addition of assorted techniques, based on photon accounting, directed to maximizing J_{SC}.

5.2.6 Stability Studies for Single-Junction Cells

The impact of the Stabler-Wronski effect on single-junction and tandem-junction device characteristics was studied in the early phases of this program using I-V and quantum efficiency measurements.[3] It was concluded that in both cases, decreases in the electron and hole ($\mu\tau$) products due to the creation of mid-gap defects upon light exposure was the major factor in device degradation. In what follows, we report the results of further stability testing. Several a-Si:H p-i-n cells of the type described in 5.2.2 and 5.2.5 were exposed to AM1.5 illumination for up to four hours. While this time interval was not sufficient to achieve the stable, degraded state, the measured changes in I-V characteristics are qualitatively the same as those seen for longer stress times. Table 5-7 shows the I-V characteristics before and after exposure to AM1.5 illumination for four hours for two cells of different i-layer thickness. The changes in ratio R = QE(-1V)/QE(0V) at 450 nm are also shown. No major changes were detected in the corresponding ratio at wavelengths over 600 nm.

TABLE 5-7. I-V CHARACTERISTICS OF a-Si:H CELLS BEFORE AND AFTER EXPOSURE TO AM1.5 ILLUMINATION FOR FOUR HOURS.

Sample	I-layer Thickness (nm)	Exposure Time (hours)	V_{oc} (mV)	J_{sc} (mA/cm^2)	FF (%)	Eff (%)	R(450 nm) (-)
20467-C9	600	0	827	12.6	66.8	6.9	1.02
		4	823	12.3	58.7	5.9	1.10
20516-C2	180	0	904	8.3	75.8	5.7	1.00
		4	887	8.2	72.6	5.3	1.03

From the data, we conclude that 1) cells degrade as first described by Staebler and Wronski, 2) thin (180 nm) cells degrade less than thick (600 nm) cells and 3) defects created near the p-i interface, as evidenced from the change in R (450 m), impact cell performance the most by causing a FF decrease. Cells of recent date show less degradation than previous cells, particularly in their long wavelength response.

5.2.7 High-Reflectance Titanium-Silver Back Contacts

A process for applying back contacts to a-Si:H alloy devices was refined during the final period. In this process (see Section 4), a thin, highly transparent layer of what is possibly a non-stoichiometric titanium oxide is covered by a 500 nm silver layer to yield a high reflectance back contact. The increase in reflectance over aluminum is translated into a higher light-generated current.

The quantum efficiency of adjacent aluminum and Ti/Ag back contact cells, fabricated on the same sample, is shown in Figure 5-4. The quantum efficiency is essentially identical up to 550 nm but deviates strongly beyond this wavelength.

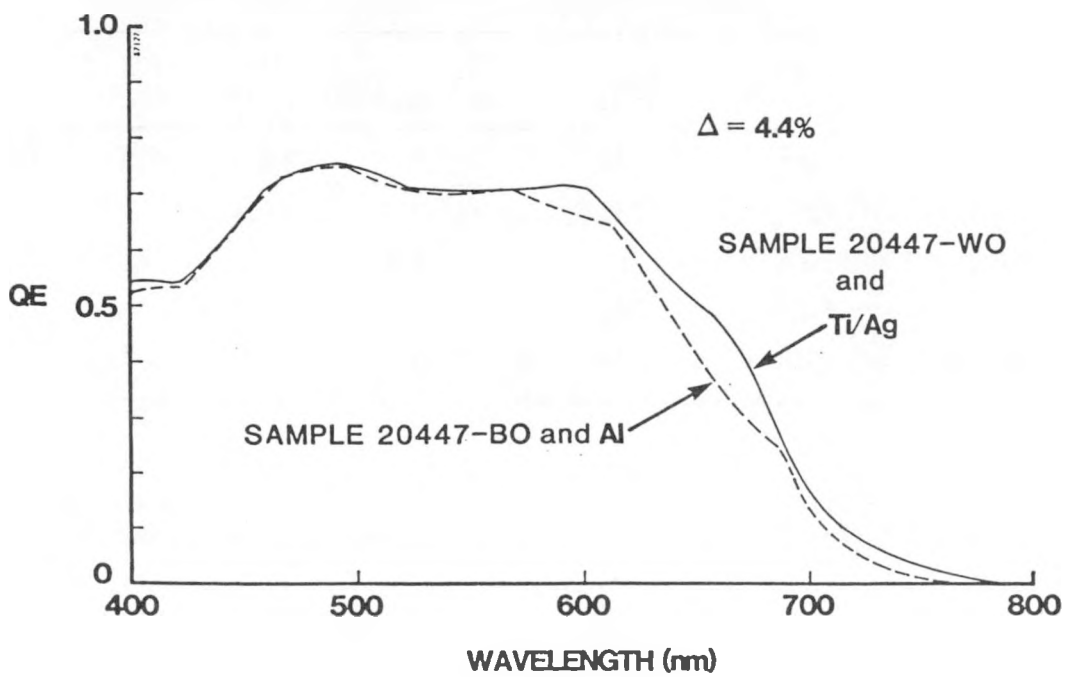

FIGURE 5-4. QUANTUM EFFICIENCY OF DEVICES WITH Al and Ti/Ag BACK CONTACTS.

Integrating the difference between the two curves over the AM1.5 spectrum between 550 nm and 800 nm, we find that the difference in projected currents is 4.4%. We then compare the light-generated currents at -1.5V for several adjacent Al and Ti/Ag cells. The results are shown in Table 5-8. The difference between the Al and TiAg back contact cells is between 3.9 and 4.3%.

TABLE 5-8. COMPARISON OF THE LIGHT-GENERATED CURRENT AT -1.5V FOR Al AND Ti/Ag BACK CONTACT CELLS.

Sample	Contact	J(-1.5V) mA/cm^2	J(Ti/Ag)/J(Al)-1 (%)
20447-W0	Ti/Ag	13.3	3.9
20447-B0	Al	12.8	
20447-W4	Ti/Ag	13.2	4.3
20447-X4	Ti/Ag	13.3	
20447-B4	Al	12.7	

Previously it was believed that the use of Ti/Ag contacts compromised the fill factor of cells in comparison to Al.[3] Table 5-9 shows the I-V characteristics of a number of adjacent Al and Ti/Ag back contact cells.

TABLE 5-9. COMPARISON OF I-V CHARACTERISTICS OF Al AND Ti/Ag BACK CONTACT CELLS FOR SAMPLE 20447.

Sample	Contact	V_{oc} (mV)	J_{sc} (mA/cm^2)	FF (%)	Eff (%)
20447-W0	Ti/Ag	797	12.9	70.5	7.3
20447-B0	Al	791	12.8	69.6	7.0
20447-W4	Ti/Ag	785	12.8	72.2	7.2
20447-X4	Ti/Ag	775	12.7	70.8	7.0
20447-B4	Al	774	12.3	70.0	6.7

Clearly, the fill factor is not reduced. The measurements suggest that, with proper process control, no fill factor penalty is paid when Ti/Ag contacts are used.

5.2.8 Effect of SnO_2 Texture on a-Si:H p-i-n Device Performance

The role of texture in improving photon collection in thin-film solar cells is well known.[14] Attempts to model this effect using different approximations has produced a variety of estimates. In what follows, we will present the results of experiments designed to measure this enhancement. Several p-i-n a-Si:H samples were fabricated by growing the layers simultaneously onto two 5 cm x 10 cm SnO_2 half substrates. One half-substrate was textured, fabricated in our SnO_2 CVD deposition chamber and the other was commercially obtained untextured material.

The results for several typical samples are shown in Table 5-10. Samples grown on textured or specular SnO_2 are denoted by the letters T and S, respectively. Both Al and Ti/Ag were used as back contact layers. The average values of the I-V parameters for all the devices of 0.1 cm^2 area with R_{sh} = 500 cm^2 are given. The "enhancement factor," $E(J_{sc}) = J_{sc}(T)/J_{sc}(S)$, calculated from the average J_{sc} (T) and J_{sc}(S) values is also listed. From Table 5-10, we note that the enhancement factor E-1 can be quite variable, with values ranging from about 10% to over 20%.

TABLE 5-10. AVERAGE I-V PARAMETERS FOR a-Si:H P-I-N DEVICES ON SPECULAR (S) AND TEXTURED (T) SnO_2 SUBSTRATES

Sample	t(i) (min)	th(i) (nm)	Back Contact	V_{oc} (mV)	J_{sc} mA/cm^2	FF (%)	Eff (%)	(E-1) (%)
20564S	35	190	Al	882	9.4	74.7	6.2	
20564T				851	10.4	71.8	6.4	10.6
20565S	35	180	Al	913	9.2	74.1	6.2	
20565T				885	10.0	73.4	6.5	8.7
20567S+	35	180	Al	848	8.6	72.2	5.2	
20567T				828	9.6	72.0	5.7	11.6
20569S	180	630	Ti/Ag	892	12.9	64.7	7.4	
20569T				847	15.0	63.2	8.1	16.3
20570S	120	390	Ti/Ag	907	1.8	62.8	6.7	
20570T				897	14.4	59.7	7.7	22.1
20571S	60	380	Ti/Ag	904	11.8	63.5	6.8	
20571T				869	14.3	65.5	8.1	21.2
20572S	90	210	Ti/Ag	916	10.2	67.6	6.3	
20572T				866	11.4	68.1	7.0	11.8
20573S	120	480	Ti/Ag	896	12.8	67.3	7.7	
20573T				859	14.6	67.8	8.5	14.1

+ No i_t-layer

TABLE 5-11. COMPARISON OF ENHANCEMENT FACTORS FROM QUANTUM EFFICIENCY AND SOLAR SIMULATOR DATA FOR CELLS OF TABLE 5-10.

Sample	Back Contact	J_{SC} (mA/cm^2)	$E(J_{SC})$-1 (%)	E(QE)-1 (%)	th(i) (nm)
20565T-A4	Al	10.26	12.1	10.1	180
20565S-B2		9.15			
20567T-A2	Al	9.52	9.7	13.5	180
20567S-A7		8.68			
20569T-B0	Ti/Ag	15.09	13.1	11.1	630
20569S-A7		13.34			
20570T-A9	Ti/Ag	14.49	24.3	13.1	390
2057S-A0		11.66			
20571T-B9	Ti/Ag	14.23	22.0	15.5	380
20571S-B9		11.66			
20572T-A9	Ti/Ag	11.42	10.7	16.9	210
20572S-A5		10.32			

If the values of $E(J_{SC})$ calculated now from J_{SC} values for selected, specific devices are compared with the ratio, $E(QE) = J_{SC}(QE)(T)/J_{SC}(QE)(S)$, where $J_{SC}(QE)$ denotes the value of J_{SC} obtained by integrating the zero bias quantum efficiency with an AM1.5 spectrum, Table 5-11 is obtained.

We note that no correlation of the enhancement with i-layer thickness is observed, and that the variation in $E(J_{SC})$ tends to be larger than that in E(QE). It is suspected that this may be related to the well-known difficulties in measuring efficiency when texture is involved, since the area of the device from which photons are collected does not necessarily coincide with the back contact area. Quantum efficiency data for two selected cells are shown in Figure 5-5, exhibiting the typical gain in the long wavelength region due to light trapping, and also a significant gain in the region below 600 nm due to reduced reflectance. We also note that not all the enhancement should be attributable to texture, since the SnO_2 absorptance may also be different. We will not attempt to model or otherwise analyze this effect here, but will use, when predicting achievable J_{SC}'s from values obtained in specular devices, a value of 15% for the enhancement due to texture. This is a conservative value when compared to previous estimates of 25%.[14]

5.2.9 High Efficiency a-Si:H Solar Cell Process

A well focused effort to achieve a-Si:H cells with efficiency over 10% by applying all the techniques described above was undertaken. The standard structure utilized for this work can be summarized as follows: a textured, highly transparent SnO_2 layer deposited in our CVD chamber is followed by a 12-15 nm p^+ a-(Si,C):H:B layer and a sharply graded transition layer of a-(Si,C):H which merges with a 600-700 nm a-Si:H i-layer and a 15-20 nm a-Si:H:P n^+ layer.

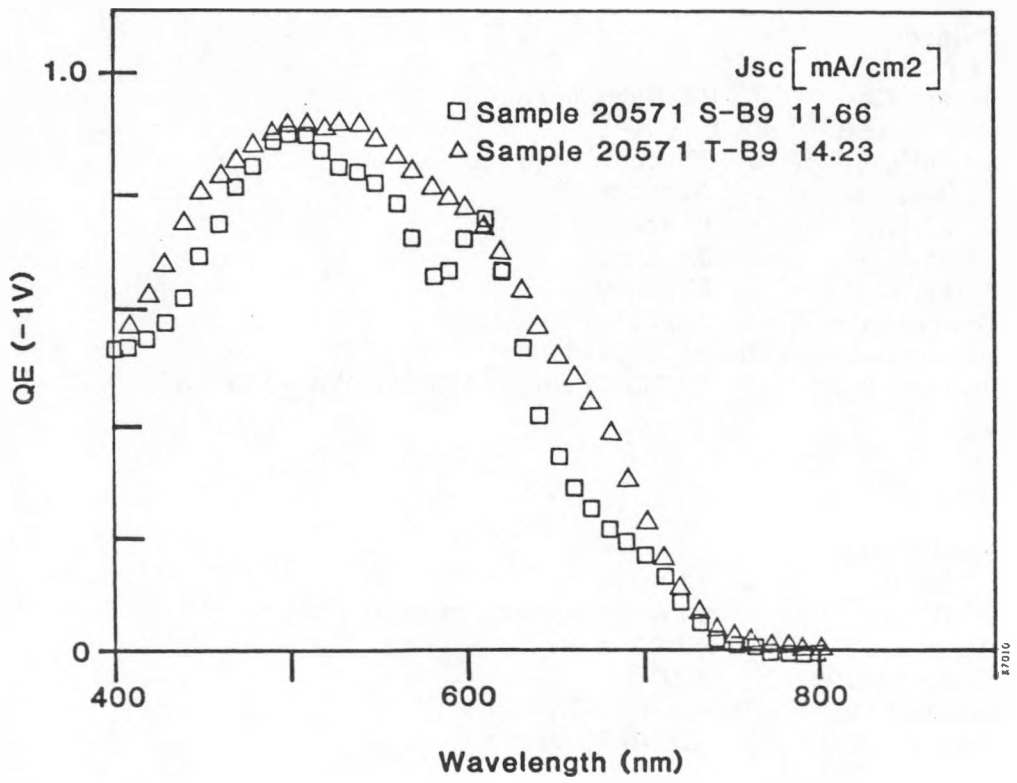

FIGURE 5-5. QUANTUM EFFICIENCY EFFECTS OF SnO_2 TEXTURE.

Several process rules were introduced in an attempt to maximize cell efficiency:

1. SnO_2 with a relatively high sheet resistance of ca. 10 Ω/□ was selected and subjected to visual inspection under a microscope to control surface defects. The SnO_2 was not cleaned prior to loading into our multi-sector reactor, to avoid surface damage.

2. A two-step p^+-layer process, consisting of a 30 s low-power plasma step followed by a 120 s deposition at full power was used in an attempt to minimize damage to the SnO_2 layer.

3. The applied substrate bias V_b was set to zero during i_t-layer deposition to minimize possible ion-bombardment damage to the p^+-layer.

4. A plasma cleaning step, not included in our standard processing (see Table 5-1), was introduced after i_t-layer deposition to avoid carbon contamination of the i-layer sector in our multi-sector reactor.

Typical preparation parameters for high-efficiency a-Si:H cells are listed in Table 5-12.

TABLE 5-12. TYPICAL PREPARATION PARAMETERS FOR a-Si:H CELLS.

1. p^+-layer

Dopant Gas: 2% B_2H_6 in He
Flow Rates:
(SiH_4) = 20 sccm
(H_2) = 30 sccm
(CH_4) = 15 sccm
(B_2H_6) = 0.2 sccm
Pressure: P = 70 mtorr
Temperature: T = 210°C
Substrate Bias Voltage: V_b = -10 V
Power: W_{rf} = 0.12-0.16 w/cm^2 (30 S) followed by 0.18 - 0.22 w/cm^2 (120 S)

2. i_t - layer

Flow Rates:
(SiH_4) = 50 sccm
(CH_4) = 15 sccm decreasing to 0 in 180 S
Pressure: P = 50-60 mtorr
Temperature: T = 300°C
Substrate Bias Voltage: V_b = 0.1-0.6 V
Power: W_{rf} = 0.20-0.30 w/cm^2

3. i-layer

Flow Rates:
(SiH_4) = 20 sccm
Pressure: P = 30 mtorr
Temperature: T = 275°C
Substrate Bias Voltage: V_b = -10 V
Power: W_{rf} = 0.18-0.20 w/cm^2

4. n^+-layer

Dopant Gas: 2% PH_3 in Ar
Flow Rates:
(SiH_4) = 20 sccm
(H_2) = 20 sccm
(PH_3) = 0.4 sccm
Pressure: P = 65-70 mtorr
Temperature: T = 325°C
Substrate Bias Voltage: V_b = 1.5-1.7 V
Power: W_{rf} = 0.25-0.30 w/cm^2

A series of ten samples were consecutively prepared according to the above rules and with close attention to process control. Table 5-13 shows the I-V characteristics of the best cells in each of the samples. The I-V characteristics of sample 20585-C9, with an efficiency of 11.0%, is shown in Figure 5-6. Another device, 20585-B9, not shown here, also attained 11.0% efficiency.

TABLE 5-13. I-V CHARACTERISTICS OF THE HIGHEST EFFICIENCY CELLS FOR EACH DEVICE SIZE IN HIGH EFFICIENCY a-Si:H SAMPLES. Device areas are nominal.

Sample	Area (cm^2)	V_{oc} (mV)	J_{sc} mA/cm^2	FF (%)	EFF (%)	Comment
20576-D7	0.1	839	16.3	67.5	9.2	One-step p^+-layer
20576-A8	0.5	859	15.1	61.9	8.0	
20577-D2	0.1	877	16.6	64.3	9.4	One-step p^+-layer
20577-A1	0.5	866	15.5	64.4	8.7	
20578-A2	0.1	868	15.9	69.1	9.5	
20578-A3	0.5	864	15.1	68.0	8.9	
20579-A5	0.1	891	15.9	68.5	9.7	
20579-A3	0.5	899	15.9	66.7	9.6	
20580-A2	0.1	878	16.4	69.7	10.1	One-step p^+-layer
20580-D1	0.5	866	15.1	66.2	8.6	
20581-D5	0.1	851	17.6	70.2	10.5	
20581-B3	0.5	896	16.6	67.0	9.9	
20581-D4	1.0	843	16.8	67.3	9.5	
20582-D0	0.1	866	16.5	71.2	10.2	
20582-C1	0.5	870	15.7	71.4	9.7	
20582-E1	1.0	848	15.9	72.1	9.7	
20583-C0	0.1	894	16.9	72.4	10.9	
20583-D1	0.5	886	16.5	71.7	10.5	
20583-A1	1.0	875	15.6	70.2	9.6	
20584-C9	0.1	909	17.0	69.1	10.7	
20584-C3	0.5	885	16.6	70.8	10.4	
20584-D1	1.0	875	15.5	65.0	8.8	
20585-C9	0.1	888	17.4	70.8	11.0	
20585-C1	0.5	861	16.7	73.5	10.6	

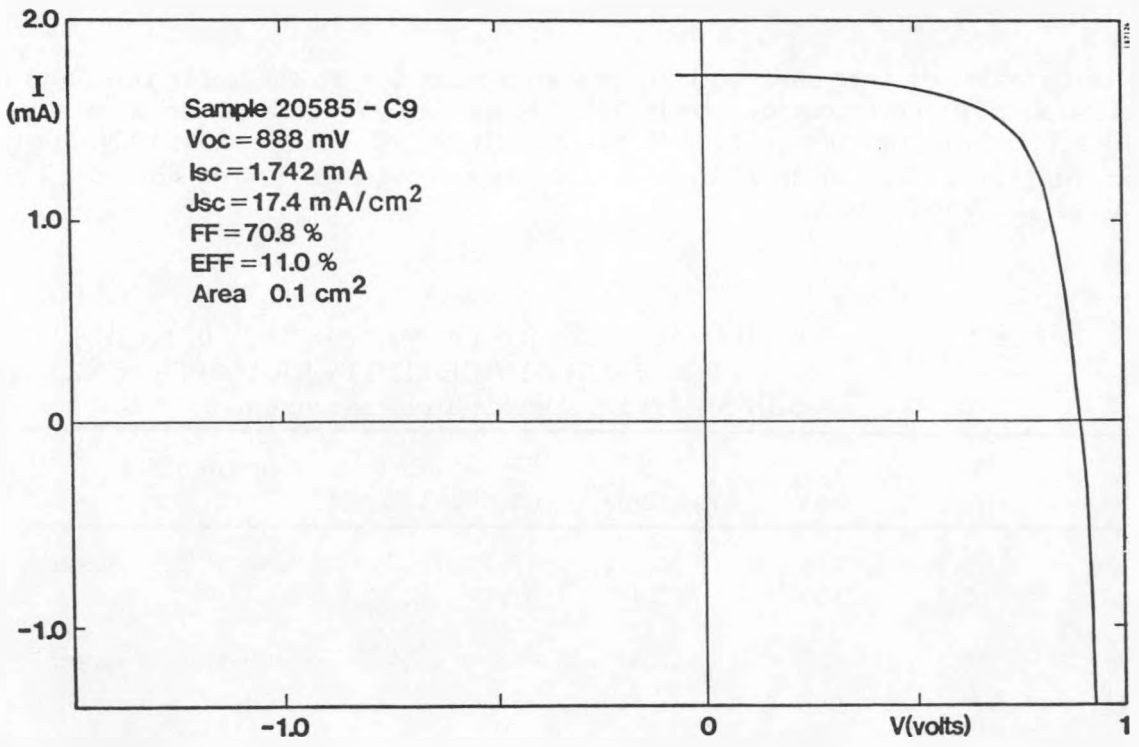

FIGURE 5-6. I-V CHARACTERISTICS OF HIGH EFFICIENCY a-Si:H CELL

The quantum efficiency of sample 20583-B2, with an efficiency of 10.0%, can be seen in Figure 5-7. The high quality of the p^+-i interface can be inferred from the low values of the ratio QE(-1V)/QE(0V) apparent from the figure.

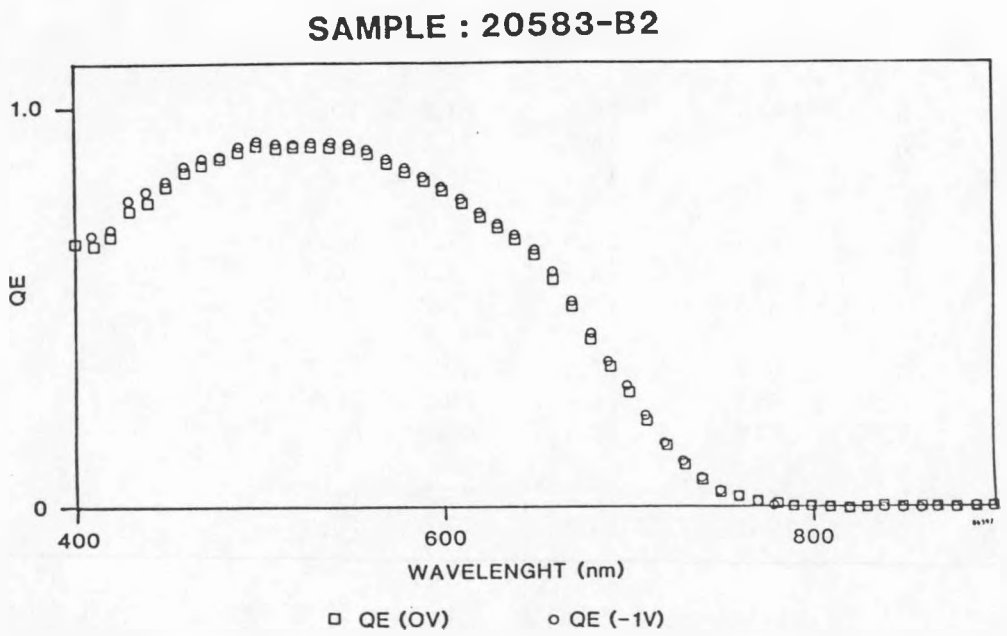

FIGURE 5-7. QUANTUM EFFICIENCY OF HIGH EFFICIENCY a-Si:H CELL.

As a measure of sample uniformity achieved, Table 5-14 shows the average I-V characteristics of 0.1 cm^2 area devices in rows A,B,C,D and E of sample 20582.

TABLE 5-14. AVERAGE I-V CHARACTERISTICS OF 0.1 cm^2 AREA DEVICES IN DIFFERENT ROWS OF SAMPLE 20582.

Row	V_{oc} (mV)	J_{sc} mA/cm^2	FF (%)	EFF (%)
A	846	15.9	71.3	9.6
B	868	15.8	71.0	9.7
C	878	15.8	70.4	9.8
D	839	16.4	71.6	9.9
E	855	16.2	73.0	10.1

5.2.10 Efficiency Measurements at SERI

Efficiency measurements at Spire were made under a simulated 100 mW/cm^2 (proposed ASTM 1985) AM1.5 global spectrum, calibrated using standard cell S-14, provided by SERI (Appendix B). Comparison with outdoor measurements shows agreement to within 2% for the measured J_{sc}. Several samples were tested by K. Emery at SERI, where the device areas were measured accurately. The results of the SERI tests are compared to the Spire results in Table 5-15, where the J_{sc}'s given for the Spire test have been recalculated using the device areas measured at SERI. Cells were tested at least twice at SERI, and only the highest efficiency results are reported here.

The I-V characteristic of the highest efficiency device, as measured at SERI, is shown in Figure 5-8.

The SERI and Spire results agree relatively well with each other. With the exception of cell 20584-C9, all other values of J_{sc} differ by 5% or less, with the Spire values systematically higher. Perhaps the biggest difference is in the measured FF values, where no systematic deviation is evident, but where the SERI data are occasionally as much as 8% lower than Spire's. To discount the possibility that the difference may be due to cell degradation, some devices were retested at Spire after the SERI test. Table 5-16 shows the results for a cell, not tested at SERI, from sample 20583, suggesting that no degradation has taken place.

TABLE 5-15. I-V CHARACTERISTICS OF HIGH EFFICIENCY a-Si:H CELLS AS TESTED AT SERI AND SPIRE. Testing at SERI on 12/9/86.

Sample	Area (cm^2)	V_{oc} (mV)	J_{sc} mA/cm^2	FF (%)	EFF (%)	Test
20583-C0	0.103	907	15.78	69.7	10.0	SERI
		894	16.37	72.4	10.6	Spire
20583-D	0.101	906	15.75	69.6	9.9	SERI
		892	16.59	72.5	10.7	Spire
20584-C9	0.100	908	15.78	71.1	10.2	SERI
		909	17.01	69.1	10.7	Spire
20584-C3	0.503	917	16.14	66.9	9.9	SERI
		885	16.54	70.8	10.3	Spire
20585-C9	0.099	878	16.63	72.2	10.5	SERI
		888	17.54	70.8	11.0	Spire
20585-B9	0.101	861	16.42	73.4	10.4	SERI
		876	17.33	71.8	10.9	Spire
20585-C1	0.503	901	16.51	68.1	10.1	SERI
		861	16.62	73.5	10.5	Spire
20582-E1	1.011	865	15.15	71.7	9.4	SERI
		848	15.73	72.1	9.6	Spire

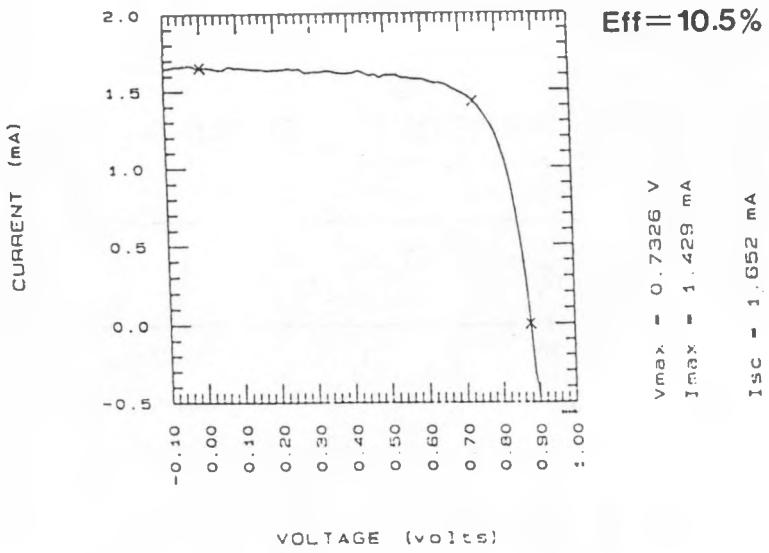

FIGURE 5-8. I-V CHARACTERISTICS OF HIGH EFFICIENCY a-Si:H CELL Number 20585-C9, AS MEASURED BY SERI.

TABLE 5-16. I-V CHARACTERISTICS OF A HIGH EFFICIENCY DEVICE BEFORE AND AFTER TESTING AT SERI ON 12/09/86.

Sample	Area (cm^2)	V_{OC} (mV)	J_{SC} mA/cm^2	FF (%)	EFF (%)	Test Date
20583-C6	0.1	834	16.2	74.0	10.0	11/20/86
		847	17.0	73.3	10.6	12/19/86

5.3 a-(Si,Ge):H SINGLE-JUNCTION CELLS

The efficiency of single-junction a-(Si,Ge):H p-i-n cells is a strong function of the bandgap of the a-(Si,Ge):H i-layer. Table 5-17 shows the I-V characteristics for the highest efficiency cells reported earlier in this program.

TABLE 5-17. CHARACTERISTICS OF SINGLE-JUNCTION a-(Si,Ge):H CELLS. Nominal area = 0.1 cm^2.

Sample	E_g (eV)	V_{oc} (mV)	J_{sc} (mA/cm^2)	FF (%)	Eff (%)	Comments
1495	1.53	720	14.1	56.0	5.7	Reference (9)
1682-A8	1.60	769	13.9	60.5	6.5	Reference (9)
20255-B8	1.66	736	16.1	56.4	6.8	Reference (5)
20276-B5	Graded bandgap	788	15.1	63.0	7.5	Reference (4)

A decrease in efficiency is observed, with a lower bandgap. Analysis of the FF of a-(Si,Ge):H cells shows that efficiency losses arise from a decrease in collection efficiency with increasing forward bias voltage applied to the junction. This is due, in turn, to the lower mobility-lifetime product for electron and hole transport that is generally observed in a-(Si,Ge):H.

In trying to build high efficiency a-(Si,Ge):H single-junction structures, it has been determined[4] that grading the i-layer from a-Si:H to a-(Si,Ge):H with the maximum (Ge)/(Si) ratio near the n^+-layer enhances V_{oc} and FF of otherwise identical cells (Table 5-17).

The advantages of the graded bandgap structure is derived from the following:

1. Higher V_{oc}, due to reduced recombination in the higher quality a-(Si,C):H region near the p^+/i-interface.

2. Higher FF due to the enhanced electron transport caused by the conduction band grading and the resulting increase in the drift-field.

3. Increased QE in the wavelength region ≥ 600 nm due to improved hole transport through the lower (Ge)/(Si + Ge) region of the i-layer.

However, the J_{sc} of the graded bandgap a-(Si,Ge):H cell has been limited to 15-16 mA/cm^2 (that is, the same as obtained in a-Si:H cells), possibly as a result of the decrease in carrier generation due to the higher bandgap obtained throughout most of the i-layer, as compared to the ungraded case. Therefore, efforts during the last phase of this program were concentrated into two main areas:

1. The development of an a-(Si,Ge):H layer with a bandgap $E_g < 1.5$ eV, to obtain the highest light-generated current.

2. The improvement of i-layer grading techniques for maximum collection efficiency.

5.3.1 Deposition of Low Bandgap a-(SiGe):H Alloys

As in the case of a-Si:H i-layers, the optimum process conditions for a-(Si,Ge):H i-layers were investigated through the use of device analysis techniques. The same structure developed in a-Si:H single-junction cell research was used with three differences: a thin transition layer graded from a-(Si,C):H to a-(SiGe):H, the a-Si:H i-layer substituted by a low bandgap a-(Si,Ge):H i-layer, and an a-(Si,Ge):H:P n^+-layer. The I-V characteristics and quantum efficiency of the devices thus constructed were used to analyze the quality of the i-layer alloy material.

The basic device structure utilized was:

1. A 10-15 nm thick, highly conductive and transparent a-(Si,C):H:B p^+-layer.

2. A thin (ca. 10 nm), sharply graded a-(Si,C):H transition layer in which the C concentration decreases to zero from that in the p^+-layer.

3. A thin (10-15 nm), sharply graded a-(Si,Ge):H transition layer in which the Ge concentration increases from zero to that obtaining in the bulk i-layer.

4. An a-(Si,Ge):H i-layer of constant (Si)/(Ge) ratio.

5. An a-(Si,Ge):H n^+-layer.

A factorial experimental technique was initially used to obtain a measure of the trends in device properties as the H_2 flow rate (H_2), substrate temperature T, and RF power W_{rf} are varied between two levels. Since our concern is with the ability of the alloy i-layer to generate and collect carriers in the near infrared wavelength range, quantum efficiency data were chiefly used in evaluating this experiment. Process conditions for the i-layer in this set of samples were as follows:

SiH_4 flow rate:	(SiH_4)	=	20 sccm
H_2 flow rate:	(H_2)	=	10 and 40 sccm
GeH_4 flow rate:	(GeH_4)	=	6 sccm
RF Power:	W_{rf}	=	0.80 and 0.20 W/cm^2
Temperature:	T	=	240 and 300°C
Pressure:	P	=	30-50 mtorr
Substrate Bias Voltage:	V_b	=	-10V

Process conditions for the p^+ and transition layers were as given in Table 5-12. The n^+-layer was always deposited under the same conditions as the i-layer with W_{rf} = 0.25-0.30 W/cm^2 and the addition of 0.4 sccm of PH_3. The results of this experiment were inconclusive relative to the variables (H_2) and W_{rf}, possibly due to the experimental layout with only two levels or to the narrow range of variation given these variables. It was found that T, which was varied from 240°C to 350°C was by far the most significant variable, with the high temperature (350°C) giving the best result, as seen from the data summarized in Table 5-18.

TABLE 5-18. RESULTS OF INITIAL a-(Si,Ge):H i-LAYER DEVELOPMENT. Device area is 0.1 cm^2. E_o is the Urbach edge slope.

Sample	T (°C)	E_o (meV)	J(-1 V) mA/cm^2	1-[QE(-1V)/QE(0V)] in % (450 nm)	(750 nm)	(800nm)
20482-B7	240	88.8	15.0	1.9	2.9	2.9
20491-A5	300	49.7	13.0	1.2	1.2	1.2
20489-C7	350	46.3	13.0	1.1	1.1	1.1

In this table, data on quantum efficiency ratios (-1V/0V) at 450, 750 and 800 nm are given for the highest efficiency cell in each sample, indicating that both electron and hole collection are best for samples grown at 350°C. The values of J(-1V) serve as an indication of the current-generating capacity of the alloy i-layers, and the characteristic energy of the Urbach tail, E_o, as measured from the logarithm of the quantum efficiency as a function of energy,[15] as a measure of layer quality. Typical values for a-Si:H i-layers are below 40 meV. We conclude from these data that deposition at 240°C, while expected to result in a-(Si,Ge):H with higher H_2 content and thus better transport properties, in fact yields samples of inferior quality .

In a second factorial experiment, a more thorough investigation of the plasma variables was undertaken. The total flow Q_t = (SiH_4) +(GeH_4) + (H_2), the pressure P, the RF power level, as monitored by the peak-to-peak RF voltage applied to the plasma V_{rf}, and the temperature T were varied between three levels. In this way, the residence time and the plasma composition were varied. The levels chosen are given in Table 5-19.

TABLE 5-19. VARIABLES AND LEVELS FOR ALLOY OPTIMIZATION

Variable	Units	Level Low	Medium	High
Q_t	(sccm)	16	32.5	65
T	(°C)	325	350	375
Pressure	(mtorr)	25	66	80
V_{rf}	(V)	2.6	4	5.4

The experiment consisted of nine runs. The following device characteristics and material properties were used to measure experimental success:

1. Bandgap E_g (QE), as determined from quantum efficiency data.

2. Fill factor.

3. The product EFF* = (V_{oc}) (FF)(J(-1.5V)).

To allow for a meaningful comparison, all samples were grown to approximately the same thickness (200-250 nm).

The criteria for the selection of the best values of the deposition parameters were high values of the average EFF* and FF, along with low values of E_g (QE). These values were calculated by averaging the corresponding data for the best cell in each experiment for all experiments for which a particular variable has a given value. Figure 5-9 shows the plots of EFF*, E_g (QE) and FF as a function of the four variables being tested. Values of E_g(QE) are relative and only taken as a guide.

On analysis, it appears that the following conditions will result in the best quality a-(Si,Ge):H cells:

1. Substrate Temperature, T = 375°C.
2. Peak-to-peak RF voltage, V_{rf} = 2.4V.
3. Total System Pressure, P = 65 mtorr.
4. Total flow Rate, Q_t = 65 sccm.

The above conditions would be expected to result in slow film growth and lessened clustering of Si and Ge atoms in the film. It is not necessarily surprising that the deposited film would be of higher quality.

The I-V characteristics and values of E_o and quantum efficiency at several wavelengths of a cell made using the above conditions are shown in Table 5-20, and compared with those of an a-Si:H single-junction cell of comparable thickness (150-200 nm). The corresponding quantum efficiencies are shown in Figures 5-10 and 5-11. The shift towards lower energies in the quantum efficiency of cell 20505 is E_g = 300 mV, consistent with a band gap E_g = 1.45 - 1.50 eV for this sample. In fact, an optical band gap measurement of an i-layer deposited under the same conditions as that in sample 20505 (see Section 3), yielded E_g = 1.45 eV.

We note that the FF of cell 20505-A5 is relatively low, although the QE(-1V)/QE(0V) ratio at 800 nm is 1.13, good by comparison with earlier ungraded samples. Problems arising from the changes in the alloy composition at the p^+-i interface could be responsible for this, as suggested by the relatively high ratio at 450 nm. In further experiments, we investigated the effects of utilizing a-Si:H:P n^+ layers and of grading at the front and back of the i-layer. Unless explicitly stated, the i-layer composition will be understood in what follows to be the same as in sample 20505.

In all the preceding a-(Si,Ge):H single-junction cell work, the p^+-layer and a-(Si,C):H transition layer process have been the same as for the a-Si:H single-junction cell. The process conditions for the a-(Si,Ge):H transition layer, i-layer and n^+-layer are summarized in Table 5-21.

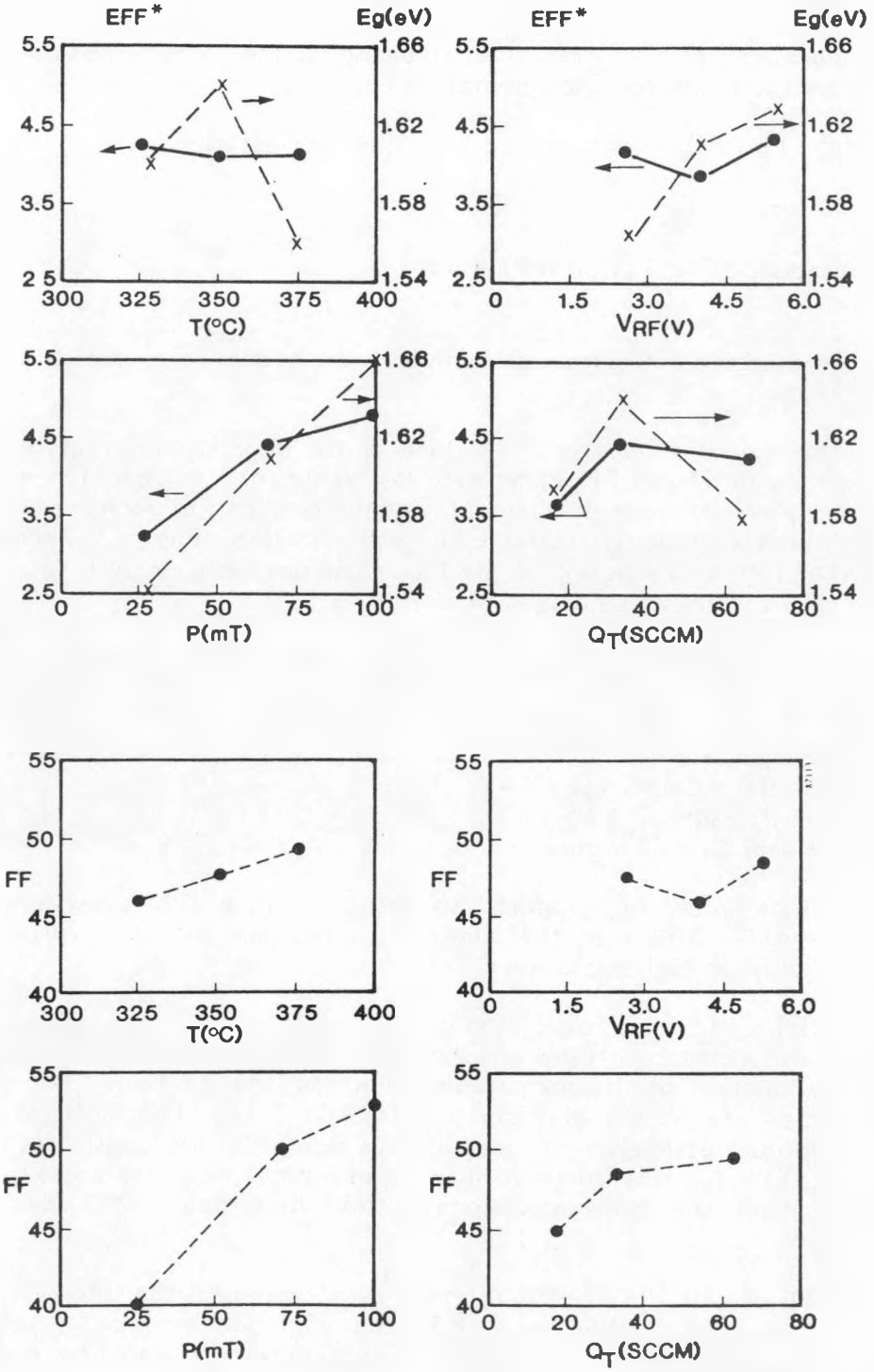

FIGURE 5-9. EFF*, E_g AND FF FOR FACTORIAL OPTIMIZATION.

TABLE 5-20. DEVICE PARAMETERS OF a-Si:H (20556-C0) and a-(Si,Ge):H (20505-A5) CELLS FABRICATED ACCORDING TO THE OPTIMUM PLASMA CONDITIONS. Area 0.1 cm^2.

Sample	V_{oc} (mV)	J_{sc} mA/cm^2	FF (%)	EFF (%)	E_o (meV)	E_g(QE)
20505-A5	638	12.6	52.2	4.2	48.0	1.45-1.50
20556-C0	898	9.5	72.6	6.2	39.2	1.75-1.80

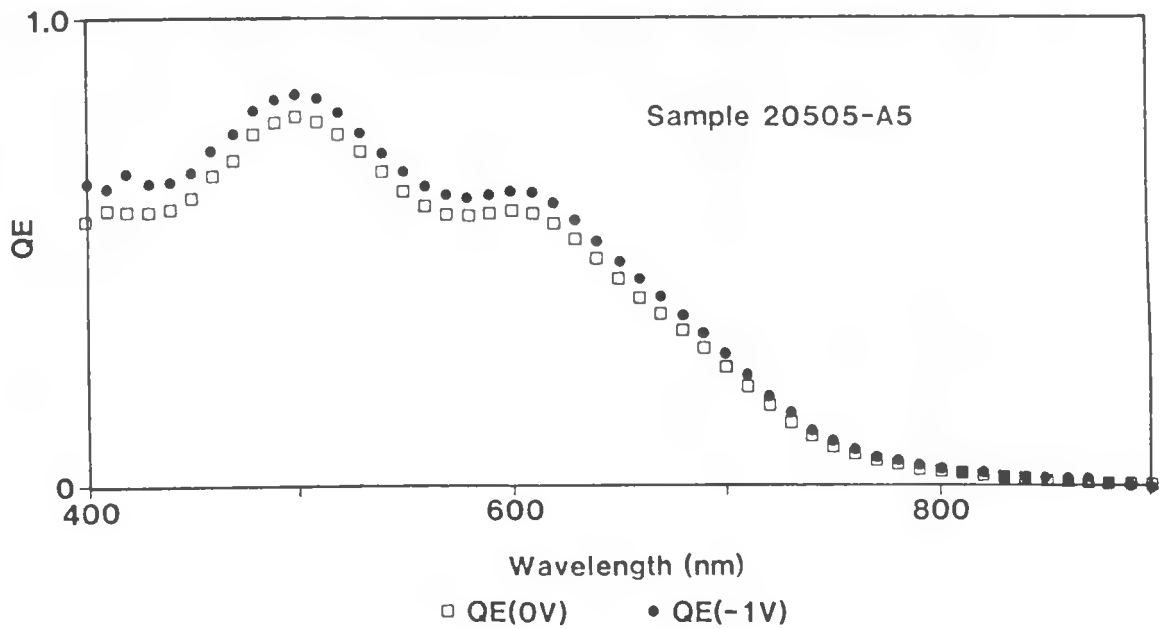

FIGURE 5-10. QUANTUM EFFICIENCY OF a-(Si,Ge):H CELL WITH E_g = 1.45-1.50 eV.

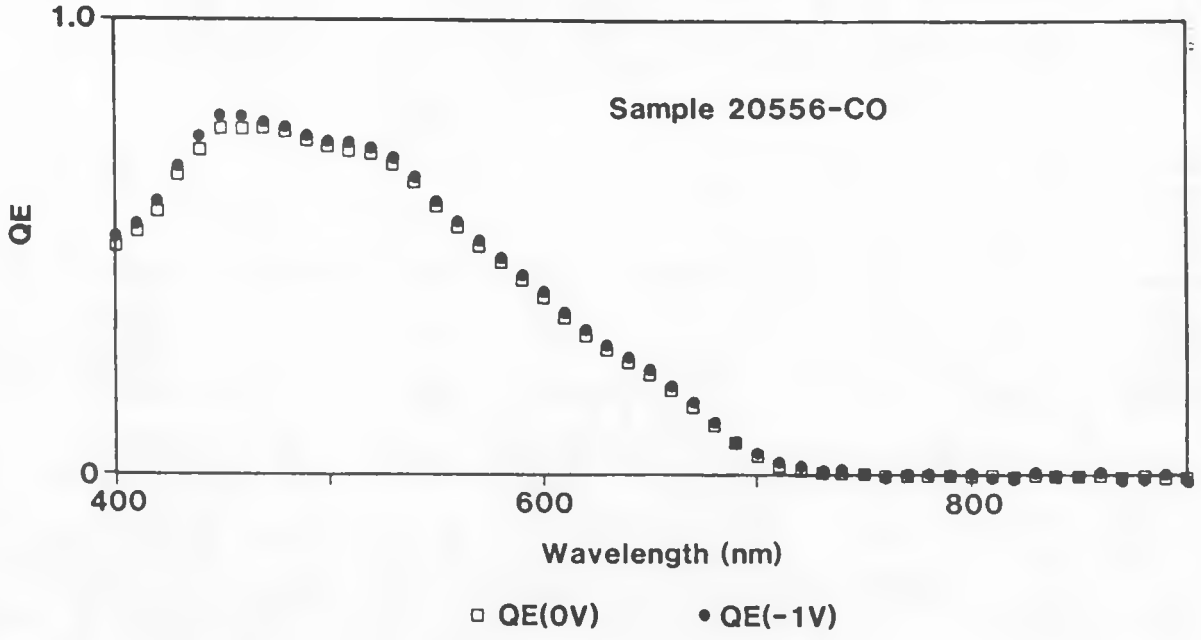

FIGURE 5-11. QUANTUM EFFICIENCY OF a-Si:H CELL WITH E_g = 1.75 - 1.80 eV.

TABLE 5-21. PROCESS PARAMETERS FOR a-(Si,Ge):H TRANSITION, I AND N^+-LAYERS.

Layer	Gas Flows (sccm) (SiH_4)	(GeH_4)	(H_2)	(PH_3)	T (°C)	P (mtorr)	t (min)	W_{rf} (W/cm^2)	V_{rf} (V)
Transition	40	0-12	10	-	350	60-70	5	0.10	2.5
Intrinsic	40	12	20	-	350	60-70	-	0.10	2.5
N^+	20	4.25	10	1	325	60-70	10	0.30	3.8

5.3.2 N^+ Layers in a-(Si,Ge):H Cells

Lower values of V_{OC} and FF may result from a low conductivity n^+-layer. In a series of experiments, the performance of devices with a-Si:H:P and a-(Si,Ge):H:P was compared. The results are shown in Table 5-22.

TABLE 5-22. I-V CHARACTERISTICS OF a-(Si,Ge):H CELLS WITH a-Si:H:P AND A-(Si,Ge):H:P N^+-LAYERS. Area = 0.1 cm^2.

Sample	N^+-Layer	E_o (meV)	V_{OC} (mV)	J_{SC} mA/cm^2	FF (%)	EFF (%)
20519-C9	a-(Si,Ge):H:P	49.2	561	12.7	55.9	4.0
20522-A7	a-Si:H:P	52.9	667	12.8	63.6	5.4

A sharp grading between the a-(Si,Ge):H i-layer and the a-Si:H:P was used for sample 20522-A7, with a transition layer thickness estimated as ca. 10 nm. A considerable improvement in V_{OC} and in the QE(-1V)/QE(0V) ratio is noted at all wavelengths (Figure 5-12). While a V_{OC} increase could be due to a lower activation energy for n^+ a-Si:H:P, the latter result is not well understood, since it would imply a change in the hole affinity near the n^+-layer, in contradiction to existing models.[3,16] In an attempt to obtain additional information on transition layer effects and improve carrier collection in a-(Si,Ge):H devices, this matter was pursued in additional experiments.

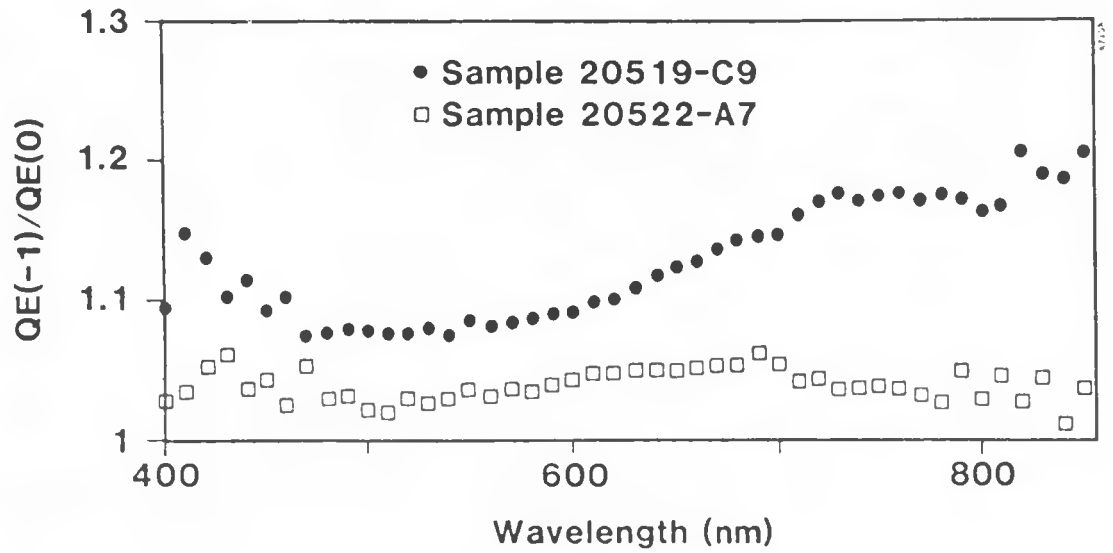

FIGURE 5-12. QUANTUM EFFICIENCY RATIOS FOR CELLS WITH a-(Si,Ge):H:P AND a-Si:H:P n^+-LAYERS.

5.3.3 Transition Layers in a-(Si,Ge):H Single-Junction Cells

Several experiments were carried out in which the thickness of the transition layer at the p^+ (a-(Si,C):H:B)-i and i-n^+ (a-Si:H:P) interfaces was varied. The structure of the devices built for this effort was as follows:

1. A 10-15 nm thick, highly conductive and transparent a-(Si,C):H:B p^+-layer.

2. A thin (ca. 10 nm), sharply graded a-(Si,C):H transition layer in which the C concentration decreases to zero from that in the p^+-layer.

3. A graded a-(Si,Ge):H transition layer with thickness between 10 and 100 nm in which the Ge concentration increases from zero to that obtained in the bulk i-layer.

4. An a-(Si,Ge)H i-layer of constant (Si)/(Ge) ratio.

5. A graded a-(Si,Ge):H transition layer with thickness between 10 and 100 nm in which the Ge concentration decreases from that in the i-layer to zero at the n^+ layer.

6. An a-Si:H:P n^+-layer.

The following process parameters were used for the a-(Si,Ge):H transition layer (front transition layer) connecting the a-(Si,C):H transition layer to the a-(Si,Ge):H, constant composition i-layer:

1. Thin Front Transition Layer (TNFTL)

   t = 5-6 m

   T = 350°C

   P = 60-70 mTorr

   W_{rf} = 0.08-0.10 W/cm^2 (V_{rf} = (2.5 $\pm$ 0.1) V)

   (SiH_4) = 40 sccm

   (GeH_4) = 0-12 sccm

   (H_2) = 10 sccm

2. Thick Front Transition Layer (TKFTL)

   t = 10-30 m

   T = 350°C

   P = 60-70 mTorr

   W_{rf} = 0.08-0.10 W/cm^2 = (V_{rf} = (2.5 $\pm$ 0.1) V)

   (SiH_4) = 20-40 sccm

   (GeH_4) = 0-12 sccm

   (H_2) = 20 sccm

For the transition layer connecting the i-layer to the n^+ layer (back transition layer), the following parameters were used:

1. Thin Back Transition Layer (TNBTL)

   t = 5 m

   T = 350°C

   P = 60-70 mTorr

   W_{rf} = 0.08 -0.10 W/cm^2 (V_{rf} = (2.5 $\pm$ 0.1) V)

   (SiH_4) = 40 sccm

   (GeH_4) = 0 sccm

   (H_2) = 10 sccm

2. Thick Back Transition Layer (TKBTL)

t = 15-30 m

T = 350°C

P = 20-70 mTorr

W_{rf} = 0.10-0.12 W/cm^2 (V_{rf} = (4.4 ±0.1) V)

(SiH_4) = 40-20 sccm

(GeH_4) = 20-0 sccm

(H_2) = 20-0 sccm

In this series of experiments, a variable i-layer thickness was obtained by varying the deposition time. The n^+-layer process was as in sample 20505, but with a GeH_4 flow (GeH_4) = 0. The sequence of experiments was as shown in Table 5-23, where the average I-V parameters for all the 0.1 cm^2 devices with R_{sh} = 500/cm^2 and i-layer and front (FTL) and back (BTL) transition layer thickness estimated from optically measured sample thickness and knowledge of time-varying deposition rates are also given.

TABLE 5-23. PROCESS AND I-V PARAMETERS FOR a-(Si,Ge):H ALLOY DEVICE FRONT AND BACK TRANSITION LAYER GRADING. Aluminum back contacts, 0.1 cm^2 area.

Sample	Front Grade Type/Time (min)	Thickness FTL (nm)	i (nm)	BTL (nm)	Back Grade Type/Time (min)	E_o (meV)	V_{oc} (mV)	J_{sc} (mA/cm^2)	FF (%)	Eff (%)
20521	TNFTL/5	15	135	30	TKBTL/30	53.2	623	14.7	56.7	5.2
20523	TNFTL/5	15	135	5	TNBTL/5	--	622	14.6	48.8	4.4
20524	TNFTL/5	15	200	30	TKBTL/30	48.5	590	15.7	53.1	5.0
20525	TKFTL/30	90	200	30	TKBTL/30	42.6	652	15.6	44.1	4.5
20526	TNFTL/5	15	205	30	TKBTL/30	43.0	605	15.6	54.5	5.1
20528	TKFTL/15	45	140	15	TKBTL/15	63.0	644	14.8	55.8	5.3

The values of the Urbach edge energy E_o are also listed for completeness, when available. Since only the a-(Si,Ge):H i-layer contributes to the reverse bias quantum efficiency QE(-1 V) in the wavelength range > 800 nm, from which E_o is obtained, one would expect a constant value of E_o for the samples in Table 5-23, having the same i-layer. In fact, with the exception of sample 20528, the values of E_o differ by less than 10 meV. A smaller variation, on the order of 5 meV, is typically observed in aSi:H i-layers and this difference is not presently understood unless it can be attributed to a lesser reproducibility of the a-(Si,Ge):H deposition.

From the first two samples listed, a relatively wide back transition layer seems to be favored. From the quantum efficiency ratios QE(-1V)/QE(0V) for the two best cells in each sample (Figure 5-13), hole collection, as measured by the ratio in the 800 nm wavelength region, seems to be the reason for the higher FF of the sample with the wide back transition region.

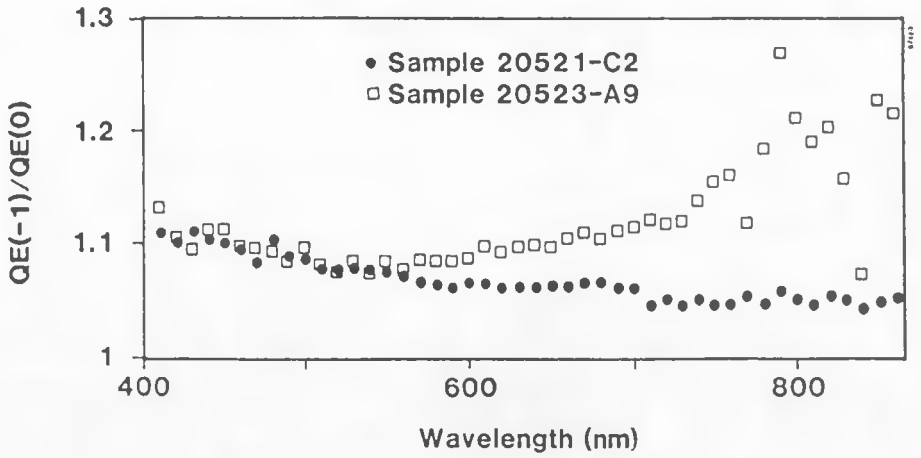

FIGURE 5-13. QUANTUM EFFICIENCY RATIOS FOR a-(Si,Ge):H CELLS WITH FRONT AND BACK TRANSITION LAYER GRADING.

If one assumes that the hole affinity of the a-(Si,Ge):H alloy is constant as the (Ge)/(Si) ratio changes, a narrow back transition layer may cause a potential barrier for electrons to appear near the n^+ a-(Si,Ge):H:P layer, thus decreasing the minority carrier (hole) lifetime in that region (Figure 5-14). As the transition layer width is increased, the electric field near the i-n^+ interface changes sign and the potential barrier disappears, thus enhancing hole collection from that region.

The i-layer deposition time was extended for the next two samples in order to obtain a higher light-generated current. In this case, the thin front transition layer seems preferable. Quantum efficiency data for the best cells (Figure 5-14) indicate that the thicker a-(Si,Ge):H transition layer enhances V_{OC} and electron collection, consistent with the effect of the a-(Si,C):H transition layer. The relative loss in hole current apparent in Figure 5-15 can be explained by the effect of the added i-layer bulk contributing to recombination.

Finally, samples 20526 and 20528 were grown with intermediate transition layer and i-layer thicknesses. We note that sample 20528, having the thicker front transition layer, exhibits higher V_{OC}. However, it is apparent that material quality is a limiting factor, since thicker i-layers yield higher J_{SC} but lower FF to produce cells of essentially the same efficiency.

The effect of increased H_2 dilution on a-(Si,Ge):H quality has previously been reported by this group. In order to assess its effect on the quality of the 1.45 eV alloy developed here, a p-i-n a-(Si,Ge):H device was fabricated using an increased H_2 flow rate of 100 sccm, other process variables remaining constant. The sample (20529), made on specular SnO_2, exhibited an Urbach edge energy E_o = 47.6 meV, that is, it failed to show a significant decrease in E_o, as expected from increased dilution. This sample achieved light-generated currents $J_L = J$ (-1.5 V) in excess of 19 mA/cm^2 (Figure 5-16). Its J_{SC}, however, was substantially reduced by collection problems.

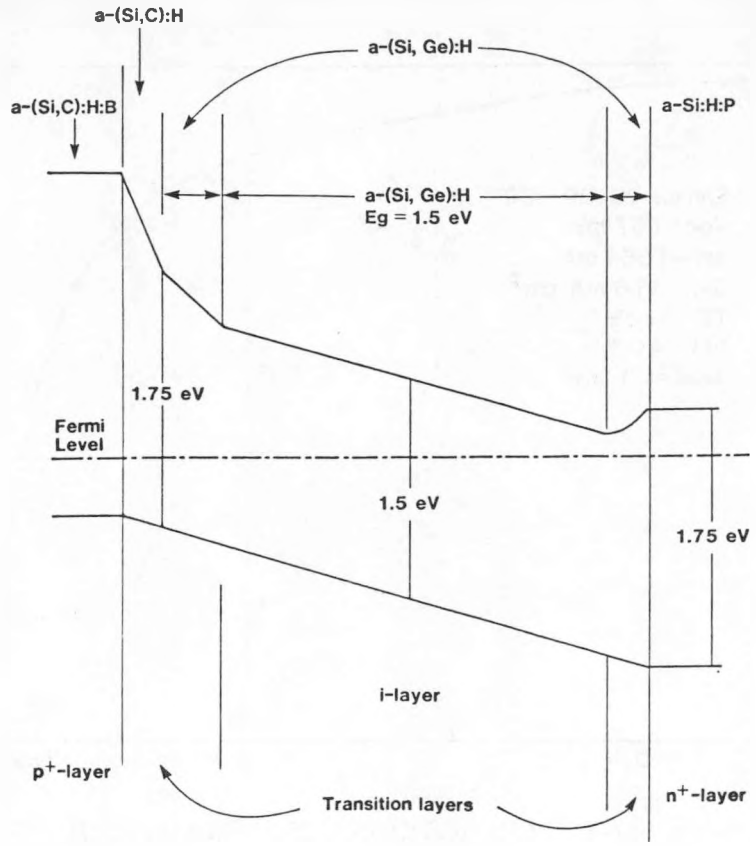

FIGURE 5-14. BAND DIAGRAM OF a-(Si,Ge):H CELL WITH FRONT AND BACK TRANSITION LAYERS.

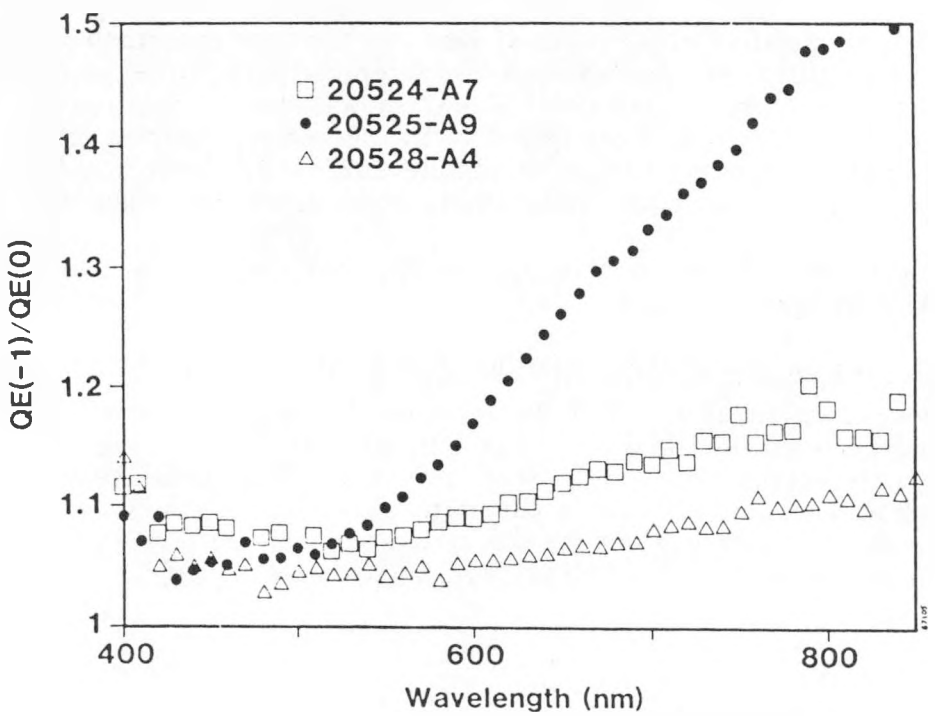

FIGURE 5-15. QUANTUM EFFICIENCY DATA FOR CELLS WITH a-(Si,Ge):H GRADED TRANSITION LAYERS.

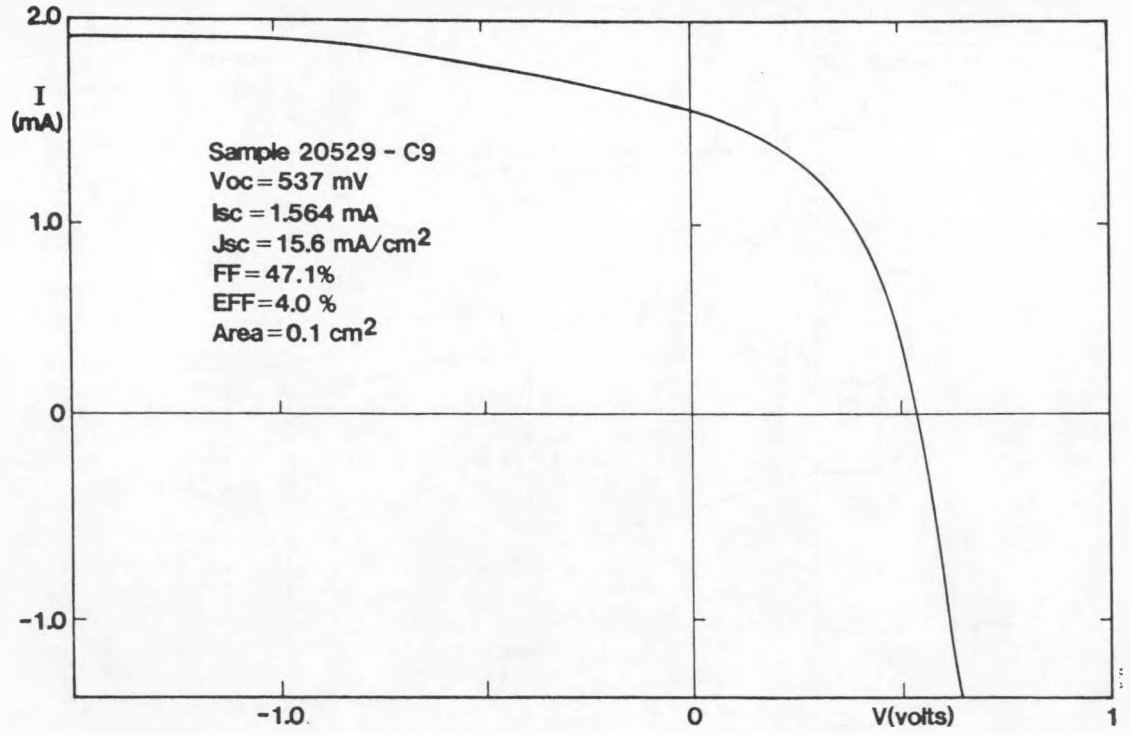

FIGURE 5-16. I-V CHARACTERISTICS OF a-(Si,Ge):H CELL 20529

A comparison with previous results for ungraded i-layers (Table 5-24) shows that the a-(Si,Ge):H alloy cells developed during this last six month period are comparable in performance to the lower bandgap cells (sample 1495). The present alloy, however, has a lower bandgap and can thus generate a higher current.

A comparison of the quantum efficiencies of a cell of the type reported here with that of a cell from the previously reported high efficiency, graded a-(Si,Ge):H sample (20276) can be seen in Figure 5-17. Clearly, sample 20528-A7 shows a better response in the spectral region beyond 700 nm. This can be attributed to the decrease in carrier generation due to the excess a-Si:H in the graded i-layer of sample 20276-A7. While the V_{OC} and FF of sample 20276-A7 were higher, sample 20524-A7 is more suited for tandem application.

In order to help predict the achievable J_{SC}, we analyze the photon losses of a typical a-(Si,Ge):H cell in paragraph 5.3.4.

5.3.4 Photon Losses for a-(Si,Ge):H Single-Junction Cells

A photon economy analysis of a cell of the type developed can be done using the optical model previously applied to a-Si:H. If the optical constants of the front and back transition layers are approximated by those of a-Si:H, the light-generated current J_L(NR) of a device such as sample 20523 can be calculated. Table 5-24 shows the results of such a calculation, where literature values for the optical constants of 1.5 eV a-(Si,Ge):H have been used as an approximation[13] and layer thicknesses are estimated.

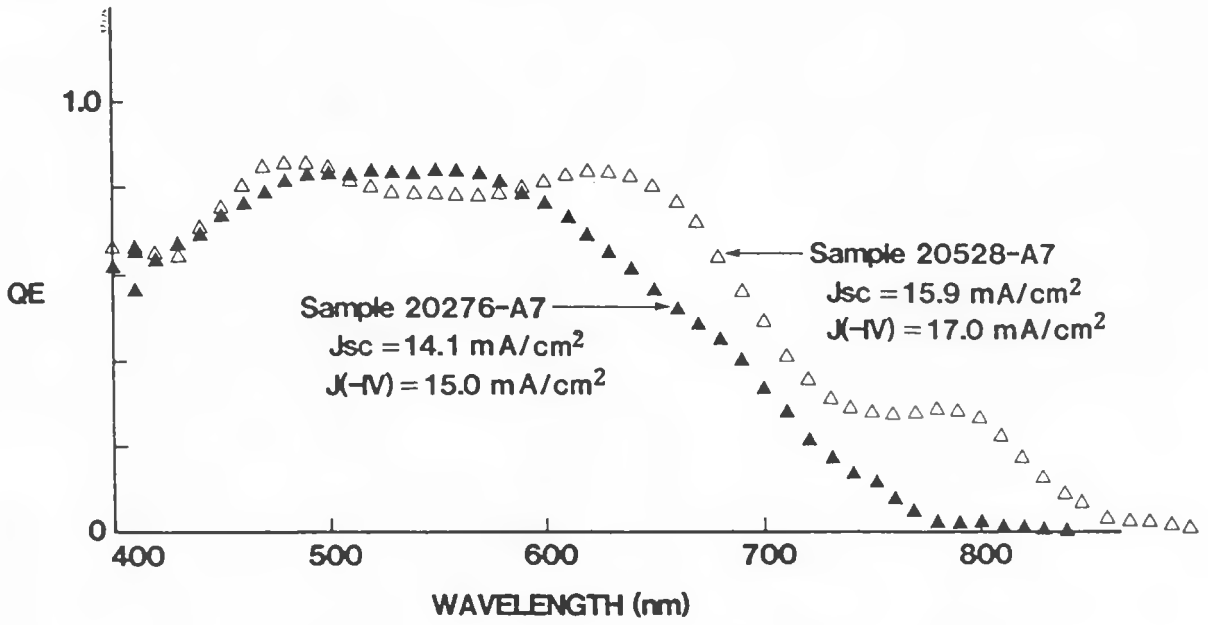

FIGURE 5-17. QUANTUM EFFICIENCY COMPARISON FOR a-(Si,Ge):H CELLS WITH GRADED TRANSITION LAYERS.

TABLE 5-24. LOSSES AND LIGHT-GENERATED CURRENT IN TYPICAL a-(Si,Ge):H SINGLE-JUNCTION CELL

Layer	Thickness (nm)	Loss (mA/cm^2)	J_L (NR) (mA/cm^2)
Glass	-	0.2	0
SnO_2	500	3.4	0
p^+	15	0.9	-
FTL	15	-	0.9
i	135	-	14.9
BTL	5	-	0.2
n^+	15	0.2	-
Aluminum	500	1.7	-
Totals		6.2	16.0

From this table, it is clear that the light-generated current expected from this structure exceeds the current measured, typically in the range 14 mA/cm^2, which suggests that a significant recombination, as large as 15%, takes place even for samples with i-layers as thin as 135 nm. Recall (see Section 5.2.4) that the agreement was quite good for a-Si:H cells, for which recombination in thin i-layers was negligible. This agrees with the conclusion drawn from the I-V characteristics discussed in section 5.3.2: the recombination losses in the 1.45 - 1.50 eV band gap a-(Si,Ge):H i-layer of the type developed here limit the achievable eficiency to below 6%.

A calculation of J_L for a p-i-n device with variable i-layer thickness and silver back contacts is shown in Table 5-25. In this table, $J_L(NR)^*$ is the light-generated current calculated with a 15% enhancement factor that could be achieved with SnO_2 texture (see Section 5.2.8).

TABLE 5-25. LIGHT-GENERATED CURRENT AND PHOTON LOSSES FOR a-(Si,Ge):H CELL

i-Layer Thickness	$J_L(NR)$ (mA/cm^2)	$J_L(NR)^*$ (mA/cm^2)	Photon Loss (mA/cm^2)			
			SnO_2	p^+-layer	n^+-layer	Silver
100	15.6	17.9	1.49	0.87	0.34	0.32
150	16.3	18.7	1.45	0.87	0.20	0.16
200	17.9	20.6	1.39	0.87	0.11	0.19
300	18.8	21.6	1.36	0.87	0.05	0.13
400	19.3	22.2	1.52	0.87	0.02	0.14
500	19.7	22.7	1.32	0.87	0.01	0.08
600	20.4	23.5	1.31	0.87	0.01	0.07

Note: Layer thicknesses are: $t(SnO_2)$ = 200 nm, $t(p^+)$ = 15 nm, $t(n^+)$ = 15 nm, t (Ag) = 500 nm

The data in this table suggest that in order to achieve a-(Si,Ge):H cells with efficiencies about 9%, requiring $J_{SC} \geq 23$ mA/cm^2 if V_{OC} = 650 mV and FF as high as 60% could be reached, i-layers as thick as 600 nm would be necessary if SnO_2 of the same quality as that used in the a-Si:H effort were employed.

Based on the above discussion, a substantial improvement in the electronic properties of the a-(Si,Ge):H i-layer is needed before minority carrier diffusion lengths L could be obtained such that $L/t(i) \geq 1$, as required for efficient carrier collection. Further research into better deposition methods is necessary to accomplish this.

SECTION 6

TANDEM-JUNCTION CELL RESEARCH

As a consequence of the efforts on both a-Si:H and a-Si,Ge:H single-junction cells, a number of substrates containing tandem cells were fabricated during the initial part of this program incorporating features of the successful single junction cells. Table 6-1 lists the results of the best a-Si:H/a-Si:H and a-Si:H/a-Si,Ge:H cells. Cell area is 0.1 cm^2. Estimates of the top and bottom cell bandgaps from quantum efficiency data are subject to considerable error and will not be cited here.

TABLE 6-1. I-V CHARACTERISTICS OF BEST TANDEM CELLS FOR SPECIFIED SUBSTRATE. Area = 0.1 cm^2.

SUBSTRATE/CELL	V_{OC} (V)	J_{SC} (mA/cm^2)	FF (%)	Eff (%)
A. a-Si:H/a-Si:H				
20324/B5	1.637	6.7	67.2	7.4
20309/A7	1.661	5.9	66.0	6.5
20303/C1	1.557	6.4	60.5	6.1
20326/A7	1.616	6.3	66.4	5.8
20285/A3	1.630	5.1	66.8	5.5
20311/B8	1.661	5.9	68.4	5.5
B. a-Si:H/a-Si,Ge:H				
20266/A8	1.586	6.5	69.4	7.2
20283/B5	1.540	6.9	62.6	6.7
20290/B7	1.568	6.3	66.0	6.5
20268/A8	1.531	6.0	66.1	6.1
20228/B1	1.531	6.2	62.8	5.9
20280/C5	1.528	5.7	64.1	5.6

Clearly, good V_{OC} and FF values have been obtained with efficiencies limited by the low J_{SC} values. To address this problem, the key activities in tandem cell research during the latter part of this program centered on:

1. Tandem cell design and analysis using the optical and I-V modeling previously developed.

2. Fabrication of tandem cells using the low band gap a-(Si,Ge):H i-layer described in Section 4.

The device design activity yielded important insight into experimental planning and will be discussed first.

6.1 TANDEM CELL DESIGN AND ANALYSIS, V_{oc} AND FF

Analysis of the relation between single-cell and tandem performance is essential in tandem optimization and requires detailed modeling.[17,18] Simulations of the I-V characteristics of the tandem structure can be obtained from an equivalent circuit approach if the parameters of the single-junction cells are known.[17] This model represents the solar cell with an equivalent circuit with lumped-parameter elements.

The value of J_{sc} to be used to characterize the magnitude of the constant-current source can be estimated from measured single-junction cell quantum efficiency data. An attempt to predict the tandem cell efficiency achievable with the single-junction technology available at the beginning of the last program quarter (Appendix C), illustrates this approach. A tandem cell efficiency near 9%, limited by the long wavelength response of the bottom cell, was predicted by this calculation.

Current-matched tandem structures can be designed with help from the optical model discussed in Section 5. In what follows, a tandem design will be sketched and its performance predicted based on that of the single-junction technology developed in the last quarter of this program.

Calculations using the equivalent circuit model (Appendix C) show that, under reasonable approximations of perfect equality between the currents generated by the two cells and negligible tunnel junction resistive losses, the tandem parameters are given by:

$$V_{oc} = V_{oc}(1) + V_{oc}(2)$$

$$FF = [FF(1) + FF(2)]/2$$

$$J_{sc} = J_{sc}(1) = J_{sc}(2)$$

where 1 and 2 denote the top and bottom cells, respectively.

If it is assumed further that the design thicknesses of the two cells in the tandem are small so as to not introduce excessive i-layer recombination losses, then the relatively high values of V_{oc} and FF obtained for the thinnest samples can be used in predicting tandem performance. Since values of over 900 and 650 mV and 75% and 55% seem to be realistically attainable for thin top and bottom cells respectively, tandem V_{oc}'s of 1550-1600 mV and FF's of 65% could be achieved. Table 6-2 shows the I-V parameters required of a tandem cell designed to exceed 10% efficiency.

TABLE 6-2. PARAMETERS OF SINGLE AND MULTI-JUNCTION CELLS OF A 10% TANDEM CELL AS CALCULATED FROM I-V MODEL

Cell	V_{oc} (mV)	FF (%)	J_{sc} mA/cm^2	Eff (%)
a-Si:H	900	75	10	
a-(Si,Ge):H	650	55	10	
Tandem	1550	65	10	10.1

The design of the tandem structure needed to obtain J_{sc}'s of 10 mA/cm^2 or more will be discussed below.

6.2 OPTICAL MODELING OF TANDEM J_{sc}

A typical calculation in which the thicknesses of the top (a-Si:H) and bottom (a(Si,Ge):H) cells have been adjusted to produce equal light-generated currents is described in what follows. If J_{L1} and J_{L2} are the currents from the top and bottom cells, their thicknesses t_1 and t_2 are determined by:

$$J = J_{L1}(t_1,t_2) = J_{L2}(t_1,t_2)$$

We have obtained values of t_1 and t_2 using the optical model described in Section 4. The current J_{L1} increases with t_1 until it saturates as t_1 exceeds 1000 nm and is a weak function of t_2. On the other hand, J_{L2} oscillates as a function of t_1 and t_2 due to the interference effects built into this model by the assumption of specularity.

If we recall that texture enhancement is on the order of 15% (Section 5), then a specular structure for which $J_{L1} = J_{L2} = 8\text{-}9$ mA/cm^2 can, when built on textured SnO_2, yield currents in excess of 10 mA/cm^2. Such a structure is shown in Table 6-3, where J_L* has been calculated using the 15% enhancement factor.

From these data, we conclude that a device with a 140 nm, a-Si:H top cell and a 200 nm a-(Si,Ge):H bottom cell can exceed 10 mA/cm^{2}when light trapping is successfully incorporated into the design. The slightly higher J_L from the bottom cell is of little concern, since a-(Si,Ge):H cells suffer from higher recombination than a-Si:H cells. Attempts to build such a tandem structure based on the alloy devices developed will be summarized below.

TABLE 6-3. LIGHT-GENERATED CURRENTS AND PHOTON LOSSES OF TANDEM STRUCTURE

Layer	Thickness (nm)	Photon Loss (mA/cm^2)	J_L (mA/cm^2)	J_L* (mA/cm^2)
Glass	-	0.21	-	
SnO_2	200	1.56	-	
Top Cell				
p_1^+	12	0.78	-	
i_1	140	-	8.71	10.01
n_1^+	12	0.38	-	
Bottom Cell				
p_2^+	12	0.06	-	
i_2	200	-	9.51	10.9
n_2^+	12	0.03	-	
Silver	500	0.18	-	

6.3 TANDEM CELL FABRICATION

Tandem cells were fabricated using the deposition techniques developed for single-junction a-Si:H and a-(Si,Ge):H cells. The structure consisted of:

1. A standard a-(Si,C):H:B p^+-layer.
2. A standard, sharply graded a-(Si,C):H transition layer.
3. A 140-180 nm a-Si:H i-layer grown at T = 350°C.
4. A standard a-Si:H:P n^+-layer.
5. A standard a-(Si,C):H:B p^+-layer.
6. A standard, sharply graded a-(Si,C):H transition layer.
7. A 50 nm, graded a-(Si,Ge):H transition layer.
8. A 200 nm, standard, constant composition a-(Si,Ge):H i-layer.
9. A 10 nm, standard, graded a-(Si,Ge):H transition layer.
10. A standard a-Si:H:P n^+-layer.

The plasma cleaning routine followed was as described in Table 5-1. Perhaps the largest departure from the standard a-Si:H cell fabrication process is the deposition of the top cell i-layer at T = 350°C. This was done in order to deposit the tandem structure with minimum changes in process temperature, since the optimum a-(Si,Ge):H was obtained at this temperature. Table 6-4 shows I-V data for a series of a-Si:H p-i-n cells with 350°C i-layers of thicknesses 140-160 nm. Average values over all 0.1 cm^2 area devices are reported.

TABLE 6-4. AVERAGE I-V CHARACTERISTICS OF 0.1 cm^2 AREA DEVICES FOR a-Si:H CELLS WITH 350°C I-LAYERS.

Sample	V_{oc} (mV)	J_{sc} (mA/cm^2)	FF (%)	Eff (%)
20517	894	9.1	70.0	5.7
20518	865	9.3	73.2	5.9
20527	879	8.3	72.8	5.3
20531	887	8.1	70.3	5.1

Clearly, V_{oc} and FF values are as high for cells processed at 350°C as at 275°C.

The deposition techniques summarized above were applied to the fabrication of a tandem device of a design similar to that developed in 6.1. Results will be discussed below.

6.4 TANDEM CELL ANALYSIS

The I-V characteristics of the highest efficiency devices in three tandem samples can be seen in Table 6-5. No spectral corrections have been made (see Appendix A) but from sunlight measurements an error of less than 5% is expected in the measured efficiency.

TABLE 6-5. I-V CHARACTERISTICS OF TANDEM CELLS MEASURED UNDER A SOLAR SIMULATOR.

Sample	Area (cm^2)	V_{oc} (mV)	J_{sc} mA/cm^2	FF (%)	EFF (%)	Comments
20532-C2	0.1	1422	7.7	55.7	6.1	AM1.5
		1422	7.7	54.6	6.0	Blue Light Bias
		1422	7.7	62.0	6.8	Red Light Bias
20532-C6	0.5	1414	7.5	56.4	6.0	
20533-B0	0.1	1431	7.5	60.5	6.5	
20533-C3	0.5	1377	7.5	57.3	6.0	
20535-B0	0.1	1402	7.3	56.9	5.8	

Analysis of the data for cell 20532-C2 using blue and red-filtered light shows that its FF is closer to that of the a-(Si,Ge):H cell. The SiGe cell is thus the current-limiting cell in this structure. This sample exhibited an inflexion point in its I-V characteristic near V_{oc} ("double diode"), attributed to an imperfect tunnel junction (Figure 6-1).

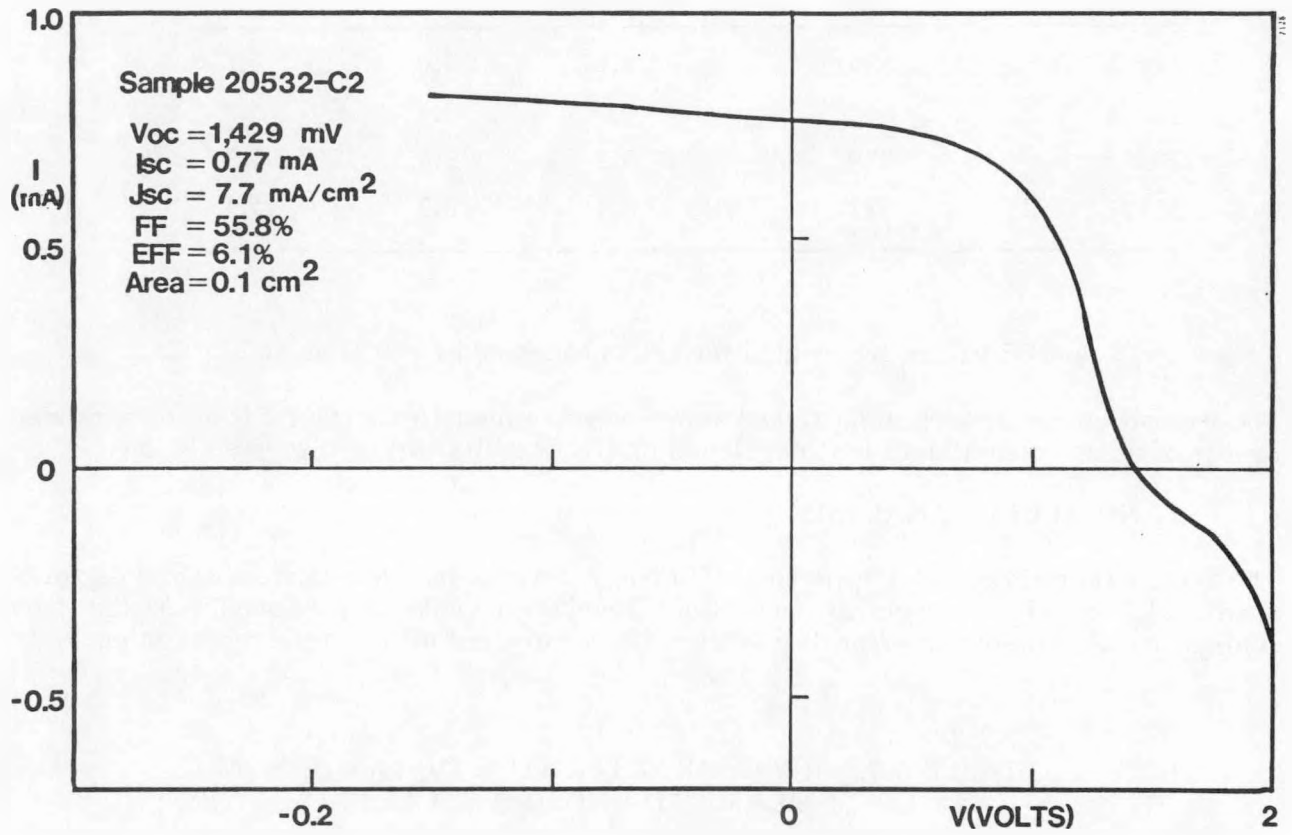

FIGURE 6-1. I-V CHARACTERISTICS OF CELL 20532-C2.

In an unsuccessful attempt to avoid the inflection of IV, sample 20533 was prepared with a slightly thicker, 275°C p^+-layer at the tunnel junction. With the p^+-layer deposited at 350°C (sample 20535), no inflexion point occurs (Figure 6-2). This is interpreted as an indication of the formation of a true tunnel junction due to improved compensation at the higher temperature.

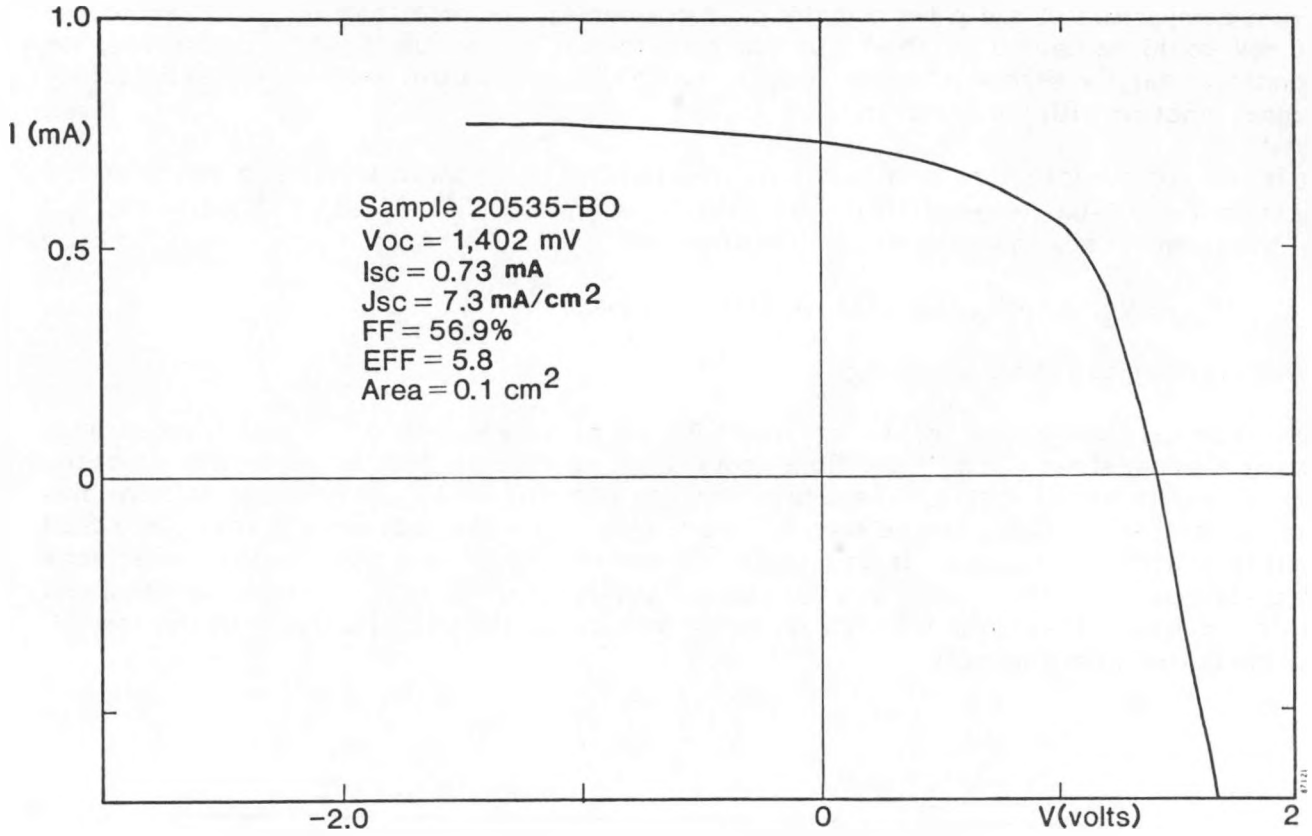

FIGURE 6-2. I-V CHARACTERISTICS OF CELL 20535-B0.

The I-V characteristics of three single-junction devices prepared under similar conditions as the top and bottom cells in the tandem samples can be seen in Table 6-6.

TABLE 6-6. I-V CHARACTERISTICS OF SINGLE-JUNCTION CELLS. Area 0.1 cm^2.

Sample	Area (cm^2)	V_{oc} (mV)	J_{sc} (mA/cm^2)	FF (%)	EFF (%)	Comments
20531-C0	a-Si:H	894	8.3	70.7	5.3	p-i-n structure
20534-B5	a-Si:H	833	8.3	71.7	5.0	p-i-n-p structure second p^+-layer at 350°C.
20536-B7	a-(Si,Ge):H	592	14.7	55.3	4.8	

From comparison of the p-i-n and the p-i-n-p samples, we note that a V_{OC} difference of 60 mV could be caused by the n^+/p^+ junction. Since no "double diode" is observed, we conclude that the second p^+-layer, prepared at 350°C, does form a relatively satisfactory tunnel junction with the n^+-layer.

It is not our purpose here to account for the tandem cell characteristics in terms of the data in Table 6-6. However, from the data for samples 20534-B5 and 20536-B7, the V_{OC} of the tandem cells can be understood as the sum:

$$V_{OC} = V_{OC}(1) + V_{OC}(2) = (833 + 592)\ mV = 1{,}425\ mV$$

which is close to the measured V_{OC}.

Quantum efficiency data for device 20535-B0, obtained under blue and red filtered light under tandem short circuit conditions (equivalent to reverse bias in the active junction, see Appendix B) and with a voltage bias equal to one-half its V_{OC} (equivalent to zero bias for the active junction), can be seen in Figure 6-3. From the data we see that the a-Si:H cell is limiting in this case. If an integrated reverse bias to zero bias quantum efficiency ratio is calculated for the top and bottom cells, values on the order of 1.10 are obtained. This is consistent with the behavior observed in a-(Si,Ge):H cells, that is with the low FF of the bottom, limiting cell.

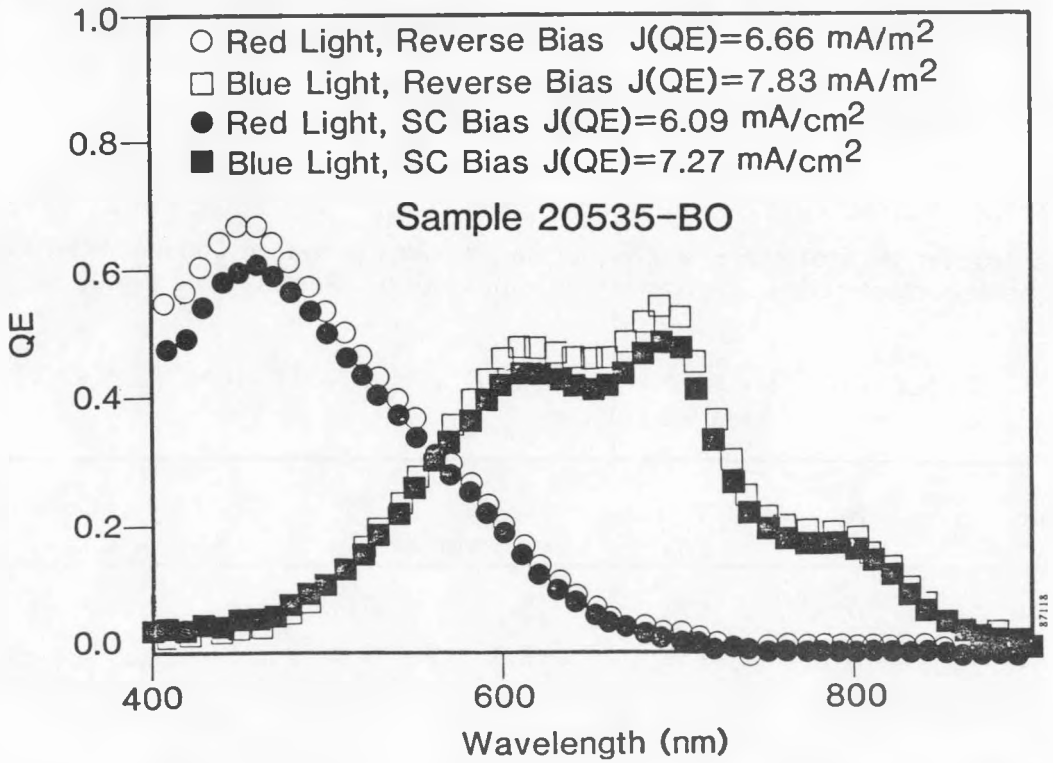

FIGURE 6-3. QUANTUM EFFICIENCY OF TANDEM CELLS AT SHORT-CIRCUIT AND REVERSE BIAS CONDITIONS.

The failure of this type of device to achieve its design efficiency can be understood in terms of the above analysis. While use of textured SnO_2 can raise the efficiency to about 7%, and improved tunnel junctions and cell structure may yield higher V_{oc} and FF, 10% efficiencies cannot be achieved unless better alloy quality is obtained.

6.5 COMPARISON WITH PREVIOUS RESULTS

The tandem cells fabricated did not achieve efficiencies as high as have been previously obtained in this program. The I-V parameters of cell 20266-A3, made with graded a-(Si,Ge):H alloys with a relatively low overall (Ge)/(Si) ratio, as compared to those of cell 20533-B0 containing the 1.4-1.5 eV lower bandgap alloy developed during the latter part of this program, are shown in Table 6-7.

TABLE 6-7. I-V CHARACTERISTICS OF TANDEM CELLS. Area 0.1 cm^2.

Sample	Area (cm^2)	V_{oc} (mV)	J_{sc} mA/cm^2	FF (%)	Eff (%)
20266-A3	0.1	1,586	6.5	69.2	7.2
20533-B0	0.1	1,431	7.5	60.5	6.5

The results show an increase in J_{sc} and a corresponding decrease in V_{oc} in cell 20533-B0, as expected when a lower bandgap alloy is used in the bottom cell i-layer. A comparison of the quantum efficiencies (Figure 6-4), suggests that the higher J_{sc} of cell 20533-B0 indeed arises from the long wavelength response of the bottom cell. Note also that cell 20266-A3 was grown on textured SnO_2, while 20533-B0 was grown on specular material. With use of textured, high transparency SnO_2 substrates, as well as further optimization of the tandem structure, J_{sc} values in excess of 10 mA/cm^2 can be obtained. However, the higher current-generating capacity of the low bandgap alloy translates once more into a lower carrier collection, resulting in a low FF of cell 20533-B0 and yielding a lower efficiency.

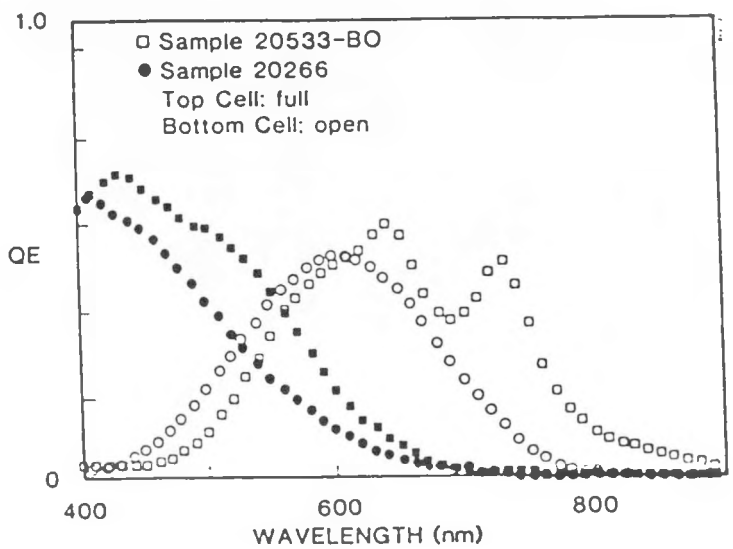

FIGURE 6-4. COMPARISON OF THE QUANTUM EFFICIENCIES OF TANDEM CELLS.

The activities of most importance to improve tandem efficiencies can be summarized as follows:

1. Develop improved n^+/p^+ tunnel junctions.
2. Develop improved a-(Si,Ge):H alloys.
3. Deposit tandem devices on textured, high transparency SnO_2 substrates.
4. Improve device design and deposition to avoid J_{sc} limitation by the lower FF cell.

REFERENCES

1. V.L. Dalal et al., Annual Report, "Research on High-Efficiency, Stacked, Multi-Junction Amorphous Silicon Alloy Thin-Film Solar Cells," Phase I (1984), SERI/STR-211-2730.

2. V.L. Dalal et al., Conf. Rec. 18th IEEE Photovoltaic Specialists Conference-1985, IEEE, New York (1985), p. 1500.

3. V.L. Dalal et al., Semi-Annual Report, "Research on High-Efficiency, Stacked, Multi- Junction Amorphous Silicon Alloy Thin-Film Solar Cells," Phase III (1986), SERI/STR-211-3104.

4. J.A. Bragagnolo et al., Proceeding of the 1987 Amorphous Silicon Subcontractors' Review Meeting, Palo Alto, California, SERI/CP-211-3086 (Rev. 3/87), Jan. 1987, p. 169.

5. V.L. Dalal et al, Annual Report, "Research on High-Efficiency, Stacked, Multi-Junction Amorphous Silicon Alloy Thin-Film Solar Cells," Phase II (1986), SERI/STR-211-2946.

6. V.L. Dalal et al., Con. Rec. 18th IEEE Photovoltaic Specialists Conference-1985, IEEE, New York (1985), p. 837.

7. V.L. Dalal et al., Semi-Annual Report, "Research on High-Efficiency, Stacked, Multi- Junction Amorphous Silicon Alloy Thin-Film Solar Cells," Phase I (1984), SERI/STR-211-2636.

8. R. Gordon et al., Final Report to SERI, Subcontract No. XS-0-9318-2 (October 1984).

9. V.L. Dalal et al., Semi-Annual Report, "Research on High-Efficiency, Stacked, Multi- Junction Amorphous Silicon Alloy Thin-Film Solar Cells," Phase II (1985), SERI/STR-211-2845.

10. C.A. Megerie et al., Conf. Rec. 17th IEEE PV Specialists Conference 1984, IEEE, New York (1984), p. 212.

11. F.B. Ellis and A.E. Delahoy, Solar Energy Materials 13 (1986), p. 109.

12. G.D. Cody in Semiconductors and Semimetals, Academic Press, Orlando, Florida (1984), p. 11.

13. K. Mitchell et al., Conf. Rec. 18th IEEE Photovoltaic Specialists Conference-1985, IEEE, New York (1985), p. 894.

14. H.W. Deckman et al., Appl. Phys. Lett. 42, p. 968 (1983).

15. G.D. Cody et al., J. de Physique 42, C-4, 301 (1981).

16. T. Tiedje et al., J. Non-Crystalline Solids, 77-78, p. 1031 (1985).

17. G.F. Virshup and J.G. Werthen, Conf. Rec. 18th IEEE Photovoltaic Specialists Conference-1985, IEEE, New York, NY (1985) p. 618.

18. J. Burdick and T. Glatfelter, Proc. Photovoltaics and Insolation Measurements Workshop, (June 30-July 3, 1985, Vail, Colorado), SERI (1985), p. 151.

APPENDIX A

SAFETY ISSUES IN a-Si DEPOSITION
by Vikram Dalal

The following safety issues are important in building and operating a-Si reactors. The discussion is by no means complete, but is only illustrative.

1. Integrity of Gas Manifolds, Cabinets, Lines and Exhaust

Since the gases used are pyrophoric, flammable or highly toxic, proper precautions should be taken in handling and containment of these gases.

A. Gases should be stored in OSHA approved cabinets, with approved dispersing of cylinders i.e. Do not mix oxidizing and reducing gases in one cabinet, keep toxic gases in a separate cabinet etc. Proper cabinet-sharing arrangements are available by consulting any vendor of such gases (e.g. Matheson, Scientific, Gas Products etc.).

B. Under no circumstances should the hazardous gas bottles be left outside of a vented cabinet.

C. All gas cylinder connections must be checked for leaks.

D. All joints (e.g. weld fittings etc.) should be in a vented area i.e. the gas manifold containing flow controllers etc. should be in a vented cabinet. All welded joints should be He leak-checked.

E. An indicator (either a pressure sensor or an air flow velometer) with an audible alarm should be installed to check that the exhaust blowers are working, and that the gas cabinets etc. are under negative pressure.

F. It is a good idea to have a separate room exhaust which can exhaust the room in 1 minute. In an emergency, activating this super-exhaust will allow fresh air to rush into the room and exhaust the dangerous gases outside with a high dilution factor.

G. It is a good idea to install flow-limit valves (available from Veriflo) which limit the flow to small values, as close to the gas cylinder as possible. These valves are useful in the event of a line break downstream.

H. All hazardous gases should have cross-flow purge assemblies, so that the entire lines and regulators can be evacuated and flushed with an inert gas such as argon several times (5 cycles will do) before changing cylinders. Also, the procedure should be repeated after changing cylinders, so any residual air is highly diluted. One part of purge assembly should be connected to vacuum, and the other to argon.

I. One-way valves should be installed to prevent suck back of air into regulators. If one installs these valves, one should be careful during changing bottles, since gases will be trapped upstream of the valve, and must be flushed out using cross-flow vacuum/Argon cycles described in H. above. The most likely accident is air reacting with trapped SiH_4 in a regulator (or SiH_4 reacting with trapped air when a

new bottle of SiH_4 is installed.) Such an accident could be catastrophic, since the regulator could explode. Many people in the semiconductor industry have been killed or maimed by this particular type of accident.

J. It is a good idea to install pneumatic solenoid valves which shut-off flow from the cylinders. These valves should be close to the cylinders. If you have these valves, be sure that you have opened them when doing the evacuation/flush cycle described in H above, otherwise there will be some trapped gas in a line. These solenoid valves should be controlled from individual switches on the reactor control panel, and should be normally-closed type.

K. If you are using computer-control of gas flows, be sure to have positive shut-off solenoid valves in series with and downstream of each flow controller. The shut-off valve on the flow controller itself is often not positive shut-off, and in our experience, sometimes does not shut tightly. It pays to assume that the line upstream of the solenoid valve is fully pressurized, even though the flow-controller is set at zero.

L. Rotameters are dangerous, and should not be used for hazardous gases. We have seen needle valves of rotameters serve as a conduit for escape of gases into the room. (This happened with BF_3). An escape of SiH_4 or PH_3 through the needle valve could be catastrophic. Also, the needle valves get damaged easily.

M. It is useful to have N_2 or Argon plumbed directly into the reactor, and into the manifolds, so that the lines and the reactor can be rapidly purged if needed.

2. Procedures For Changing Gas Bottles

Quite the most dangerous procedure is changing gas bottles. Consider what can go wrong.

- The wrench can slip and break a line.
- The cylinder valve may not close tight.
- You may have forgotten to evacuate trapped gas.
- The cap on the new bottle may be pressurized, because the valve on the new bottle was not tightly closed.
- The thread on the CGA fitting on the new cylinder may be damaged. (The author was once the unfortunate recipient of a Si_2H_6 cylinder where the valve would not seal after opening, and the output thread was damaged at the vendor's facility. Fortunately, a cross-purge assembly was present, and by some adroit manipulation of the vacuum and Argon lines, we were able to safely evacuate the cylinder.)

One must establish firm, well thought-out procedures for changing gas bottles. These must be followed. They must be written down. Certain trustworthy employees must be thoroughly trained in changing of gas bottles, and only they should be allowed to change hazardous gas bottles.

There must always be two people present, each well versed in changing bottles, during the change operation. One should do the procedure, the second should check it off.

It is also important that both people wear portable gas masks with dual air supply (house and bottle air). If the cylinder cap is pressurized, one can easily die while opening it if one is not wearing a mask.

It is very important that the employees entrusted with this operation be totally reliable. This is one operation where one can use a dedicated team (as at IBM or DEC), or, in a smaller facility, a scientist/technician team. This job is not too small for a scientist. It is too important to be entirely entrusted to low-level people. One only needs to do it once every 3 months. Might as well do it right.

One should have O_2 supply, and CPR trained personnel available in the facility when dealing with these gases. First aid techniques for handling these gases must be thoroughly studied, and the local hospital must be aware of what gases you are dealing with, and what the treatments are. Consulting with local fire departments and first aid rescue teams on a routine basis is a good practice, as also conducting evacuation drills. PH_3, B_2H_6, GeH_4, SiH_4, AsH_3, etc. are just too dangerous to not be thoroughly familiar with their effects.

3. Toxic Gas Detectors

It goes without saying that toxic gas detectors be available in the facility for detecting leaks of AsH_3, PH_3, etc. These should be located in the exhaust from the gas cabinets, gas manifolds, in the output of the scrubber, and over the reactor. Several companies make multi-point monitor systems.

4. Automatic Shut-off Valves

It is very important that provisions be made for shutting off flow of gases into the reactor in the event of a pressure increase due to power failure or vacuum-pump failure. Belts will break, motors will burn out, pumps will catch fire, power will fail. A simple relay circuit on the Baratron pressure indicator circuit, combined with the use of normally closed solenoid valves on the gas inlet, can be used to close the inlet valve in the event of a pressure rise or a power failure. This must be an automatic operation, with a bypass provided only for repair/rapid evacuation etc. If a bypass is used, the bypass mode must be sufficiently obnoxious (e.g. loud buzzer) so that one does not normally use it. This precaution is very important. One cannot rely on the operator watching dials and then reacting. The tragedy at Bhopal has made automatic cut-offs imperative.

It is also a good idea to have all gas solenoid valves and high voltage/RF power supplies on trip circuit breakers, i.e. if the power fails, all breakers trip, and have to be manually reset one at a time. It costs little to buy such breakers, but really helps out in safety. Of course, all breakers should be clearly identified as to the circuit they control.

5. Redundant Systems

It is useful to have redundant systems. A good example is two mechanical pumps, one the work horse, the second a smaller version for emergencies. The failure of one pump will still leave you with one operating pump, which should be connected in parallel with the first. The extra cost is minimal, less than $2,000. Both pumps should be on all the time, with the reserve one being fed Argon to keep air out and oil in.

Similar redundancies in valves and scrubbers (or gas burn-offs) would be useful.

6. Use of Inert Gas

To avoid explosions in mechanical pumps, it is useful to bleed Argon upstream of the trap continuously. Also, N_2 should be bled into the exhaust line of the mechanical pump at a fairly robust rate so that the hazardous gases (SiH_4 etc.) are diluted at least 1000:1 in the exhaust line (By the time they reach the outside, even without a burn off or a scrubber, they will be diluted to ppb levels). This simple precaution prevents explosions in mechanical pumps, or in scrubbers. Caution: if you are using "house" N_2, always have a N_2 cylinder for stand-by in a parallel mode.

7. Stand-by Power

It is the author's opinion that a simple, auto-trigger, stand-by, diesel generator or a UPS to power exhaust blowers and mechanical pumps is one of the most useful precautions one can take. Once the hazardous gases are out of the building, they are diluted to ppb levels, and we are safe. But one must exhaust the gases trapped in the reactor and pumps during a power failure, because a leak of air could trigger an explosion.

8. Precautions on Vacuum Pumps

Several models of vacuum pumps have auto-shut off valves to shut off the inlet of the pump in a power failure so that oil and air cannot go upstream into the line. Unfortunately, in some models, the shut-off is triggered by air diffusing through the oil, where it can react with SiH_4. This is a bad design, which some other manufacturers avoid by providing that a N_2 purge will initiate a shut-off. Such models are clearly to be preferred. If you have an unsafe model, be sure to bleed N_2 into the pump chamber to avoid a SiH_4-air explosion. Read your pump manual carefully, and ask the vendor.

Of course, only inert pump fluid (Fomblin etc) should be used.

9. Use of Decomposition Furnace, Scrubbers and Burn-offs.

A decomposition furnace, maintained at a high temperature (1000°C) will clearly help decompose SiH_4, PH_3, B_2H_6, GeH_4, etc., and allow only H_2 to go through. A scrubber, or a burn-off, following this furnace will reduce or burn any residual gas. Thus, a combination of a decomposition furnace and a scrubber/burn-off will clearly help in reducing hazardous gas emissions. Of course, the furnace tube will have to be cleaned periodically. Also, the tube only has a finite life at high temperatures.

10. Use of Premixed Gases

There is much to be said for using PH_3, AsH_3, B_2H_6 premixed with SiH_4. SiH_4 burns easily, and the combustion will decompose PH_3 etc. easily, reducing them to relatively harmless particulates and gases. Particulates can be poisonous, but nowhere to the same extent as AsH_3 or PH_3. So, if process conditions permit, the use of premixed gases would be an added safety condition.

Needless to say, use of pure AsH_3, PH_3, B_2H_6 or GeH_4, or even large concentrations of these, is very, very dangerous. A leak could be instantly fatal. It is good to avoid using pure dopant gases if possible.

11. A Master "Panic Button"

The use of a master "Panic Button", centrally located, easily accessible and visible, to switch off all power to gas lines and therefore all valves, is imperative. This panic button should not turn off vacuum pumps or exhaust blowers.

Conclusions

To conclude, we have tried to illustrate some of the safety issues involved in a-Si:H deposition. While one cannot address all eventualities (e.g., a bomb explosion next to a PH_3 tank), we have tried to address the likely failure scenarios and some safe practices. The discussion is not complete. It is meant to stimulate discussion and thought. A very useful exercise would be a list of disaster scenarios for each group's peculiar experimental arrangements, and the relevant safety precautions for each case. For a-Si technology, as for all other high-tech industries, the lessons of "Three Mile Island" and Bhopal are quite clear: safety must start at the top, disaster scenarios must be thought out, automatic controls with redundancy must be installed, and only the best trained operators be allowed to perform hazardous tasks.

APPENDIX B

CALIBRATION PROCEDURES

by
J.F. Booker

Careful calibration of light sources and reference cells is crucial to proper measurement of solar cell performance. Practical methods for determining cell performance rely on a total irradiance measurement using either a black body detector or a photovoltaic reference cell. Interpretation of measurements from these devices is necessary to determine actual cell efficiencies.

For single-junction cells the primary consideration is to provide a method for determining the short-circuit current of the cell. This is most simply done by choosing a solar simulator having the spectral content of the standard spectrum,[1] or by choosing a reference cell with spectral response closely matching that of the cell being tested. If either option is possible, then the use of spectral mismatch factors[2] provides a method of determining the short-circuit current. Measurement of tandem cells is more complex, and will be briefly discussed below.

B.1 PROCEDURE

Our method for establishing the calibration of our indoor simulator (Oriel Xenon 1000W solar simulator) is based on the outdoor measurement of the particular type of amorphous cell we will be measuring indoors. Measurement of outdoor irradiance has relied on the use of crystalline silicon reference cells calibrated at Spire on a Spectrolab X-25 solar simulator, based on a primary cell from JPL.[3] Recent measurements using a filtered x-Si reference cell No. S14 provided by SERI[4] show agreement to within 2%.

The procedure is based upon the following steps:

1. Measurement of solar irradiance using a x-Si reference cell. Precautions are taken to minimize measurement errors and to ensure that the actual spectrum is close to the standard spectrum: We require T=18-24°C, no cloud cover, relative humidity <50%, low turbidity (no visible haze), and solar irradiance of 95-105 mW/cm^2.

2. The short-circuit current of the amorphous cell is measured, giving a current density under standard conditions.

3. The indoor simulator is set to an intensity giving the current density found in (2).

4. The response of a secondary reference cell on the indoor simulator is measured, giving a calibration for the simulator for a particular type of amorphous cell.

B.2 USE WITH SINGLE-JUNCTION CELLS

As a practical matter we find it most useful to use a x-Si cell with a Schott KG-3 color filter as our daily reference. This gives a reference cell which approximates the response of an amorphous cell with E_g 1.7 eV. We have found that use of an unfiltered reference with our Oriel Xenon simulator is unreliable: the long wavelength (>750 nm) output apparently changes significantly over time.

We do not presently have the capability for frequent spectral irradiance measurements on our simulator. This greatly limits our ability to use, and trust, mismatch calculations as a method of improving the accuracy of our short-circuit current measurements. Direct integration of quantum efficiency data with the standard spectrum has proven most useful as an independent method of determining current densities.

B.3 COMMENTS ON TANDEM JUNCTION MEASUREMENTS

The primary concern in single junction measurements is the determination of short-circuit current, with voltage and fill factor remaining relatively insensitive to the spectrum. For tandem cells, unlike single-junction cells, no reference cell can correct for an imperfect simulator. In series connected tandem cells fill factor becomes a strong function of the spectrum[5-6] because of the requirement of current matching. It thus becomes imperative to report corrections to both current and fill factor due to imperfect simulators.

While a detailed method for performing these corrections has not yet been proposed, the following conditions must be satisfied to provide for a method comparable to the use of spectral mismatch factors with single cells:

1. Actual current generated by each cell under standard conditions must be determined. This can be accomplished with a tandem cell quantum efficiency measurement.[7]

2. The actual operating conditions of the individual cells in the tandem under standard conditions must be reproduced. In general, the cells will not operate at the same voltage because of different internal short-circuit currents. As a result, the fill factor will most strongly represent the behavior of a single cell in the tandem structure. This is discussed in more detail in Appendix C. Simulation of standard conditions can most easily be accomplished using a small red or blue signal in addition to the simulator irradiance in order to generate the proper current in each cell of the tandem, as determined in (1).

The need for careful consideration of tandem cell measurements cannot be overlooked. On the basis of simulations performed at Spire it is evident that the fill factor error can in fact be greater than the error in current measurement with a tandem cell. For this reason continued work in this area will be necessary.

REFERENCES

1. R. Hulstrom, R. Bird, and C. Riordan, Solar Cells 15 (1985) 365.

2. C. Seaman, Solar Energy, 29 (1982) 291.

3. Private communication, M. Sanfacon.

4. Reference cell and calibration provided by W. Luft.

5. J. Burdick and T. Galtfelter, Proc. Photovoltaics and Insolation Measurements Workshop, Vail, CO (1985) 151.

6. G. Virshup and J. Werthen, to be published in Proc. 18th IEEE Photovoltaic Specialists Conf., Las Vegas, NV (1985).

7. "Research on High Efficiency Stacked Multi-Junction aSi Alloy Thin film Solar Cells, "Annual Report, Spire Corporation (1985).

APPENDIX C

TANDEM CELL ANALYSIS

by
J. F. Booker

1.0 INTRODUCTION

Methods of predicting and analyzing the behavior of series-connected tandem cells are essential to the development of high efficiency devices. The inability to directly probe the behavior of the individual cells is a serious problem in understanding the characteristics of the fabricated tandem cells. The requirement of current matching of the individual cells, while constraining the device design and spectral tolerance, provides a basis for extracting significant information on the single-junction cells which make up the tandem device. The ability to understand the effect of single cell characteristics on tandem cell performance is useful both for device design and diagnostic measurements of fabricated tandem cells.

As a first step to understanding tandem cell behavior we present the results of a computer simulation giving tandem cell I-V characteristics for realistic top and bottom cells in a two-cell stack.[1,2] We then discuss analytically the effect of single cell characteristics on the observed tandem cell fill factor. This provides insight into important factors for tandem cell device design and explains results of the computer simulation, in addition to pointing the direction for diagnostic measurements of completed tandem cells. Finally, we provide a mathematical justification for a technique to measure the quantum efficiency of tandem cells. This is useful in allowing a clear interpretation of quantum efficiency results under several different conditions.

2.0 BASIC MODEL AND BEHAVIOR

The requirement of current matching of individual cells in the series-connected tandem device, and an assumption of the electrical characteristics of the single cell interconnections, along with the single-junction cell device characteristics, serve to define the particular properties of a tandem cell. Modeling efforts using this approach have been very instructive in understanding the basic behavior of tandem cells. The computer simulation uses a double exponential diode model with shunt and series resistances for the single-junction cells of the tandem structure. A perfect tunnel junction is assumed, though resistive losses can be incorporated within the series resistance of either single cell. While there are serious shortcomings in the use of this single cell model to describe the behavior of amorphous silicon alloy cells, we believe that it is useful in achieving a reasonable approximation to the empirical behavior of these single-junction cells.

The purpose of this modeling effort was twofold. First, we wanted to understand in detail the expected performance of tandem cells fabricated using our single-junction cell technology. Second, in order to better understand the behavior of fabricated tandem cells we needed a way of assessing the impact of the constituent cells on the tandem cell behavior. In all this work we used the actual behavior of real single-junction cells as a starting point. The single-junction model was a convenient method for generating single cell I-V curves for a range of light levels; a very large data base of I-V curves would have served equally, if not better, for this purpose.

2.1 Equal Light Generated Currents

In general, we expect that the highest efficiency series-connected tandem cell must split the spectrum between cells such that the light generated current in the single-junction cells is equal. We estimated the total available light generated current from the quantum efficiency of the two individual cells we wished to use in the tandem structure. Splitting this equally between the single-junction cells determined the light generated current J_L for each in the tandem structure. Because the cells had relatively good collection characteristics, the difference between the short-circuit current J_{SC} and J_L was assumed to be negligible. Fill factors for the individual junction cells were determined by actual measurements under the operating condition in the tandem cell (e.g., 50 mW/cm^2 red light for the bottom cell). Parameters for the single-junction model were carefully chosen to accurately reflect the actual behavior of fill factor and voltage as a function of light intensity.

A calculation using an a-Si top cell and an a-(Si,Ge) bottom cell of the type available at the beginningof the last half-year of the program is shown in Figure C-1. The a-(Si,Ge) cell was made on lightly textured SnO_2,and a total light-generated current of 16 mA/cm^2 was calculated.

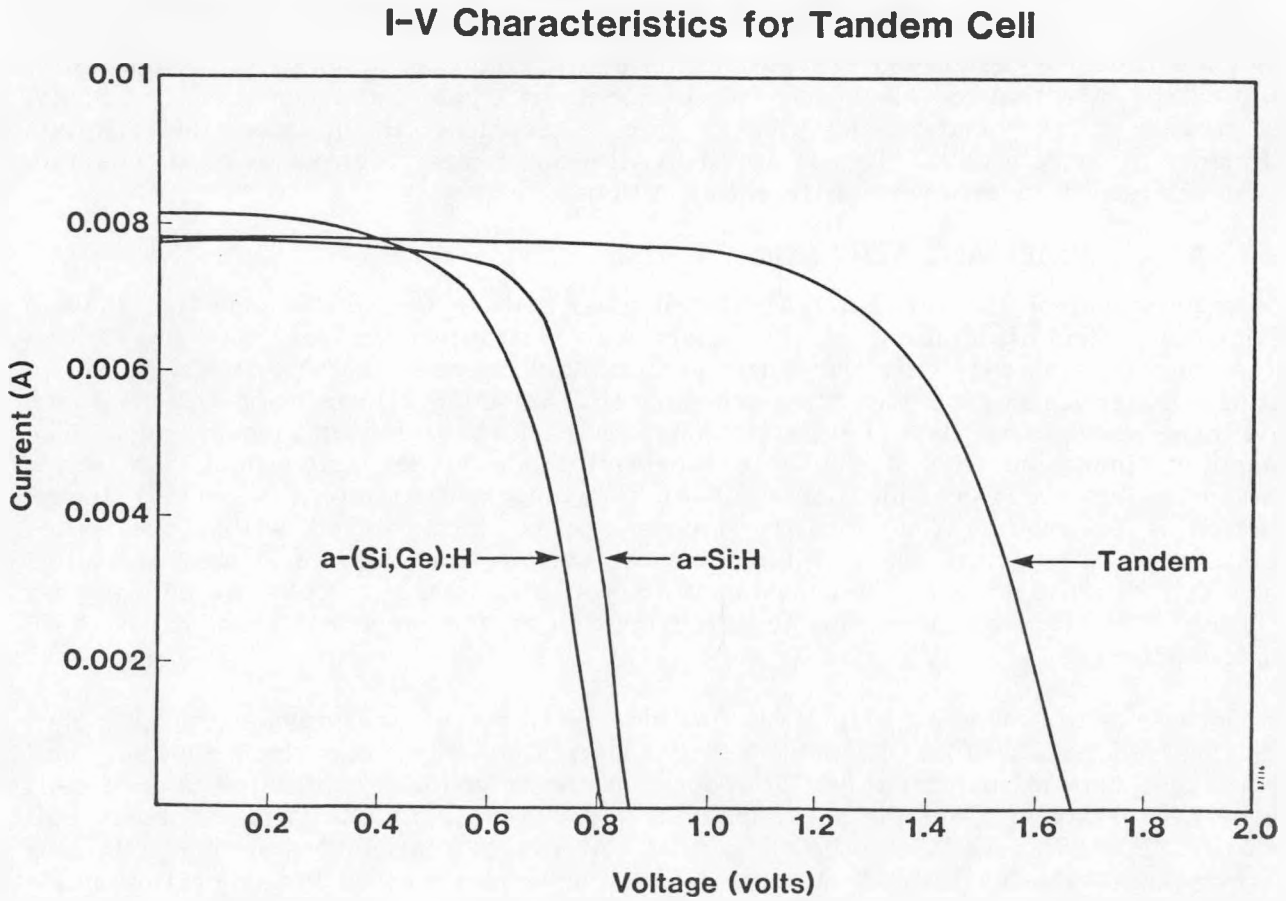

FIGURE C-1. I-V CHARACTERISTICS FOR TANDEM CELL

The single and tandem cell characteristics are summarized in Table C-1. As required by our assumptions, the tandem cell current is half the total light generated current and the open-circuit voltage is the sum of the single cell voltages. The fill factor is very close to an average of the single-junction fill factors. This is an important result, because it gives us a very simple method for predicting the maximum tandem cell efficiency given the properties of the constituent cells. While marginally higher efficiencies may be obtained by operating with unequal light-generated currents, as discussed below, the effect is not, in general, large enough to greatly effect the maximum efficiency.

TABLE C-1. I-V CHARACTERISTICS OF SINGLE AND TANDEM CELLS

Cell	V_{OC} (V)	J_{SC} mA/cm^2	FF (%)	(%)
Top	0.85	13	0.72	8.0
Bottom	0.80	16	0.61	7.8
Tandem	1.65	8	0.665	8.8

2.2 Unequal Light-Generated Currents

Most real tandem cells will be fabricated such that the light generated current in the constituent cells is not exactly equal. Moreover, any deviation of spectrum from the design spectrum will likely have the same effect. Thus it is essential to understand the behavior of tandem cells under these conditions.

Using the same constituent cells described above we let the light generated current in the individual cells vary, while maintaining a total light-generated current of 16 mA/cm^2. While the total will actually decline slightly as one cell becomes dominant, the effect for cells with somewhat similar band gaps will be small. Figure C-2 shows the tandem efficiency as a function of the top cell thickness. Alternately, we could express the efficiency as a function of J_L of the top cell, or the spectral balance of the incident light.

The tandem cell efficiency as a function of the top cell thickness is easily explained by examining the fill factor and short circuit current J_{SC} dependence shown in Figure C-3. Because current matching is required, J_{SC} cannot exceed the smallest J_L of the two cells. The fill factor of the tandem cell varies between two limits, reflecting the fill factors of the two constituent cells. The gain in fill factor can be greater than the loss in current, leading to the highest tandem cell efficiency occurring when the highest fill factor individual cell is slightly limiting. This is readily seen in Figures C-1, C-2, and C-3, where the greatest efficiency occurs for J_L = 7.7 mA/cm^2 in the top cell. This effect has been confirmed through measurements of actual tandem cell devices by varying the spectral content while maintaining a total intensity of 100 mW/cm^2.

3.0 ANALYSIS OF TANDEM CELL FILL FACTOR

It is often useful to interpret the current voltage characteristics of tandem cells in terms of the behavior of the underlying single-junction cells. The modeling efforts described

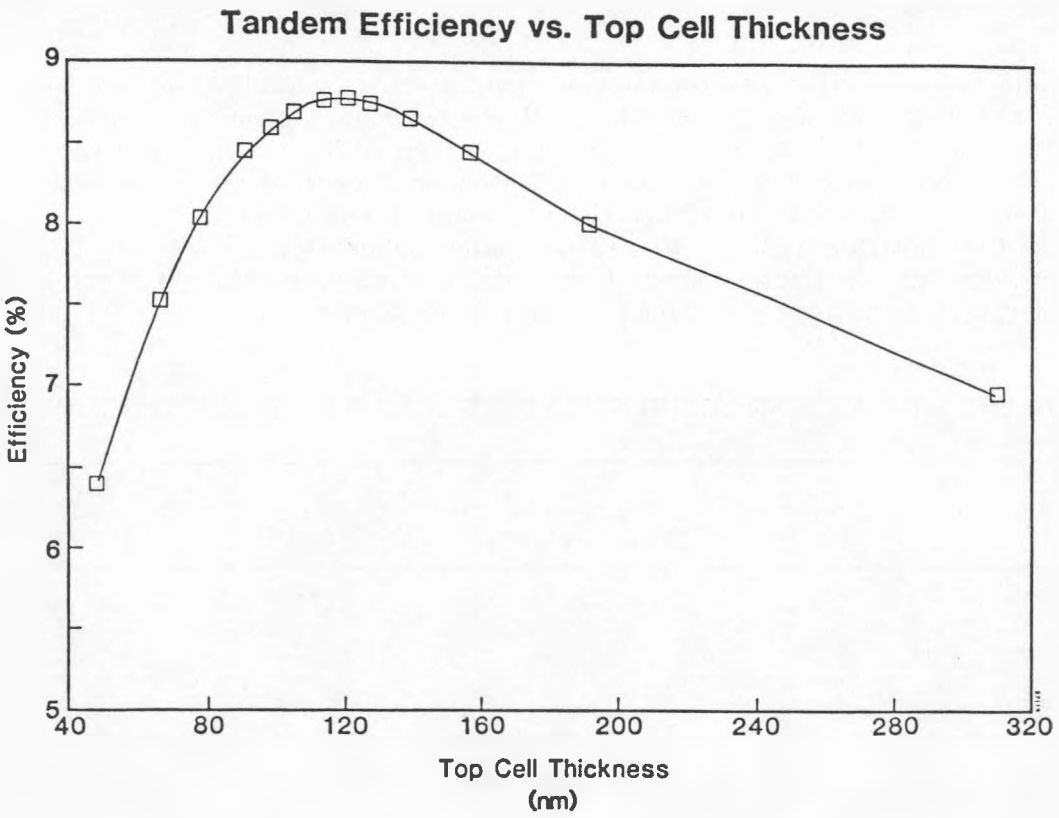

FIGURE C-2.

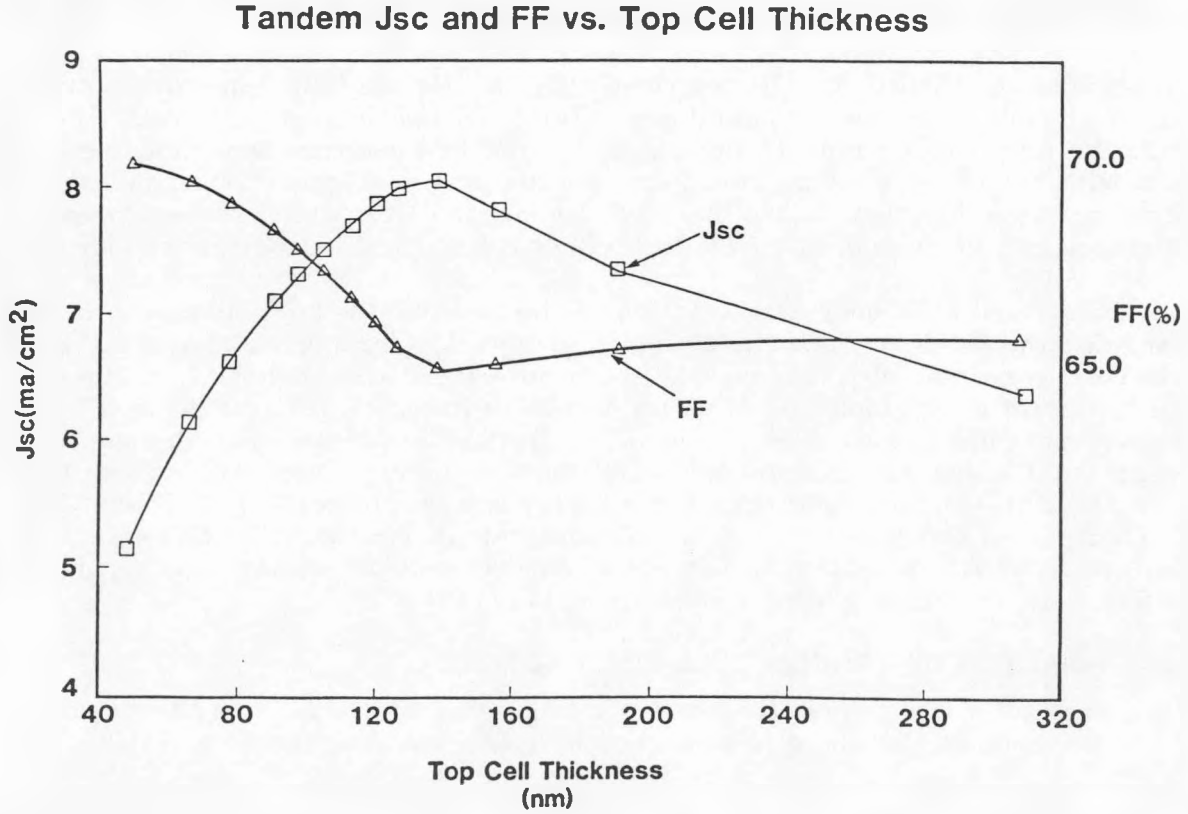

FIGURE C-3.

above have illustrated the major effects. Here we attempt to understand the tandem cell fill factor in terms of the single-junction cell characteristics.

If we operate a tandem cell in a mode where the light generated current of one cell is significantly greater than the second, then the I-V characteristic of the tandem cell is most easily understood in terms of the I-V characteristic of the limiting single-junction cell. In particular, the fill factor of the tandem is given by

$$FF_{tandem} = FF_{single} \quad (1)$$
$$+ \Delta FF_{diode} \quad (1a)$$
$$+ \Delta FF_{series} \quad (1b)$$
$$+ \Delta FF_{shunt} \quad (1c)$$

where (1a) - (1c) are small corrections to the limiting single cell fill factor FF. In general, (1a) is positive, (1c) is negative, and (1b) can be either positive or negative. The different terms are discussed below.

If we consider an "ideal" I-V curve, as shown in Figure C-4, the voltage loss ΔV at V_{mp} is more significant in the single-junction cell than the tandem cell by an amount $\Delta V/V_{mp,t}$ where $\Delta V = V^s_{oc} - V^s_{mp}$ for the single cell. If we neglect the current loss, which gives the same loss in fill factor in the single and tandem,

$$\Delta FF_{diode} = \Delta V/V_{mp,t} \quad (2)$$

where V_{mpt} is the maximum power voltage for the tandem.

Tandem losses are also caused by the sum of all series resistances present, $R_1 + R_2 + R_{np}$, where R_1 and R_2 are the series resistances of the single-junction cells and R_{np} is an assumed resistance in the tunnel junction. Neglecting all other losses, it is easily shown that

$$\Delta FF_{series} = J^s_{mp}/2V_{mps}\,[(R_1 - R_2) - R_{np}] \quad (3)$$

where J^s_{mp} refers to the single cell. If $R_1 = R_2$ then any losses due to series resistance effects will be the result of series resistance effects inherent to the tandem structure.

Because of higher operating voltages, shunt resistance losses seen under limiting conditions will be greater in the tandem cell than the single cell. We obtain:

$$\Delta FF_{shunt} = -V_{mp}/(R_{1,sh} J^s_{mp}) \quad (4)$$

where $R_{1,sh}$ is the shunt resistance of the limiting cell. Each of the above terms may easily be responsible for changes of 0.05 in fill factor. This clearly illustrates the importance of considering these different influences on fill factor when attempting to interpret tandem cell fill factors in terms of the underlying single cell fill factor.

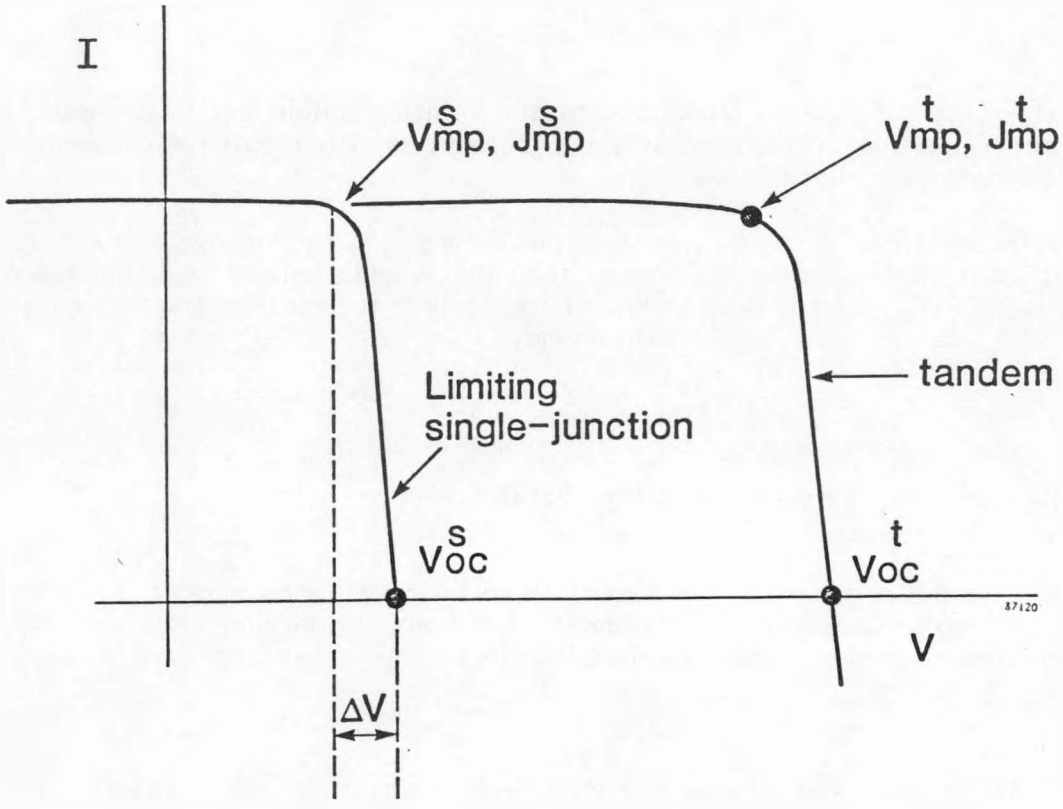

FIGURE C-4. I-V CHARACTERISTICS OF "IDEAL" TANDEM CELL

This analysis should be very helpful in measuring the single cell factors in completed tandem devices. We discuss below methods for measuring shunt and series resistance of the individual cells which can then be used to interpret fill factor measurements of the completed tandem devices.

4.0 TANDEM CELL DIAGNOSTICS

Development of high efficiency tandem structures requires a detailed understanding of loss mechanisms in actual devices. Many of the losses are best considered through the performance of the single-junction cells in the tandem structure. If the single-junction cell characteristics can be measured, then well-developed techniques for interpreting the behavior can be employed. Losses integral to the tandem structure itself can be identified and addressed separately.

In this section we examine in detail the tandem cell quantum efficiency technique,[3,4] including the implications for better understanding of tandem cell current-voltage characteristics. We will also show how current losses in the tandem structure can be measured using this method.

4.1 Quantum Efficiency Model

Quantum efficiency is a widely used experimental technique for measuring the response of a solar cell to monochromatic light. The signal light is generally a square wave produced by an optical chopper, and is of negligible intensity compared to a typical dc bias light of approximately 1 sun (100 mW/cm^2) intensity. The measurement an be performed at any desired voltage bias, yielding information on interface recombination and hole diffusion length. The response of a tandem junction cell to this same measurement, will, under appropriate voltage and light bias conditions, give the single cell quantum efficiencies.

Because current matching is required in series-connected tandem cells, the current response ΔI_t of the tandem cell to a small signal must equal the constant voltage response of the single cells. Let the tandem cell be held at a fixed voltage bias V_t, where the change in single cell voltage due to the signal light is ΔV_1 and ΔV_2. If we define ΔI_1 and ΔI_2 to be the constant voltage single cell response, then

$$\Delta I_t = \Delta I_1 - g_1 \Delta V_1 \qquad (1)$$

$$\Delta I_t = \Delta I_2 - g_2 \Delta V_2 \qquad (2)$$

and

$$\Delta V_1 + \Delta V_2 = 0 \qquad (3)$$

where g_1 and g_2 are the slopes of the single cell I-V curves at V_1 and V_2, respectively. We assume that the response to the signal light is small, so that $g_1(V_1) = g_1(V_1 + \Delta V_1)$ and $g_2(V_2) = g_2(V_2 + \Delta V_2)$. Also note that, because of imperfect collection, the current response ΔI of the single junction cells, and hence the tandem cell, is always a function of voltage.

Solving (1), (2), and (3) for the response of the tandem cell ΔI_t gives

$$\Delta I_t = (g_2 \Delta I_1 + g_1 \Delta I_2)/(g_1 + g_2) \qquad (4)$$

This result is the basis for interpreting quantum efficiency measurements of tandem cells.

4.2 Large Signal Quantum Efficiency

The basic concept behind measuring the quantum efficiency of a single cell in the tandem structure is to light bias the tandem cell in such a way that the light generated current in one cell is much greater than in the other. if the tandem cell is held at 0V then current matching requires that the light biased cell operate near its open circuit voltage V_{oc2}; thus the limiting cell operates at $-V_{0C2}$. Under these conditions $g_2 \gg g_1$ so that for wavelengths with $\Delta I_1 \approx \Delta I_2$ the term $g_2 \Delta I_1 \gg g_1 \Delta I_2$ in equation (4), giving

$$\Delta I_t = \Delta I_1 \qquad (5)$$

This relation holds at <u>all</u> tandem voltages for which $g_2 \Delta I_1 \gg g_1 \Delta I_2$. For example, to measure $\Delta I_1(V_1=0)$, we would need to use a tandem voltage near V_{oc2}. The single cell short-circuit current can then be calculated from the standard AM1.5 global spectrum [5] using results of such a measurement. This holds because eq. (5) holds for regions where ΔI_1 is not small. Such integrations show good agreement with measured short-circuit current measurements and are also of great use in determining the balance of light generated current in each cell.

Detailed results of this measurement can be interpreted in the usual way to provide detailed diagnostics of the individual single cell device performance. In addition, because eq. (5) shows that this is an absolute measurement of single cell quantum efficiency, variation of quantum efficiency from the expected single cell behavior must be indicative of electrical losses due to the tunnel junction, optical losses in the top cell, or unexpected performance in the bottom cell due to different growth conditions.

4.3 Small Signal Quantum Efficiency

As shown earlier, the single-junction IV characteristics can be understood from tandem cell I-V measurements under certain spectral conditions if the shunt and series resistances of each cell are known. The I-V measurement itself can directly measure the shunt resistance of each single-junction cell but cannot directly measure the individual series resistances. The quantum efficiency technique provides the means for measuring this series resistance.

Suppose we look at the behavior of the non-limiting cell using (4). Let cell 1 be the limiting cell. To measure the response of cell 2 we must have $g_1 \Delta I_2 \gg g_2 \Delta I_1$. This will happen if $\Delta I_2/\Delta I_1 \approx 10^3$, because $g_1/g_2 \approx 10^{-2}$. As an example, let the bottom cell be limiting (by using a blue bias light.) The response to a signal light at 400 nm must be from the top cell because of the very high absorption coefficient at this wavelength.

Now consider performing the measurement under two bias conditions. If $V_t \approx Vt_{oc}$ then both cells are operating in the series resistance region. Then (4) becomes

$$S_1 = g_1 \Delta I_2/(g_1 + g_2) \tag{6}$$

where S_1 is the response of the tandem cell. If the tandem voltage $V_t \approx V_{oc2}$ then $g_1 \ll g_2$, giving

$$S_2 = g_2^*/g_1 \ \Delta I_2 \tag{7}$$

where S_2 is the response of the tandem cell to this measurement and g_2^* is simply a shunt resistance determined from an IV measurement. If we assume that the tunnel junction contributes negligibly to the series resistance, the total tandem series resistance from an IV measurement is

$$g_t = g_1 + g_2 \tag{8}$$

Solving for g_1 and g_2 using (6), (7), and (8) gives

$$g_{1,2} = g_t/2 \pm \sqrt{\frac{g_t^2}{4} - c\, g_t} \tag{9}$$

where

$$c = S_1/S_2\ g_2^* \tag{10}$$

A large degree of care must be made in carrying out this measurement, as the series resistances g_1 and g_2 are strong functions of light intensity. In particular, it is important that (8) be measured under the same conditions as the quantum efficiency measurements. The values for g_1 and g_2 are then valid for the particular light bias of each cell during the measurement.

An alternative approach is to measure g_1 and g_2 directly from IV measurements under conditions where either g_1 or g_2 is negligible. This would require the light bias of one cell to be much greater than the other. Note that to measure g_1 or g_2 at one sun requires a light bias of much greater than one sun for the non-limiting cell of the tandem. If true linear resistances of the order of the measured resistance at V_{oc} are present this approach will fail. In most cases with single cells, however, we find a residual series resistance of only 1-2 ohm-cm^2 when extrapolating to light intensities much greater than one sun.

REFERENCES

1. G.F. Virshup and J.G. Werthen, Conf. Rec. 18th IEEE Photovoltaic Specialists Conference - 1985, IEEE, New York, NY (1985) p. 618.

2. J.A. Bragagnolo et al, Semi-annual Report, Phase III (1986).

3. V.L. Dalal et al., Conf. Rec. 18th IEEE Photovoltaic Specialists Conference - 1985, IEEE, New York (1985), p. 837.

4. J. Burdick and T. Glatfelter, Proc. Photovoltaics and Insolation Measurements Workshop, (June 30 - July 3, 1985, Vail, Colorado), SERI (1985), p. 151.